Characterization of Nanophase Materials. Edited by Zhong Lin Wang
Copyright © 2000 Wiley-VCH Verlag GmbH
ISBNs: 3-527-29837-1 (Hardcover); 3-527-60009-4 (Electronic)

Part I Technical Approaches

Characterization of Nanophase Materials. Edited by Zhong Lin Wang
Copyright © 2000 Wiley-VCH Verlag GmbH
ISBNs: 3-527-29837-1 (Hardcover); 3-527-60009-4 (Electronic)

1 Nanomaterials for Nanoscience and Nanotechnology

Zhong Lin Wang

Technology in the twenty first century requires the miniaturization of devices into nanometer sizes while their ultimate performance is dramatically enhanced. This raises many issues regarding to new materials for achieving specific functionality and selectivity. Nanophase and nanostructured materials, a new branch of materials research, are attracting a great deal of attention because of their potential applications in areas such as electronics [1], optics [2], catalysis [3], ceramics [4], magnetic data storage [5, 6], and nanocomposites. The unique properties and the improved performances of nanomaterials are determined by their sizes, surface structures and interparticle interactions. The role played by particle size is comparable, in some cases, to the particle chemical composition, adding another flexible parameter for designing and controlling their behavior. To fully understand the impacts of nanomaterials in nanoscience and nanotechnology and answer the question of why nanomaterials is so special, this chapter reviews some of the unique properties of nanomaterials, aiming at elucidating their distinct characteristics.

1.1 Why nanomaterials?

Nanomaterials are classified into nanostructured materials and nanophase/nanoparticle materials. The former refer to condensed bulk materials that are made of grains with grain sizes in the nanometer size range, while the latter are usually the dispersive nanoparticles. The nanometer size here covers a wide range which can be as large as 100–200 nm. To distinguish nanomaterials from bulk, it is vitally important to demonstrate the unique properties of nanomaterials and their prospective impacts in science and technology.

1.1.1 Transition from fundamental elements to solid states

Nanomaterials are a bridge that links single elements with single crystalline bulk structures. Quantum mechanics has successfully described the electronic structures of single elements and single crystalline bulks. The well established bonding, such as ionic, covalent, metallic and secondary, are the basis of solid state structure. The theory for transition in energy levels from discrete for fundamental elements to continuous bands for bulk is the basis of many electronic properties. This is an outstanding question in basic science. Thus, a thorough understanding on the structure of nanocrystals can provide deep insight in the structural evolution from single atoms to crystalline solids.

Nucleation and growth are two important processes in synthesizing thin solid films. Nucleation is a process in which an aggregation of atoms is formed, and is the first step of phase transformation. The growth of nuclei results in the formation of large crystalline particles. Therefore, study of nanocrystals and its size-dependent structures and properties is a key in understanding the nucleation and growth of crystals.

1.1.2 Quantum confinement

A specific parameter introduced by nanomaterials is the surface/interface-to-volume ratio. A high percentage of surface atoms introduces many size-dependent phenomena. The finite size of the particle confines the spatial distribution of the electrons, leading to the quantized energy levels due to size effect. This quantum confinement has applications in semiconductors, optoelectronics and non-linear optics. Nanocrystals provide an ideal system for understanding quantum effects in a nanostructured system, which could lead to major discoveries in solid state physics.

The spherical-like shape of nanocrystals produces surface stress (positive or negative), resulting in lattice relaxation (expansion or contraction) and change in lattice constant [7]. It is known that the electron energy band structure and bandgap are sensitive to lattice constant. The lattice relaxation introduced by nanocrystal size could affect its electronic properties.

1.1.3 Size and shape dependent catalytic properties

The most important application of nanocrystals has been in catalysis. A larger percentage of surface atoms greatly increases surface activities. The unique surface structure, electronic states and largely exposed surface area are required for stimulating and promoting chemical reactions. The size-dependent catalytic properties of nanocrystals have been widely studied, while investigations on the shape (facet)-dependent catalytic behavior are cumbersome. The recent success in synthesizing shape-controlled nanocrystals, such as the ones dominated by {100}, {111} [8] and even {110} facets [9], is a step forward in this field.

1.1.4 Novel mechanical properties

It is known that mechanical properties of a solid depend strongly on the density of dislocations, interface-to-volume ratio and grain size. An enhancement in damping capacity of a nanostructured solid may be associated with grain-boundary sliding [10] or with energy dissipation mechanism localized at interfaces [11] A decrease in grain size significantly affects the yield strength and hardness [12]. The grain boundary structure, boundary angle, boundary sliding and movement of dislocations are important factors that determine the mechanical properties of the nanostructured materials. One of the most important applications of nanostructured materials is in superplasticity, the capability of a polycrystalline material to undergo extensive tensible deformation without necking or fracture. Grain boundary diffusion and sliding are the two key requirements for superplasticity.

1.1.5 Unique magnetic properties

The magnetic properties of nano-size particles differ from those of bulk mainly in two points. The large surface-to-volume ratio results in a different local environment for the surface atoms in their magnetic coupling/interaction with neighboring atoms, leading to the mixed volume and surface magnetic characteristics. Unlike bulk ferromagnetic materials, which usually form multiple magnetic domains, several small ferromagnetic particles could consist of only a single magnetic domain. In the case of a single particle being a single domain, the superparamagnetism occurs, in which the magnetizations of the particles are randomly distributed and they are aligned only under an applied magnetic field, and the alignment disappears once the external field is withdrawn. In ultra-compact information storage [13, 14], for example, the size of the domain determines the limit of storage density. Magnetic nanocrystals have other important applications such as in color imaging [15], bioprocessing [16], magnetic refrigeration [17], and ferrofluids [18].

Metallic heterostructured multilayers comprised of alternating ferromagnetic and nonmagnetic layers such as Fe-Cr and Co-Cu have been found to exhibit giant magnetoresistance (GMR), a significant change in the electrical resistance experienced by current flowing parallel to the layers when an external magnetic field is applied [19]. GMR has important applications in data storage and sensors.

1.1.6 Crystal-shape-dependent thermodynamic properties

The large surface-to-volume ratio of nanocrystals greatly changes the role played by surface atoms in determining their thermodynamic properties. The reduced coordination number of the surface atoms greatly increases the surface energy so that atom diffusion occurs at relatively lower temperatures. The melting temperature of Au particles drops to as low as ~ 300 °C for particles with diameters of smaller than 5 nm, much lower than the bulk melting temperature 1063 °C for Au [20]. Nanocrystals usually have faceted shape and mainly enclosed by low index crystallographic planes. It is possible to control the particle shape, for example, cubic Pt nanocrystals bounded by {100} facets and tetrahedral Pt nanocrystals enclosed by {111} facets [8]. The rod-like Au nanocrystals have also been synthesized, which are enclosed by {100} and {110} facets [9]. The density of surface atoms changes significantly for different crystallographic planes, possibly leading to different thermodynamic properties.

1.1.7 Semiconductor quantum dots for optoelectronics

Semiconductor nanocrystals are zero-dimensional quantum dots, in which the spatial distribution of the excited electron-hole pairs are confined within a small volume, resulting in the enhanced non-linear optical properties [21–24]. The density of states concentrates carriers in a certain energy range, which is likely to increase the gain for electro-optical signals. The quantum confinement of carriers converts the density of states to a set of discrete quantum levels. This is fundamental for semiconductor lasers.

With consideration the small size of a semiconductor nanocrystal, its electronic properties are significantly affected by the transport of a single electron, giving the possibility of producing single electron devices [25]. This is likely to be important in quantum devices and nanoelectronics, in which the size of the devices are required to be in the nanometer range.

Nanostructured porous silicon has been found to give visible photoluminescence [27, 28]. The luminescence properties of silicon can be easily integrated with its electronic properties, possibly leading to a new approach for opto-electronic devices. The mechanism has been proposed to be associated with either quantum confinement or surface properties linked with silica. This is vitally important to integrate optical circuits with silicon based electronics. The current research has been concentrated on understanding the mechanism for luminescence and improving its efficiency.

1.1.8 Quantum devices for nanoelectronics

As the density of logic circuits per chip approaching 10^8, the average distance between circuits is 1.7 μm, between which all of the circuit units and interconnects must be accommodated. The size of devices is required to be less than 100 nm and the width of the interconnects is less than 10 nm. The miniaturization of devices breaks the fundamentals set by classical physics based on the motion of particles. Quantum mechanical phenomena are dominant, such as the quantization of electron energy levels (e.g., the 'particle in a box' quantum confinement problem), electron wave function interference, quantum tunneling between the energy levels belonging to two adjacent nanostructures, and discreteness of charge carriers (e.g., single electron conductance). The quantum devices rely on tunneling through the classically forbidden energy barriers. With an appropriate voltage bias across two nanostructures, the electron energy levels belonging to the two nanostructures line up and resonance tunneling occurs, resulting in an abrupt increase in tunneling current. The single-electron electronics uses the energy required to transport a single electron to operate a switche, transistor or memory element.

These new effects not only raise fundamental questions in physics, but also call on challenges in new materials. There are two outstanding material's issues. One is the semiconductor nanocrystals suitable for nanoelectronics. Secondly, for the operation of high density electronics system, new initiatives must be made to synthesize interconnects, with minimum heat dissipation, high strength and high resistance to electromigration. The most challenging problem is how to manipulate the nanostructures in assembling devices. This is not only an engineering question but rather a science question because of the small size of the nanostructures.

Semiconductor heterostructures are usually referred to as one-dimensional artificially structured materials composed of layers of different phases/compositions. This multilayered material is particularly interesting if the layer thickness is less than the mean-free-pathlength of the electron, providing an ideal system for quantum well structure. The semiconductor heterostructured material is the optimum candidate for fabricating electronic and photonic nanodevices [28].

1.1.9 Carbon fullerences and nanotubes

Research in nanomaterials opens many new challenges both in fundamental science and technology. The discovery of C_{60} fullerence [29], for example, has sparked a great research effort in carbon related nanomaterials. Besides diamond and graphite structures, fullerence is a new state of carbon. The current most stimulating research focuses on carbon nanotubes, a long-rod-like structure comprised of cylindrical concentric graphite sheets [30]. The finite dimension of the carbon nanotube and the chirality angle following which the graphite sheet is rolled result in unique electronic properties, such as the ballistic quantum conductance [31], the semiconductor junctions [32], electron field emission [33] etc. The unique tube structure is also likely to produce extraordinarily strong mechanical strength and extremely high elastic limit. The reversible buckling of the tube results in high mechanical flexibility.

Fullerence and carbon nanotubes can be chemically functionalized and they can serve as the sites/cells for nano-chemical reaction [34]. The long, smooth and uniform cylindrical structure of the nanotube is ideal for probe tips in scanning tunneling microscopy and atomic force microscopy [35]. The covalent bonding of the carbon atoms and the functionalized nanotube tip gives the birth of the chemical microscopy [36], which can be used to probe the local bonding, bond-to-bond interactions and chemical forces.

1.1.10 Ordered self-assembly of nanocrystals

Size and even shape selected nanocrystals behave like a molecular matter, and are ideal building blocks for two- and three-dimensional cluster self-assembled superlattice structures [37–40]. The electric, optical, transport and magnetic properties of the structures depend not only on the characteristics of individual nanocrystals, but also on the coupling and interaction among the nanocrystals arranged with long-range translational and even orientational order [41, 42]. Self-assembled arrays involve self-organization into monolayers, thin films, and superlattices of size-selected nanocrystals encapsulated in a protective compact organic coating. Nanocrystals are the hard cores that preserve ordering at the atomic scale; the organic molecules adsorbed on their surfaces serve as the interparticle molecular bonds and as protection for the particles in order to avoid direct core contact with a consequence of coalescing. The interparticle interaction can be changed via control over the length of the molecular chains. Quantum transitions and insulator to conductor transition could be introduced, possibly resulting in tunable electronic, optical and transport properties [43].

1.1.11 Photonic crystals for optically-active devices and circuits

Photonic crystals are synthetic materials that have a patterned periodic dielectric constant that creates an optical bandgap in the material [44]. To understand the mechanism of photonic crystals, one starts from the energy band structure of electrons in a crystalline solid. Using the Fermi velocity of the electrons in a solid, it can be found that the electron wavelength is compatible to the spacing between the atoms. Electron motion in a periodic potential results in the quantized energy levels. In the energy regions filled with energy levels, bands are formed. An energy gap between the conduction band and the valence band would be formed, which is a key factor in deter-

mining the conductivity of the solid. If the bandgap is zero, the material is conductive; for a small bandgap, the material is semiconductor; and the material is insulator if the bandgap is large.

The wavelength of photons is in the order of a few hundreds of nanometers. It is necessary to artificially create a dielectric system which has periodically modulated dielectric function at a periodicity compatible with the wavelength of the photon. This can be done by processing materials that are comprised of patterned structures. As a result, photons with energies lying within the bandgap cannot be propagated unless a defect causes an allowed propagation state within the bandgap (similar to a defect state), leading to the possibility of fabricating photon conductors, semiconductors and insulators. Thus point, line, or planar defects can be shown to act as optical cavities, waveguides, or mirrors and offer a completely different mechanism for the control of light and advancement of all-optical integrated circuits [45–47]. By using particles sizes in the nanometer regime with different refractive indices than the host material, these effects should be observable in the near infrared and visible spectral regions.

1.1.12 Mesoporous materials for low-loss dielectrics and catalysis

Mesoporous materials can be synthesized by a wide range of techniques such as chemical etching, sol gel processing and template-assisted techniques. Ordered self-assembly of hollow structures of silica [48], carbon [49] and titania [50, 51] has drawn much attention recently because of their applications in low-loss dielectrics, catalysis, filtering and photonics. The ordered hollow structure is made through a template-assisted technique. The monodispersive polystyrene (PS) particles are used as the template to form an ordered, self-assembled periodic structure. Infiltrating the template by metal-organic liquid and a subsequent heat treatment form the ordered pores, whose walls are metal oxides. The structure is ordered on the length-scale of the template spheres and the pore sizes are in submicron to micron range. Alternatively, ordered porous silica with much smaller pore sizes in nanosize range (< 30 nm), produced deliberately by introducing surfactant, has also been processed [52, 53], in which the porosity is created by surfactants. A combination of the template assisted pore structure and the surfactant introduced in the infiltration liquid results in a new structure that have porousity at double-length scales [54]. The low density (~ 10% of the bulk density) of the material results in very low dielectric constant, a candidate for low-loss electronic devices. The large surface area of the porous materials is ideal for catalysis. The synthesis of mesoporous materials can be useful for environmental cleaning [55] and energy storage [56].

1.2 Characterization of nanophase materials

There are three key steps in the development of nanoscience and nanotechnology: materials preparation, property characterization, and device fabrication. Preparation of nanomaterials is being advanced by numerous physical and chemical techniques. The purification and size selection techniques developed can produce nanocrystals with well defined structure and morphology. The current most challenging tasks are property characterization and device fabrication. Characterization contains two main

categories: structure analysis and property measurements. Structure analysis is carried out using a variety of microscopy and spectroscopy techniques, while the property characterization is rather challenging.

Due to highly size and structure selectivity of the nanomaterials, the physical properties of nanomaterials could be quite diverse. To maintain and utilize the basic and technological advantages offered by the size specificity and selectivity of nanomaterials, it is imperative to understand the principles and methodologies for characterization the physical properties of individual nanoparticles/nanotubes. It is known that the properties of nanostructures depend strongly on their size and shape. The properties measured from a large quantity of nanomaterials could be an average of the over all properties, so that the unique characteristics of individual nanostructure could be embedded. The ballistic quantum conductance of a carbon nanotube [31] (Fig. 1-1), for example, was observed only from defect-free carbon nanotubes grown by an arc-discharge technique, while such an effect vanishes in the catalytically grown carbon nanotubes [57, 58] because of high density of defects. This effect may have great impact on molecular electronics, in which carbon nanotubes could be used as interconnects for molecular devices with no heat dissipation, high mechanical strength and flexibility. The covalent bonding of the carbon atoms is also a plus for molecular device because of the chemical and bonding compatibility. Therefore, an essential task in nanoscience is property characterization of an individual nanostructure with well defined atomic structure.

Characterizing the properties of individual nanoparticle/nanotube/nanofiber (e.g., nanostructure) is a challenge to many existing testing and measuring techniques because of the following constrains. First, the size (diameter and length) is rather small, prohibiting the applications of the well-established testing techniques. Tensile and creep testing of a fiber-like material, for example, require that the size of the sample be sufficiently large to be clamped rigidly by the sample holder without sliding. This is impossible for nanostructured fibers using conventional means. Secondly, the small size of the nanostructures makes their manipulation rather difficult, and specialized techniques are needed for picking up and installing individual nanostructure. Finally, new methods and methodologies must be developed to quantify the properties of individual nanostructures.

Mechanical characterization of individual carbon nanotubes is a typical example. By deflecting on one-end of the nanofiber with an AFM tip and holding the other end fixed, the mechanical strength has been calculated by correlating the lateral displacement of the fiber as a function of the applied force [59, 60]. Another technique that

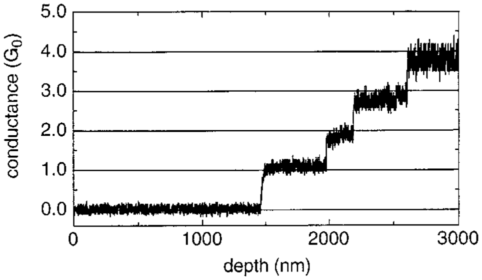

Figure 1-1. Quantized conductance of a multiwalled carbon nanotube observed as a function of the depth into the liquid mercury the nanotube was inserted in an atomic force microscope, where $G_0 = 2e^2/h = (12.9\ \mathrm{k}\Omega)^{-1}$ is the quantum mechanically predicted conductance for a single channel (Courtesy of Walt de Heer, Georgia Institute of Technology).

has been previously used involves measurement of the bending modulus of carbon nanotubes by measuring the vibration amplitude resulting from thermal vibrations [61], but the experimental error is quite large. A new technique has been demonstrated recently for measurement the mechanical strength of single carbon nanotubes using in-situ TEM [62]. The measurements is done on a specific nanotube whose microstructure is determined by transmission electron imaging and diffraction. If an oscillating voltage is applied on the nanotube with ability to tune the frequency of the applied voltage, the periodic force acting on the nanotube induces electro-mechanical resonance (Fig. 1-2). The resonance frequency is an accurate measure of the mechanical modulus.

In analogous to a spring oscillator, the mass of the particle attached at the end of the spring can be determined if the vibration frequency is measured, provided the spring constant is calibrated. This principle can be adopted to determine the mass of a very tiny particle attached at the tip of the free end of the nanotube (Fig. 1-3). This newly discovered "nanobalance" has been shown to be able to measure the mass of a particle as small as 22 ± 6 fg (1f = 10^{-15}) [62]. *The most sensitive and smallest balance in the world.* The nanobalance is anticipated to be useful for measuring the mass of a large biomolecule or biomedical particle, such as virus.

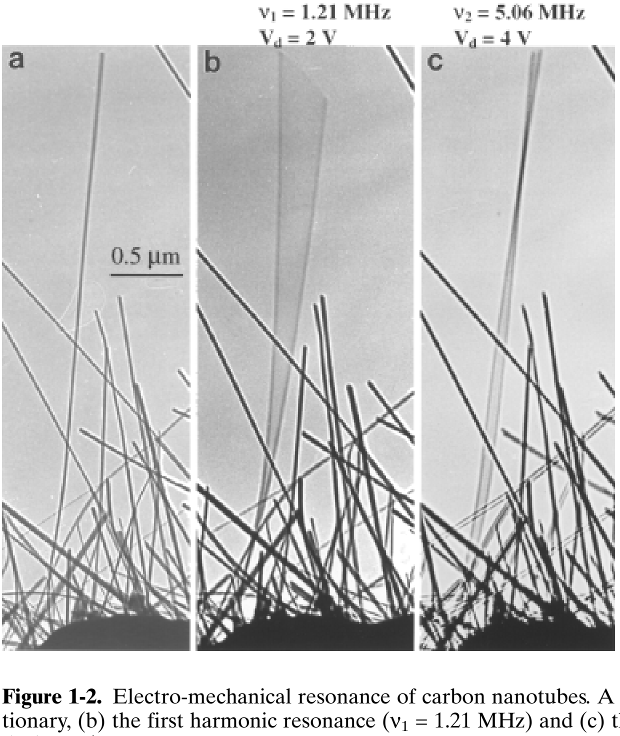

Figure 1-2. Electro-mechanical resonance of carbon nanotubes. A selected carbon nanotube at (a) stationary, (b) the first harmonic resonance (ν_1 = 1.21 MHz) and (c) the second harmonic resonance (ν_2 = 5.06 MHz).

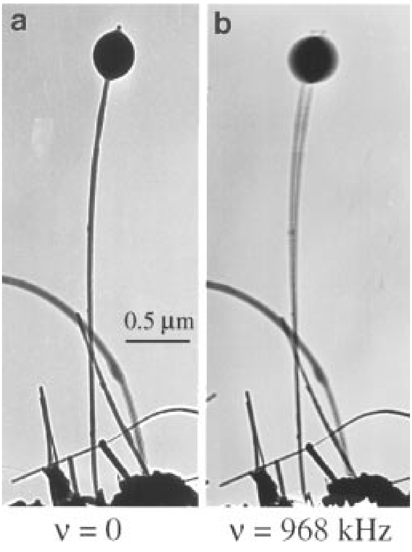

Figure 1-3. A small particle attached at the end of a carbon nanotube at (a) stationary and (b) first harmonic resonance (ν = 0.968 MHz). The effective mass of the particle is measured to be ~ 22 fg (1 f = 10^{-15}).

1.3 Scope of the book

Development of nanotechnology involves several key steps. First, synthesis of size and even shape controlled nanoparticles is the key for developing nanodevices. Second, characterization of nanoparticles is indispensable to understand the behavior and properties of nanoparticles, aiming at implementing nanotechnology, controlling their behavior and designing new nanomaterial systems with super performance. Third, theoretical modeling is vitally important to understand and predict material's performance. Finally, the ultimate goal is to develop devices using nanomaterials. With consideration the large diversity of research in nanomaterials, this book concentrates on the structure and property characterization of nanomaterials.

The book emphasizes the techniques used for characterizing nanophase materials, including x-ray diffraction, transmission electron microscopy, scanning transmission electron microscopy, scanning probe microscopy, optical, electrical and electrochemical characterizations. The book aims at describing the physical mechanisms and detailed applications of these techniques for characterizations of nanophase materials to fully understand the morphology, surface and the atomic level microstructures of nanomaterials and their relevant properties. It is also intended as a guidance with introduction of the fundamental techniques for structure analysis. The book focuses also on property characterization of nanophase materials in different systems, such as the family of metal, semiconductor, magnetic, oxide and carbon systems. It is the key to illustrate the unique properties of the nanocrystals and emphasize how the structures and the properties are characterized using the techniques presented in the book.

References

[1] M.A. Kastner, *Phys. Today*, **1993**, *46*, 24.
[2] L. Brus, *Appl. Phys. A*, **1991**, *53*, 465.
[3] L.N. Lewis, *Chem. Rev.*, **1993**, *93*, 2693.
[4] R. Freer, *Nanoceramics* London, Institute of Materials, **1993**.
[5] D.D. Awschalom and D.P. DiVincenzo, *Phys. Today*, **1995**, *48*, 43.
[6] J.F. Smyth, *Science*, **1992**, *258*, 414.
[7] J. Woltersdorf,, A.S. Nepijko, and E. Pippel, *Surf. Sci.*, **1981**, *106*, 64.
[8] T.S. Ahmadi, Z.L. Wang, T.C. Green, A. Henglein and M.A. El-Sayed, *Science*, **1996**, *272*, 1924.
[9] M. Mahamed, Z.L. Wang and M.A. El-Sayed, *J. Phys. Chem. B*, **1999**, submitted.
[10] B.S. Berry and W.C. Pritchett, *Thin Solid Films*, **1976**, *33*, 19.
[11] C.M. Su, R.R. Oberle, M. Wuttig, and R.C. Cammarata, *Mater. Res. Soc. Symp. Proc.* **1993**, *280*, 527.
[12] for a review see J.R. Weertman and R.S. Averback, in *Nanomaterials: Synthesis, Properties and Applications*, eds. A.S. Edelstein and R.C. Cammarata, London, Institue of Phys. Publ., **1996,** Chapter 13, 323, and references therein.
[13] L. Gunther, *Phys. World*, **1990**, *3*, 28.
[14] R.G. Audran and A.P. Huguenard, *U.S. Patent*, **1981**, 4,302,523.
[15] R.F. Ziolo, *U.S. Patent*, **1984**, 4,474,866.
[16] R.H. Marchessault, S. Ricard and P. Rioux, *Carbohydrate Res.*, **1992**, *224*, 133.
[17] R.D. McMichael, R.D. Shull, L.J. Swartzendruber, L.H. Bennett, R.E. Watson, *J. Magn. Magnsm Mater.*, **1992**, *111*, 29.
[18] I. Anton et al., *J. Magn. Magnsm Mater.*, **1990**, *85*, 219.
[19] M.N. Baibich, J.M. Broto, A. Fert, F. Nguyen Van dau, F. Petroff, P. Etienne, G. Greuzet, A. Friederich, and J. Chazelas, *Phys. Rev. Letts.*, **1988**, *61*, 2472.
[20] Ph. Buffat, J.P. Borel, *Phys. Rev. A*, **1976**, *13*, 2287.
[21] S.M. Prokes, *Appl. Phys. Lett.*, **1993**, *62*, 3244.
[22] L. Brus, *Appl. Phys. – Mater. Sci. & Processing*, **1991**, *53*, 465.
[23] A.P. Alivisatos, *Science*, **1996**, *271*, 933.
[24] C.B., Murray, D.J. Norris, M.G. Bawendi, *J. of American Chemical Society*, **1993**, *115*, 8706.
[25] D.L. Klein, R. Roth, A.K.L. Lim, A.P. Alivisatos, P.L. McEuen, *Nature*, **1997**, *389*, 699.
[26] C. Pickering, M.I.J. Beale, D.J. Robbins, P.J. Pearson and R. Greef, *J. Phys. C: Solid State Phys.*, **1984**, *17*, 6536.
[27] L.T. Canham, *Appl. Phys. Lett.*, **1990**, *57*, 1046.
[28] for a review see R.C. Cammarata, in *Nanomaterials: Synthesis, Properties and Applications*, eds. A.S. Edelstein and R.C. Cammarata, London, Institue of Phys. Publ., **1996**, Chapter 13, 323, and references therein.
[29] H.W. Kroto, J.R. Heath, S.C. O'Brien, R.F. Curl and R.F. Smalley, *Nature*, **1985**, *318*, 162.
[30] S. Iijima, *Nature*, **1991**, *354*, 56.
[31] S. Frank, P. Poncharal, Z.L. Wang and W.A. de Heer, *Science*, **1998**, *280*, 1744.
[32] S.J. Tans, A.R.M. Verschueren, C. Dekker, *Nature*, **1998**, *393*, 49.
[33] W. A. de Heer, A. Chatelain, D. Ugarte, *Science*, **1995**, *270*, 1179.
[34] W.Q. Han, S.S. Fan, Q.Q. Li and Y.D. Hu, *Science*, **1997**, *277*, 1287.
[35] H. Dai, J.H. Hafner, A.G. Rinzler, D.T. Colbert, R.E. Smalley, *Nature*, **1996**, *384*, 147.
[36] S.S. Wong, E. Joselevich, A.T. Woolley, C.L. Cheung, C.M. Lieber, *Nature*, **1998**, *394*, 52.
[37] R.L. Whetten, J.T. Khoury, M.M. Alvarez, S. Murthy, I. Vezmar, Z.L. Wang, C.C. Cleveland, W.D. Luedtke, U. Landman, *Adv. Materials*, **1996**, *8*, 428.
[38] J.S. Yin and Z.L. Wang, *Phys. Rev. Lett.*, **1997**, *79*, 2570.
[39] C.B. Murray, C.R. Kagan, M.G. Bawendi, *Science*, **1995**, *270*, 1335.
[40] S. Sun and C.B. Murray, *J. Appl. Phys.* **1999**, *85*, 4325.
[41] Z.L. Wang, *Adv. Mater.*, **1998**, *10*, 13.
[42] S.A. Harfenist, Z.L.Wang, M.M.Alvarez, I.Vezmar and R.L.Whetten, *J. Phys. Chem.*, **1996**, *100*, 13904.
[43] C.P. Collier, R.J. Saykally, J.J. Shiang, S.E. Henrichs and J.R. Heath, *Science*, **1997**, *277*, 1978.
[44] J.D. Joannopoulos, P.R. Villeneuve and S. Fan, *Nature*, **1997**, *386*, 143.
[45] F. Gadot F, A. Chelnokov, A. DeLustrac, P. Crozat, J.M. Lourtioz, D. Cassagne, C. Jouanin, *Appl. Phys. Letts.*, **1997**, *71*, 1980.
[46] T.F. Krauss, R.M. DeLaRue, S. Brand, *Nature*, **1996**, *383*, 699.
[47] D.F. Sievenpiper, M.E. Sickmiller, E. Yablonovitch E, *Phys. Rev. Letts.,* **1996**, *76*, 2480.
[48] O.D. Velev, T.A. Jede, R.F. Lobo and A.M. Lenhoff, *Nature*, **1997**, *389*, 448.

[49] A.Z. Zakhidov, R.H. Baughman, Z. Iqbal, C. Cui, I. Khayrullin, S.O. Dantas, J. Marti, and V.G. Ralchenko, *Science*, **1998**, *282*, 897.
[50] J.E.G.J. Wijnhoven and W.L. Vos, *Science*, **1998**, *281*, 802.
[51] B.T. Holland, C.F. Blanford and A. Stein, *Science*, **1998**, *281*, 538.
[52] C.T. Kresge, M.E. Leonowioz, W.J. Roth, J.C. Vartuli and J.S. Beck, *Nature*, **1992**, *359*, 710.
[53] D. Zhao, J. Feng, Q. Huo, N. Melosh, G.H. Fredrickson, B.F. Chmelka and G.D. Stucky, *Science*, **1998**, *279*, 548.
[54] J.S. Yin and Z.L. Wang, *Appl. Phys. Letts.*, **1999**, *74*, 2629.
[55] X. Feng, G.E. Fryxell, L.Q. Wang, A.Y. Kim, J. Liu, K.M. Kemner, *Science*, **1997**, *276*, 923.
[56] U. Bach, D. Lupo, P. Comte, J.E. Moser, F. Weissortel, J. Salbeck, H. Spreitzer, M. Gratzel, *Nature*, **1998**, *395*, 583.
[57] H.J. Dai, E.W. Wong, C.M. Lieber, *Science*, **1996**, *272*, 523.
[58] T.W. Ebbesen, H.J. Lezec, H. Hiura, J.W. Bennett, H.F. Ghaemi, T. Thio, *Nature*, **1996**, *382*, 54.
[59] E. Wong, P. Sheehan and C. Lieber, *Science*, **1997**, *277*, 1971.
[60] J.P. Salvetat, A.J. Kulik, J.M. Bonard, G.A.D. Briggs, T. Stockli, K. Metenier, S. Bonnamy, F. Beguin, N.A. Burnham, L. Forro, *Adv. Materials*, **1999**, *11*, 161.
[61] M.M. Treacy, T.W. Ebbesen, J.M. Gibson, *Nature*, **1996**, *38*, 678.
[62] P. Poncharal, Z.L. Wang, D. Ugarte and W.A. de Heer, *Science*, **1999**, *283*, 1513.

Characterization of Nanophase Materials. Edited by Zhong Lin Wang
Copyright © 2000 Wiley-VCH Verlag GmbH
ISBNs: 3-527-29837-1 (Hardcover); 3-527-60009-4 (Electronic)

2 X-ray Characterization of Nanoparticles

Daniela Zanchet, Blair D. Hall, and Daniel Ugarte

2.1 Introduction

The hunt for new applications of nanostructured systems is now a major area of research in materials science and technology. To exploit the full potential that nanosystems offer, it is important that novel methods of manipulation and fabrication be developed, in addition to extending current techniques of sample characterization to smaller sizes. Success in devising and assembling systems on the scale of nanometers will require a deeper understanding of the basic processes and phenomena involved. Hence, one of the current key objectives is to adapt and develop a range of techniques that can characterize the structural, electronic, magnetic and optical properties of nanostructured systems. High-resolution techniques, that provide local information on the nanometer scale (such as electron or scanning probe microscopies), as well as those that provide only ensemble-average measurements, are all important in obtaining a complete picture of material properties.

One of the most fundamental characteristics of nanometer-sized particles is their very high surface-to-volume ratio. This can lead to novel and unexpected atomic arrangements, and may also have dramatic effects on other physical or chemical attributes. Because of this, the precise determination of nanoparticle structure, both medium-range order and/or the existence of local distortion, is a fundamental issue. Methods of structure determination can be broadly classified in two categories, depending on the use of real or reciprocal space data. Direct space methods allow the visualization of the atomic arrangement in nanometer-sized regions; the most vivid examples are: High Resolution Transmission Electron Microscopy (HRTEM) and Scanning Probe Microscopies (Scanning Tunneling Microscopy; Atomic Force Microscopy; etc). Reciprocal space-based methods exploit interference and diffraction effects of photons or electrons, to provide sample-averaged information about structure. For most bulk material-related studies, reciprocal space methods are much easier to apply than direct methods, disposing of numerous, flexible, mathematical tools to fully exploit the experimental data.

In fact, it must be recognized that X-ray diffraction (XRD), based on wide-angle elastic scattering of X-rays, has been the single most important technique for determining the structure of materials characterized by long-range order [1]. However, for other systems, such as disordered materials, XRD has been of limited use, and other experimental techniques have had to be developed. A particularly powerful example is the technique of EXAFS (Extended X-ray Absorption Fine Structure) [2], which probes the local environment of a particular element. Although this method is, as XRD, reciprocal space-based, it is essentially a spectroscopic technique, exploiting the energy-dependence of X-ray absorption due to interference effects in the individual photoelectron scattering process. This fact allows precise measurement of a local environment without the necessity of long-range order in the material.

Small-angle elastic X-ray scattering (SAXS) can provide direct information about the external form of nanoparticles or macromolecules, by measuring the typical size of the electron density variations [3]. For example, SAXS measurements can be used

to estimate the radius of gyration of particles, giving information related to the average particle diameter. The applicability of this technique depends on both detection range and X-ray beam divergence: in general, it can be applied to determine the size, or even size distribution, of nanoparticles in the 1–200 nm range.

This chapter will discuss structural characterization of nanostructured materials using X-rays. Many techniques, of varying degrees of complexity, could be presented here, however, it is not our intention to review all available experimental methods. Instead, we wish to highlight problems that can arise when well-established methods of measurement, or treatment of data, for the bulk are applied to nanosystems. To do this, we will analyze the structure of a sample of 2 nm gold particles using both XRD and EXAFS. SAXS studies are not included in our discussion as their size-range of applicability is already well suited to nanoparticle studies; readers are referred to existing texts describing this technique [3, 4].

XRD and EXAFS are both reciprocal space-based methods usually applied to comparatively large amounts of sample (~ mm^3). They are both capable of providing information on the average behavior of nanoparticle samples, however, they differ in the nature of X-ray interaction with matter (elastic or inelastic), and give two relatively complementary types of information (long-to-medium range, versus local order, respectively). We will concentrate on the application of these techniques to nanosystems, and the special considerations that must be taken into account when doing so. The discussion should enable the reader to get an idea of the general aspects involved in characterizing nanosized-volumes of matter, and thereby understand how to optimize experiments and data processing to fully exploit the capacities of these powerful techniques.

2.2 X-ray sources

Since their discovery, at the end of last century, X-ray tubes have not changed in their basic principle of operation. A beam of energetic electrons is directed onto a solid target (Copper, Molybdenum, etc), generating X-ray photons. The resulting X-ray energy spectrum is made up of intense narrow fluorescent lines (white lines), characteristic of the target material, and a less intense continuous spectrum (Bremsstrahlung) [1].

This simple type of device has allowed the development of extremely powerful crystallographic methods that have been used extensively to determine material structure by diffraction experiments. As already mentioned, XRD involves the elastic scattering of photons; it requires a collimated, and rather monochromatic, incident X-ray beam. These conditions can be reasonably well met by using the characteristic lines of X-ray tubes. For many years, experimental methods have been limited by the discrete nature of the energy distribution of the conventional X-ray tubes. However, in the last few decades, synchrotron facilities characterized by high intensity, enhanced brightness, and a continuous energy spectrum, have been developed. Such sources, combined with efficient and flexible X-ray optics (mirrors, monochromators, slits, etc.), can supply a monochromatic beam of X-rays for which continuous variation of the energy is possible. This has stimulated the emergence of new techniques of analysis, among them spectroscopic techniques, such as EXAFS [5].

Usually, in nanophase materials or nanoparticles, the actual amount of matter constituting the nanometric sized volumes is extremely small. As a consequence, most experimental techniques used for characterization are limited by the poor quality of

signal that can be obtained. For X-ray methods, this becomes critical and the use of the modern synchrotron sources is almost a prerequisite to obtain good quality data. In the sections that follow, we describe the results of experiments performed at the Brazilian National Synchrotron Laboratory (LNLS), where conventional X-ray optics and experimental set-ups for powder diffraction, and X-ray absorption spectroscopy were used; no special apparatus was employed for these measurements on nanosystems.

2.3 Wide-angle X-ray diffraction

2.3.1 Diffraction from small particles

The distribution of X-ray intensity scattered by a finite-sized atomic aggregate takes on a simple form, provided that aggregates within the sample are uniformly and randomly oriented with respect to the incident beam. Under these conditions, a radially symmetric powder diffraction pattern can be observed.

Powder diffraction patterns for individual particle structures can be calculated using the Debye equation of kinematic diffraction [6]. For aggregates containing only one type of atom, the Debye equation is expressed as:

$$I_{\mathrm{N}}(s) = I_0 N f^2(s)\left(1 + \frac{D}{N}\sum_{\mathrm{n}\neq \mathrm{m}} \frac{(\sin 2\pi s r_{\mathrm{mn}})}{2\pi s r_{\mathrm{mn}}}\right) \tag{2-1}$$

where I_0 is the intensity of the incident beam and $I_{\mathrm{N}}(\mathrm{s})$ is the power scattered per unit solid angle in the direction defined by $s = 2\sin(\theta)/\lambda_{\mathrm{p}}$, with θ equal to half the scattering angle and λ_{p} the wavelength of the radiation. The scattering factor, $f(s)$, determines the single-atom contribution to scattering, and is available in tabulated form [7]. N is the number of atoms in the cluster and r_{mn} is the distance between atom m and atom n. The Debye-Waller factor, D, damps the interference terms and so expresses a degree of disorder in the sample. This disorder may be dynamic, due to thermal vibrations, or static, as defects in the structure. A simple model assumes that the displacement of atoms is random and isotropic about their equilibrium positions. In this case,

$$D = \exp\left(-(2\pi s \Delta x)^2\right) \tag{2-2}$$

where Δx is the rms atomic displacement from equilibrium along one Cartesian coordinate [6].

The Debye equation is actually in the form of a three dimensional Fourier transform, in the case where spherical symmetry can be assumed. As such, some feeling for the details of powder diffraction patterns can be borrowed from simple one-dimensional Fourier theory. Firstly, at very low values of s, the reciprocal space variable, one can expect to find the low-frequency components of the scatterer structure. This is the small-angle scattering region, in which information about the particle size and external form is concentrated. No details of the internal atomic arrangements are contained in the small-angle intensity distribution (see [3,4,6] for a description of small-angle diffraction). Secondly, beyond the small-angle region, intensity fluctuations

arise from interference due to the internal structure of the particle, or domains of structure within it. The size of domains and the actual particle size need not to be the same, so small-angle and wide-angle diffraction data can be considered as complementary sources of information. Thirdly, the finite size of domains will result in the convolution of domain-size information with the more intense features of the internal domain structure. This domain size information will tend to have oscillatory lobes that decay slowly on either side of intense features (examples will be shown below).

2.3.2 Distinctive aspects of nanoparticle diffraction

The very small grain size of clusters in nanophase materials gives their diffraction pattern the appearance of an amorphous material. Of course they are not amorphous: the problem of accurately describing nanoparticle structure is one of the central themes of this text. The difficulty in determining their structure by X-ray diffraction, however, is imposed at a fundamental level by two features of these systems: the small size of structural domains that characterize the diffraction pattern; and the occurrence of highly symmetric, but, non-crystalline structures. In short, the common assumption that there exists some kind of underlying long-range order in the system under study does not apply to nanophase materials. This is most unfortunate because the wealth of techniques available to the X-ray crystallographer must largely be put aside.

Size-dependent and structure-specific features in diffraction patterns can be quite striking in nanometer-sized particles. Small particles have fairly distinct diffraction patterns, both as a function of size and as a function of structure type. In general, regardless of structure, there is a steady evolution in the aspect of diffraction profiles: as particles become larger, abrupt changes do not occur, features grow continuously from the diffraction profile and more detail is resolved. These observations form the basis for a direct technique of diffraction pattern analysis that can be used to obtain structural information from experimental diffraction data. This will be outlined in Section 2.3.3 below.

2.3.2.1 Crystalline particles

Single crystal nanoparticles exhibit features in diffraction that are size-dependent, including slight shifts in the position of Bragg peaks, anomalous peak heights and widths [8]. Figure 2-1 shows the diffraction patterns for three sizes of face-centered-cubic (fcc) particles, spanning a diameter range of 1.6–2.8 nm, and containing from 147 to 561 atoms. The intensities have been normalized, so that the first maximum in each profile has the same height, and shifted vertically, so that the features of each can be clearly seen. Also shown are the positions of the bulk (Bragg) diffraction lines for gold, indexed at the top.

It should be immediately apparent from Fig. 2-1 that there is considerable overlap in the peaks of the particle profiles. In fact, the familiar concept of a diffraction peak begins to loose meaning when considering diffraction from such small particles. On the contrary, Eq. 2-1 shows the diffraction from a small body to be made up of a combination of continuous oscillating functions. This actually has several important consequences, which have been known for some time [8]:

- not all peaks associated with a particular structure are resolved in small crystalline particles;

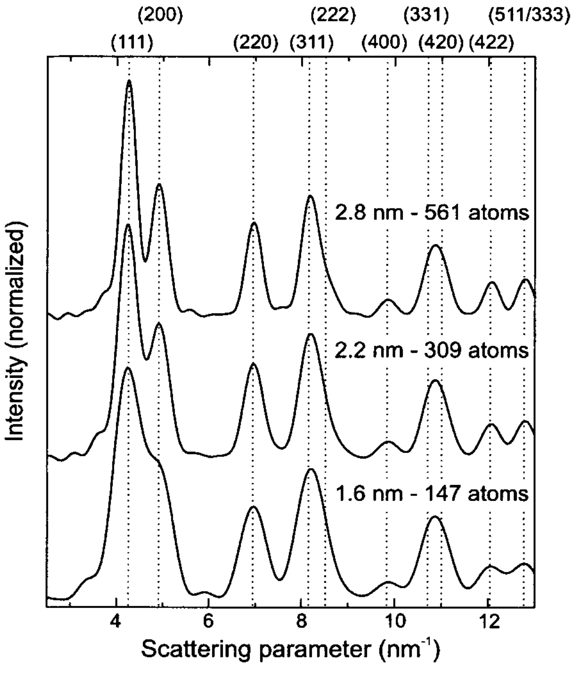

Figure 2-1. Calculated diffraction pattern of three successive sizes of cuboctahedral (fcc) particles. The intensities of the main (111) peak have been normalized to the same value for display, in reality their intensity increases rapidly with size. The baselines of the profiles have also been shifted vertically. At the top of the figure the indices for the Bragg diffraction peaks are shown. The number of atoms per model and the approximate diameters are inset.

- those peaks that are resolved may have maxima that do not align with expected bulk peak positions;
- peak shapes, peak intensities and peak widths may differ from extrapolated bulk estimates;
- few minima in intensity between peaks actually reach zero;
- small, size-related, features appear in the diffraction pattern.

Clearly, to extract quantitative information based on size-limited bulk structure formulae is fraught with difficulty. It means, for example, that an apparent lattice contraction, or expansion, due to a single peak shift may be size related. Also, the familiar Scherrer formula [6], relating particle-size to peak-width, will be difficult to apply accurately [9].

2.3.2.2 Non-crystalline structures

In many metals, distinct structures can occur that are not characteristic of the bulk crystal structure. For most fcc metals, the preferred structures of sufficiently small particles exhibit axes of five-fold symmetry (see schematic representation in Fig. 2-2), which is forbidden in crystals. These Multiply-Twinned Particles (MTPs) were first identified in clusters of gold [10], and have since been well documented in a range of metals [11]. Although MTPs exhibit distinct diffraction patterns, the interpretation of diffraction data can not be made by applying conventional methods of analysis because they lack a uniform crystal structure (e.g.: the location of the maximum in the diffraction peak does not give precise information about the nearest-neighbor distances within the particles [12]. Furthermore, MTPs often co-exist with small fcc parti-

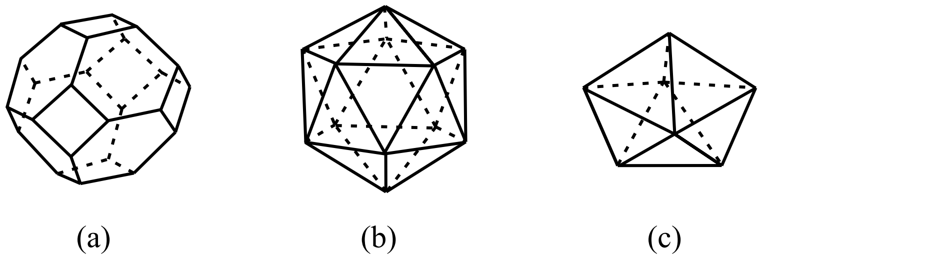

Figure 2-2. Schematic representation of the three possible structures of metal nanoparticles: a) cuboctahedron, formed by a fcc crystal truncated at (100) and (111) atomic planes; b) icosahedron and c) decahedron. b) and c) are known as Multiply-Twinned-Particles (MTPs), characterized by five-fold axes of symmetry.

cles in a single sample. This greatly complicates the problem of determining nanoparticle structure because, in general, it will not be possible to characterize an experimental diffraction pattern by a single particle structure.

The extent to which size and structure can impact on the MTP diffraction patterns can be seen in Fig. 2-3 and Fig. 2-4. These figures show the two distinct MTP structures: the icosahedron [13, 14] and the truncated decahedron [14, 15]. Both of these can be constructed by adding complete shells of atoms to a basic geometry. Individual shells repeat the geometrical form, but with an increasing number of atoms used in the construction. The models below used the inter-atomic distance in bulk gold, with the MTP structures given a uniform relaxation as prescribed by Ino [14]. No Debye-Waller factor was included.

Figure 2-3 shows three sizes of icosahedral particles, in a similar presentation to Fig. 2-1. The icosahedral structure cannot be considered as a small piece of a crystal lattice. However, an icosahedron can be assembled from twenty identical tetrahedral

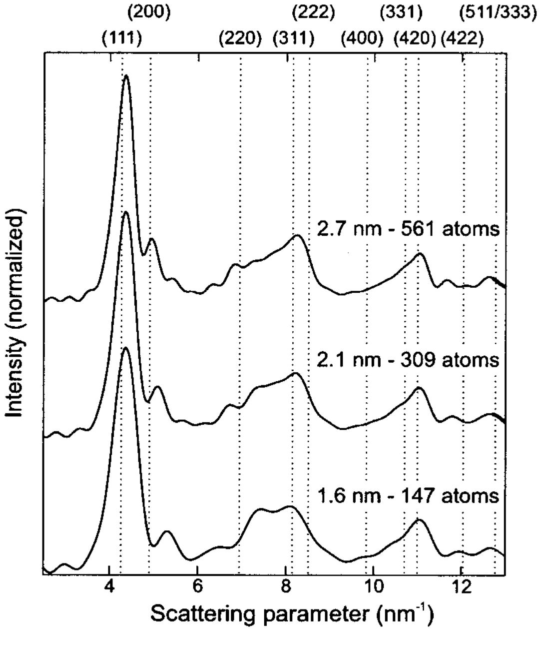

Figure 2-3. The diffraction patterns of three successively larger icosahedra. The intensities of the main peak have been normalized to the same value for display, and the profile baseline shifted. The Bragg indices, that apply to the bulk fcc structure, are shown here only for reference.

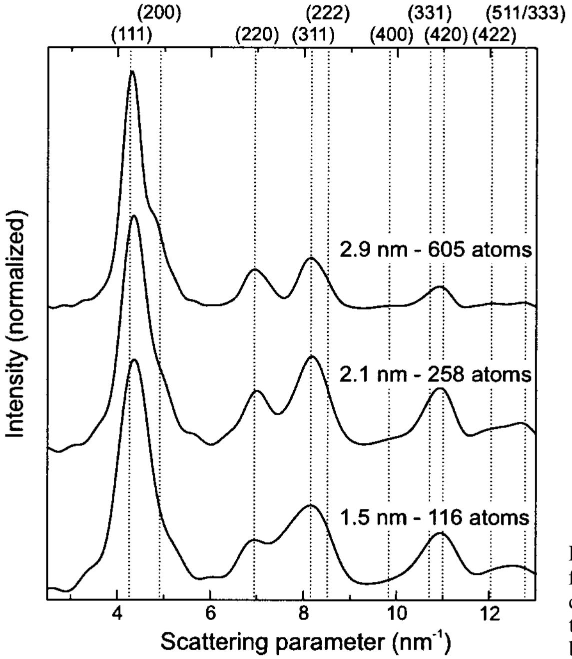

Figure 2-4. Three diffraction patterns from successive sizes of decahedral particles. The fine edges of the decahedra are truncated with (100) planes as suggested by Ino [14].

units, brought together at a common apex in the center of the particle. These tetrahedra are arranged as twins with their three immediate neighbors, so that the complete structure contains thirty twin planes. The individual tetrahedra are exact sub-units of a rhombohedral lattice [16], although it is common to regard them as slightly distorted fcc tetrahedra.

The oscillatory features in Fig. 2-3 (clearly visible at $s \approx 3$ and $s \approx 6$ nm^{-1}) are size-related. In particular, the illusive, shoulder peak, to the right of the diffraction maximum, carries no internal-structure information [17]. It is clear in Fig. 2-3 that these oscillations increase in frequency as the particle size increases. As a result, the prominent shoulder peak moves in, towards the diffraction maximum, as the particle size increases. These size-effects are most obvious in the icosahedral diffraction profiles but occur for each structure type. In general, it is important to consider the consequences of a sample size distribution (something that in practice is almost impossible to avoid) when interpreting diffraction data.

In Fig. 2-3 the bulk fcc Bragg peak locations have been reported for reference again. It can be seen that, in a mixture of structures, an icosahedral component may not clearly distinguish itself, because its contributions to the diffracted intensity profile will be most important in the same regions in which fcc peaks occur. This will be exacerbated by a distribution of sizes: the feature on the right of the main peak will broaden and may form a shoulder on the principal peak, making the latter appear as a single asymmetrical diffraction peak.

Given that the tetrahedral structure of the icosahedral sub-units is crystalline, one might expect the diffraction pattern of icosahedra to be characteristic of that structure. This does happen, but only at much larger sizes: when much larger models are constructed, the rhombohedral lattice peaks start to be resolved [18].

The last in this series of figures shows the diffraction patterns of three truncated decahedral particles (Fig. 2-4). The decahedral structure is the one originally proposed by Ino [14]. The decahedron can be considered as five tetrahedral sub-units, arranged to share a common edge, which forms the five-fold axis of the particle. The five component tetrahedra are in fact perfect sub-units of an orthorhombic crystal, and can be derived from a slightly distorted fcc structure [16]. The narrow external edges formed by the tetrahedra of a perfect geometrical structure are unfavorable energetically. Here, these edges have been truncated by (100) planes according to Ino [14], the more complex surface features proposed by Marks have not been modeled, as they cannot be observed by diffraction [11].

While the general remarks made previously in relation to Figs. 2-1 and 2-3 apply here too, it is apparent that the degree to which Fig. 2-4 differs from Fig. 2-1 is not as great as in the icosahedral case. This is because on the one hand, the distortion of the tetrahedra from fcc to orthorhombic involves less change than does the distortion in the icosahedral structure. On the other hand, there are only five twin planes in the decahedral structure, meaning that the sub-units are relatively larger, compared to the particle diameter, and their structure is more apparent in the diffraction profile.

2.3.3 Direct analysis of nanoparticle diffraction patterns

The Debye equation shows that the diffracted intensity depends on the distribution of inter-atomic distances within the scattering volume. While the internal structure can be used to calculate a set of inter-atomic distances, the converse is not necessarily true. This is a ubiquitous problem in diffraction, but it is worth drawing attention to the present context: if a model diffraction pattern agrees well with observed data, then there is strong evidence that the structure represented by the model characterizes the actual structure of the sample. However, if more than one model structure actually have very similar distributions of inter-atomic distances then diffraction measurements will not be able to distinguish between them.

With this in mind, a direct approach can be used to analyze experimental diffraction data from nanoparticles. We have seen above that quite distinct features are associated with both particle size and structure. Here, there is an opportunity to extract both the structure type and the domain size distribution from an experimental diffraction profile. This is achieved by comparing combinations of model structure diffraction patterns with the experimental data, until a satisfactory match is obtained. Such a procedure neatly handles the problem of sample size dispersion and makes only such assumptions about particle structure as are necessary to construct a series of trial model structures. This method was originally proposed as a way to interpret electron diffraction data of unsupported silver particles [19, 20]. It has come to be known as Debye Function Analysis (DFA) and has been applied since by two groups independently [21–24]. A more complete description of DFA can be found in [25].

It is important to realize that the DFA does not alter the structure of the models in any way: it does not attempt to refine nanoparticle structure. The DFA uses a finite set of fixed-structure diffraction patterns to assemble the best possible approximation to an experimental diffraction pattern. If the physical sample differs significantly in structure from the models, for example because of lattice contraction or other relaxation, then the results of the DFA will show this up in the quality of the fit.

DFA analysis is sensitive to the domain structure within the (often) imperfect particles. It remains an open question as to how particle imperfections will contribute to a diffraction pattern: it has been suggested that certain defects can form domains with local atomic arrangements similar to small icosahedra or decahedra, while the particle as a whole may not appear to have this structure [26].

To illustrate DFA, we apply it to a diffraction pattern obtained from a sample of gold particles. These nanoparticles have been synthesized by chemical methods [27] and consist of gold clusters covered by thiol molecules ($C_{12}H_{25}SH$), which are attached to the surface by the sulfur atom. From transmission electron microscopy, the size distribution was estimated to have a mean diameter of 2 nm and a half width of 1 nm [28]. Powder X-ray diffraction studies were performed using 8.040 keV photons. As nanoparticles diffraction peaks are rather large (FWHM ≈ 5 degrees for the (111) peak of 2 nm particles), we used 2 mm detection slits before the scintillation detector. To set up the DFA, complete-shelled models for the three structure types (fcc, ico, dec) were used to calculate diffraction patterns. A total of twelve diffraction patterns were calculated, covering the diameter range between approximately 1 and 3 nm for each structure type (see Table 2-1). In addition, two parameters were assigned for background scattering: one to the substrate contribution, the other a constant offset. The Debye-Waller parameter was kept fixed during optimization, however the rms atomic displacement (see Eq. 2-2) was estimated to be $19 \pm 3 \times 10^{-12}$ m, by repeating the fitting procedure with a range of values for D.

Table 2-1. Numerical values associated with the fit of Fig. 2-5. Note that the proportions of each structure have been rounded to integers, and when estimated values round to zero the associated uncertainties are not reported. The quoted diameter values are obtained from the distribution of inter-atomic distances. The abrevations fcc, ico and dec, refer to cuboctahedral, icosahedral and decahedral model structures, respectively.

Struct.	No. of atoms	Diam. (nm)	Percentage by number	Percentage by weight
fcc	55	1.2	0	0
fcc	147	1.6	0	0
fcc	309	2.2	0	0
fcc	561	2.8	0	0
ico	55	1.1	40 ± 14	29 ± 10
ico	147	1.6	7 ± 7	14 ± 13
ico	309	2.1	0	1 ± 1
ico	561	2.7	0	1 ± 1
dec	39	1.0	30 ± 3	15 ± 2
dec	116	1.5	20 ± 14	31 ± 21
dec	258	2.1	0	0
dec	605	2.9	1 ± 2	8 ± 14

The results of the DFA are presented in Table 2-1 summarizing both the models used and the values estimated for each parameter. In particular, relative proportions are reported both as a number fraction and as a fraction of the total sample weight. This is done because the intensity of diffraction from particles increases in proportion to the number of atoms, and hence larger particles will dominate an observation. The

upper window in Fig. 2-5 shows the experimental data (dotted line) superimposed on the DFA best-fit (solid line), and once again, fcc peak positions are indicated for reference. The lower window shows the difference between the two curves. The almost complete absence of structure in the difference curve indicates that a good fit has been obtained.

The uncertainties reported in Table 2-1 are obtained by collecting statistics from repeated runs. These runs simulate the variability of the measurement process by adding a random component (noise) to the experimental data before each fit starts. The random noise is added here assuming a Poisson process with a rate equal to that of the actual measured intensity. The uncertainty estimates here are obtained from the standard deviations of individual parameters by analyzing values from ten runs. A more complete discussion of this approach to estimating uncertainty in parameters is given by Press et al. [29].

Table 2-1 shows that the sample is composed only of MTP structures with a roughly equal split between icosahedra and decahedra, both types of structure have sizes mainly less than 2 nm. A greater proportion of the icosahedra are the smallest size in the fit, while the decahedral contribution is dominated by the second smallest (1.5 nm) size domains. This is not immediately apparent from a visual inspection of the raw data. Certainly, comparing the profiles of Fig. 2-3 with the experimental diffraction pattern in Fig. 2-5 one would not necessarily expect small icosahedra to be present. Nevertheless, the quality of the fit is definitely made worse if icosahedral structures are excluded. Another remarkable fact is the total absence of fcc nanoparticles. This probably indicates a high proportion of imperfect structures in the sample, which may be showing up as MTPs in the fit.

While the uncertainty associated with the relative proportions of each model is rather high, it must be remembered that these parameters are not independent: at each run the balance of individual structure types is being varied – a little less of one

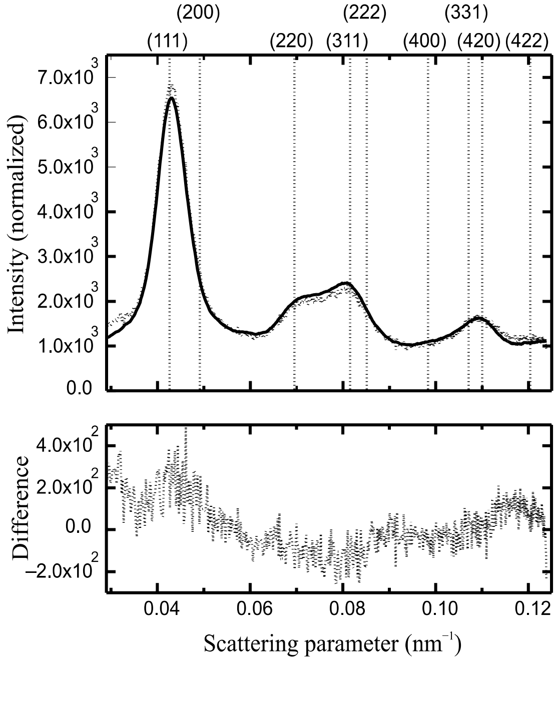

Figure 2-5. Fitting results of the DFA on a sample of 2 nm gold particles. The upper window shows the experimental data (dotted line) superimposed on the fit (solid line). The lower window shows the simple difference between the two curves. Intensity values are arbitrary, but close to the actual count rates that occurred during the experiment.

structure means a little more of another – and this correlation is not captured by our simple calculation of the statistics from several runs. Also, it is important to understand that the parameters estimated by DFA are describing the *shape* of domain size distributions (the uncertainty in the average domain size, for example, is much less). It should not be surprising, therefore, that in the tails of the distributions (where parameter values are small) the relative uncertainty is higher than near the distribution centers. What these results do show is that it is becoming difficult to distinguish clearly between the smallest decahedra and icosahedra. Improving the signal-to-noise ratio, accounting better for systematic contributions (background, and gas scattering), and extending measurements to higher values of scattering parameter, *s*, would all help to aleviate this problem.

We conclude that DFA analysis has clearly identified the presence of MTP structures, and strongly suggests that both icosahedral and decahedral domains are contained in the particles of the sample. Furthermore, given the closeness in size of the decahedral domains to the size observed by TEM, we are confident that single-domain decahedral particles are present in this sample.

2.3.3.1 Technical considerations

The measurement of diffraction patterns from nanoparticle samples differs somewhat from standard powder diffraction work. The intensity of scattering per atom is weak, and the amount of sample material is often limited, so the detection of a low level of diffraction signal can be critical. It is important to reduce unwanted sources of diffraction, such as scattering from gas in the diffraction chamber, and diffraction from the substrate material. Also, because diffraction features are very broad, only low angular resolution is required at the detector and very broad collection angle should be used, increasing the intensity and improving the statistical uncertainty of readings. It must also be remembered that the entire diffraction profile contains structural information about the nanoparticles and therefore that good quality data should be collected for the whole profile, not just in the more intense regions (peaks) of the diffraction pattern.

If good results are to be obtained by DFA, it is important to account for all systematic contributions to the diffraction pattern. DFA tries to recreate an exact match to the experimental data, and is therefore quite sensitive to effects that change the profile shape or components that introduce some structure of their own. It is hard to predict how such systematic errors will show up in the results of the analysis. We therefore recommend that careful measurement of background scattering terms and careful determination of the origin for the diffraction pattern ($s = 0$) be carried out.

An implementation of DFA requires a certain effort in the development of software. A more interactive approach may be valuable in preliminary work, and has sometimes been used in the past [18]. This can usually be done with any general purpose computer mathematical package with graphics. The process is, surprisingly, reasonably quick; indeed, it is an excellent manner in which to convince oneself of the necessity to both incorporate size distributions and include MTP structures in the analysis of metal nanoparticle structure.

An interactive method cannot, however, provide convincing, unbiased results, nor estimate uncertainties in a large number of parameters: some form of automatic optimization is desirable. Unfortunately, the problem to be solved is not easy. Experience has shown that a technique suitable for global optimization is necessary, as one can

easily be trapped in local minima. In the work presented here, a simple form of the simulated annealing algorithm is used and found to be quick and reliable [22, 29], the code used for this work is written in C and it runs on a desktop PC.

2.4 Extended X-ray absorption spectroscopy

2.4.1 X-ray absorption spectroscopy

The technique of X-ray Absorption Spectroscopy (XAS) explores variations in the absorption coefficient of matter with photon energy. When a monochromatic X-ray beam passes through a material, its intensity is reduced by various interaction processes (scattering, absorption, etc.). For hard X-rays (more than 1000 eV), the photoelectric effect dominates, in which a core atomic electron is ejected by photon absorption. The absorption coefficient, μ, can be defined as [2, 30]:

$$I = I_0 e^{-\mu t} \tag{2-3}$$

where I is the transmitted intensity, t is the material thickness traversed and I_0 is the incident beam intensity. The coefficient μ depends both on material properties and photon energy (E).

In general, as photon energy increases, the absorption coefficient decreases gradually until critical energies are attained, whereupon it changes abruptly. These discontinuities, known as absorption edges, occur when the photon energy corresponds to a threshold (E_0) for core electron excitation. The energy of the absorption edge is specific to each chemical element, since it corresponds to the binding energy of the photoelectron.

When this absorption process occurs in condensed matter, the ejected photoelectron interacts with atoms in the immediate neighborhood, resulting in a modulation of the absorption coefficient beyond the edge. These modulations can easily be identified in an experimental spectrum, for example that shown in Fig. 2-6a. Based on the energy of the ejected electron ($E - E_0$), it is possible to roughly divide the absorption spectrum in two regions, according to different interaction regimes with the surrounding atoms:

- XANES (X-ray Absorption Near Edge Structure): ≈ 0–40 eV above E_0, where multiple scattering events take place, yielding information about symmetries and chemical state.
- EXAFS (Extended X-ray Absorption Fine Structure): ≈ 40–1000 eV, where single scattering events dominate, providing structural information, such as coordination numbers and inter-atomic distances.

To understand and model the XANES spectral region usually requires heavy, and complicated, multiple scattering calculations. On the other hand, EXAFS oscillations, dominated by single electron scattering process, can be handled in a simpler mathematical treatment. The availability of reliable and simplified data processing has transformed EXAFS into a widely used structural characterization technique, and also explains why most XAS studies have been done in this spectral region. In particular, EXAFS has been used as an alternative (and sometimes a complement) to XRD, since it probes the local environment of the excited atom. Indeed, EXAFS can be

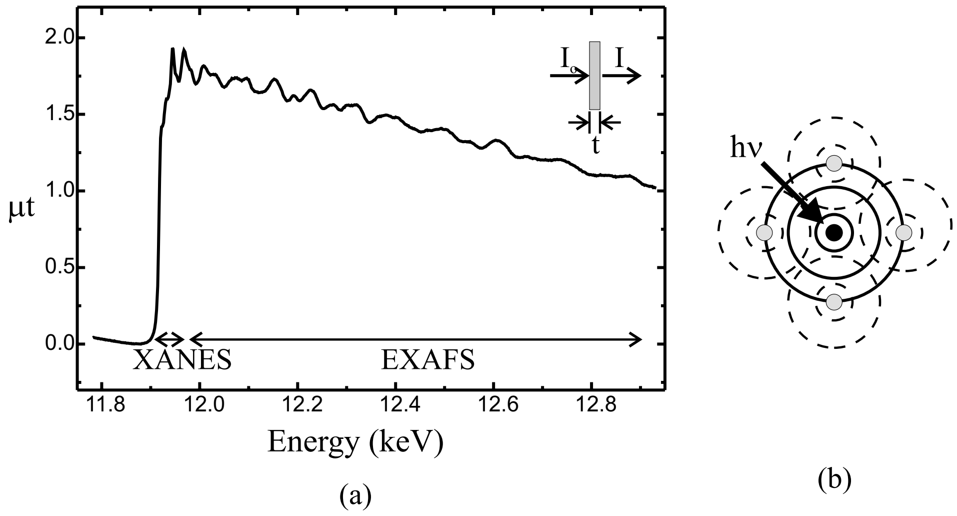

Figure 2-6. a) X-ray absorption spectrum of Au-L_3 edge of a gold film. Note the modulation of the absorption coefficient above the edge. b) Pictorial representation of the interference process between ejected (solid line) and backscattered (dashed line) photoelectron waves that gives rise to the EXAFS oscillations. See text for explanations.

seen as a low-energy electron diffraction process, where the photelectron comes from an energy-selected atomic element. Concerning nanostructured materials, many authors have tackled the problem of determining the inter-atomic distances by EXAFS [31–33]. This measurement is rather difficult to obtain in these systems by other means, due to the intrinsic lack of long-range order in small particles. In the following sections we describe the basic process and the special features of EXAFS experiments on nanoparticles, and illustrate these with a particular example.

2.4.2 EXAFS

In order to understand the physical origin of EXAFS oscillations, we must first remember that the probability for a core electron to absorb an X-ray photon depends on both the initial and final states. Above the edge, the final state can be described by an outgoing spherical wave, originating at the absorbing atom. This wave may be scattered by neighboring atoms, resulting in an interference pattern (see Fig. 2-6b). The final state will depend on both (outgoing and scattered) wave phases, which in turn will depend on the electron wavevector (k), or equivalently on the ejection energy. Hence, the exact position of neighboring atoms can affect the probability of exciting a core electron and gives rise to the oscillatory behavior of the absorption coefficient as a function of photoelectron energy.

Mathematically, the interference term arising from scattering by a single neighbor can be expressed as $A(k)\sin[2kr+\phi(k)]$, where k is the modulus of the wavevector, r is the distance between absorbing and neighbor atoms, and $\phi(k)$ represents the total photoelectron phase-shift and depends on both photoabsorber and scattering atoms. $A(k)$ is the backscattering amplitude and is mainly a characteristic of the scatterer

atom. The total EXAFS signal consists of the superposition of individual pair-wise contributions from all neighboring atoms; these can be grouped into coordination shells composed of atoms found at similar distances from the absorbing atom.

The EXAFS oscillations, $\chi(k)$, are given by [30]:

$$\chi(k)=\sum_{j} S_0^2(k)\frac{N_j}{kr_j^2}\,e^{-2\sigma_j^2k^2}\,e^{-2\frac{r_j}{\lambda_j(k)}}A_j(k)\sin\left[2kr_j+\phi_j(k)\right] \tag{2-4}$$

where

$$k=\sqrt{\frac{2m}{\hbar^2}\left(E-E_0\right)} \tag{2-5}$$

k	=	photoelectron wavevector modulus;
j	=	coordination shell index;
r	=	distance between the absorbing atom and a neighbor;
N	=	number of identical atoms in the same coordination shell;
$A(k)$	=	backscattering amplitude;
σ	=	total Debye-Waller factor (including static and dynamic contributions);
$\phi(k)$	=	total phase shift;
$\lambda(k)$	=	photoelectron mean free path;
$S_0^2(k)$	=	amplitude reduction factor due to many-body effects;
E	=	photon energy;
m	=	electron mass;
E_0	=	threshold energy.

The structural parameters involved in the EXAFS equation are the coordination number (N), the inter-atomic distance (r), and the Debye-Waller factor (σ). The latter includes two contributions: dynamic, arising from atomic vibration, and static, which is caused by structural disorder in a given coordination shell. This expression also includes atomic parameters such as $\lambda(k)$, $A(k)$, $\phi(k)$, $S_0^2(k)$. The EXAFS equation supposes that a harmonic approximation applies to atomic vibrations and that the pair-distribution function for inter-atomic distances, $P(r)$, is assumed to be Gaussian. The term $\exp(-2r/\lambda(k))$ accounts for the finite photoelectron lifetime and represents the probability for the photoelectron to travel to, and from, the backscatterer without additional scattering and before the core hole is filled.

Since it has been assumed that $\chi(k)$ can be represented by a linear combination of sine waves from each coordination shell, it is possible, in principle, to separate each contribution by applying a Fourier transform. By extracting and analyzing the EXAFS signal we can obtain estimates for the structural parameters: N, r and σ for each shell, however, this requires, prior knowledge of the atomic parameters: $\lambda(k)$, $A(k)$, $\phi(k)$, $S_0^2(k)$. To obtain the required set of atomic parameters, two approaches are possible: they can be either calculated theoretically, or determined experimentally by using a standard reference compound; in principle both methods seem to have the same limits of accuracy [2].

2.4.2.1 Special features of EXAFS in nanoparticle systems

The wide use of EXAFS in materials research has led to the development of robust procedures for the use of this technique for bulk systems. As mentioned in Section 2.4.2, the origin of EXAFS oscillations lies in the interaction of the ejected photoelectron with the neighboring atoms. Since only the local environment of the excited atom is probed, both experimental methods and data analysis procedures can be applied to nanostructured systems. However, as might be expected, the structural parameters (N, r, σ) one obtains depend on the characteristic size of the system.

Intuitively, the very small size of particles will lead to a decrease in the mean coordination number, and an absence of higher order coordination shells. Deviation in the measured value of N, from the bulk, may be used as a rough estimate of the mean particle diameter [34, 35], however other factors may also influence this measurement, such as size-induced modification of the particle structure.

One of the main results that can be obtained by EXAFS is a precise determination of inter-atomic distance (in practice, to better than 0.002 nm). EXAFS is well suited to this measurement because it does not require long-range order and can be used to directly determine changes to the nearest-neighbor distance in disordered or finite systems.

EXAFS can also provide valuable information on nanoparticle structure. Although structure cannot be fully determined, it has been proposed that through the analysis of the first and second coordination shell distances, and in particular the ratio r_I/r_{II} (I – first and II – second shells), it should be possible to distinguish between MTPs and bulk-like structures in metals [36]. In other systems, such as semiconductors, a careful comparison among the parameters has been used to differentiate hexagonal from cubic structures [35].

Experimental measurements of the Debye-Waller factor can be used to obtain further structural information. Firstly, the stiffening or softening of the chemical bonds due to the modification of the surface atomic potential can be observed, because of modifications in the atomic vibrations [32, 37]. Secondly, we expect, based on surface studies, that the large surface-to-volume ratio will result in a higher structural disorder in nanosystems. It is well known that the lack of translational symmetry in surfaces leads to atomic rearrangement, changing the bond distribution. In nanostructured materials, this effect will tend to grow as the particle diameter decreases and will enhance the average static contribution to the Debye-Waller factor. Careful analysis of EXAFS data at different temperatures can be used to separate the dynamic and static contributions to the Debye-Waller factor and hence measure the structural disorder and deduce vibrational properties (such as the Debye temperature) [35, 36, 38].

In summary, structural information can be obtained by the EXAFS through the parameters N, r and σ. When dealing with nanosystems, these parameters are dependent on the size of the system. One of the key measurements that EXAFS can perform is an accurate estimate of nearest-neighbor distance. The technique can also provide indirect information on: particle dimensions; vibrational properties; and structural defects.

2.4.3 Data analysis applied to nanoparticles

We now present an example of an EXAFS study that shows the main aspects of interest in nanomaterials research. We have selected a system where it is possible to observe most of the advantages and some specific difficulties of the technique. The experimental sample consists of the same thiol-capped 2 nm gold nanoparticles described in Section 2.3.3. The experiment set out to investigate the possibility of changes in inter-atomic distances, since a contraction is expected for metal clusters due to surface stress [39]. Measurements were performed on the Au-L_3 edge (11.919 keV), at low temperature (8 K), in transmission mode and with an energy resolution of 1.8 eV. Detection used two gas ionization chambers.

From a qualitative point of view, we can expect to observe certain differences between an absorption spectrum from a bulk sample and one from a sample of thiol-capped gold nanoparticles (Fig. 2-7). Firstly, a stronger attenuation in the EXAFS oscillations is expected. The reduction of the mean coordination number, and the absence of higher order coordination shells, results in a homogeneous attenuation of the EXAFS oscillation amplitude. In addition, higher structural disorder and the surface metal-ligand bonds contribute to the damping of the EXAFS oscillations at high k-values. It must be remembered that due to the passivation by thiol molecules, surface gold atoms are coordinated with both sulfur and gold. The metal-ligand damping effect can be understood because the EXAFS interference term is multiplied by the backscattering amplitude factor, $A(k)$, which strongly depends on the atomic number of the scatterer atom. For heavy atoms, $A(k)$ has a significant contribution over the whole k-range of interest, whereas for light elements, such as sulfur, it decreases monotonically at high k-values.

Secondly, the characteristic frequency of the EXAFS oscillations may be expected to change if the nearest-neighbor inter-atomic distance does so. Both, the existence of Au-Au inter-atomic distance contraction and the presence of the Au-S bond (shorter

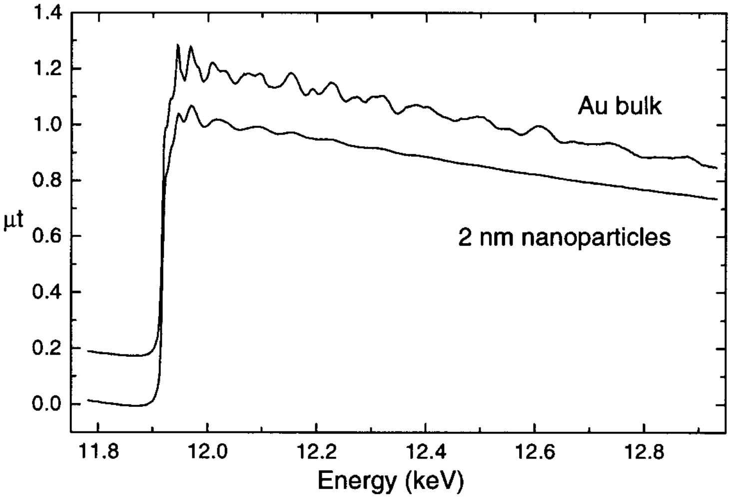

Figure 2-7. Comparison of the absorption spectrum of 2 nm thiol-capped gold nanoparticles and bulk gold. The attenuation and damping of the nanoparticle EXAFS oscillations can be clearly observed. Measurements were performed at low temperature (8 K).

than the Au-Au one) should decrease the oscillation frequency in the k-space. Although it is not easy to see this effect directly in the EXAFS spectrum, it becomes visible when the signal from the first coordination shell is isolated.

In the remainder of this section, we present an example of practical EXAFS data analysis in some detail, the individual steps have been assigned to subsections [2, 30, 40].

2.4.3.1 Extraction of EXAFS signal

The absorption spectrum is composed of EXAFS oscillations superposed on a smooth background, which comes from the other absorption edges and from the other elements in the sample. In terms of the measured signal, $\mu(E)$, the EXAFS oscillations $\chi(E)$ are defined as:

$$\chi(E) = \frac{\mu(E) - \mu_0(E)}{\Delta\mu(E)} \tag{2-6}$$

where $\mu(E)$ is the absorption coefficient associated with a particular edge (Au-L_3, in this case) and $\mu_0(E)$ is the absorption coefficient of an isolated gold atom;$\Delta\mu(E)$ is the change in the atomic absorption across the edge, and provides normalization. Consequently, the first step in the analysis involves (see Fig. 2-8):

a) subtraction of the pre-edge background: obtained by a least squares fit with a straight line or Victoree-like function ($a\lambda_p^3 - b\lambda_p^4$, λ_p= X-ray wavelength);
b) subtraction of the atomic absorption coefficient (μ_0): estimated by a polynomial fit in the EXAFS region, by cubic-splines or other interpolation functions;
c) normalization: difference between μ_0 and the extrapolation of the pre-edge region. This extrapolation is usually performed by fitting a standard analytical function, it requires an estimate of the threshold value, E_0. The choice of this parameter is arbitrary, as it is refined during the fitting procedure. Usually it is chosen as a characteristic point in the absorption curve, for example, the first inflection point.

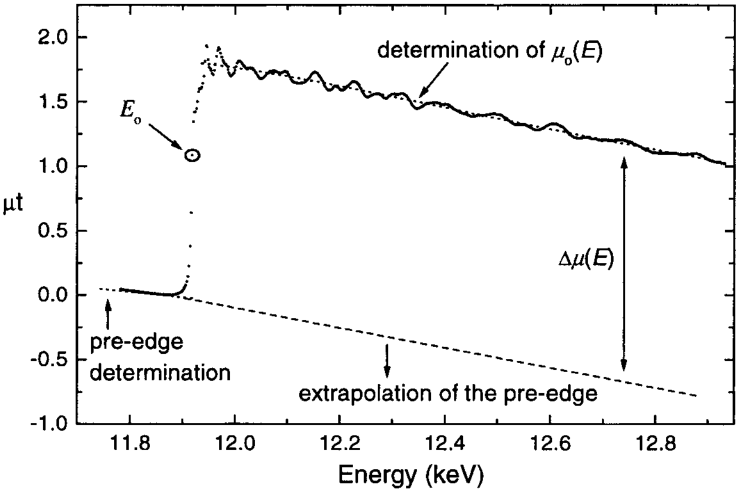

Figure 2-8. Representation of the EXAFS signal extraction from the X-ray absorption spectrum ($\mu(k)$ = absorption coefficient; $\mu_0(k)$ = atomic absorption coefficient, $\Delta\mu(k)$ = normalization). See text for explanations.

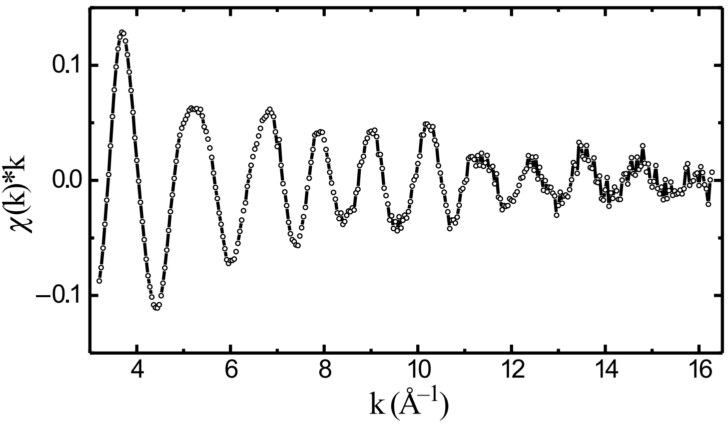

Figure 2-9. EXAFS oscillations of 2 nm gold nanoparticles.

Because the absorption spectrum is measured as a function of energy, but the photoelectron interference is better described in terms of *k*, a change of variable is made to transform from *E*- to *k*-space using Eq. 2-5.

A check on the quality with which the EXAFS signal has been extracted can be made by verifying that the oscillations are symmetrically distributed around zero. Another point to check is that the function representing the atomic absorption coefficient does not match the EXAFS oscillations, this can be seen by taking its derivative. Finally, we obtain the EXAFS oscillations shown in Fig. 2-9.

2.4.3.2 Fourier Transform

To separate the EXAFS contributions from individual coordination shells, we can Fourier Transform (FT) $\chi(k)$ into *r*-space. The FT of the EXAFS oscillations corresponds to a pseudo-radial function, where peak positions, *R*, are related to inter-atomic distances (although they also include phase-shift effects), and the area under peaks

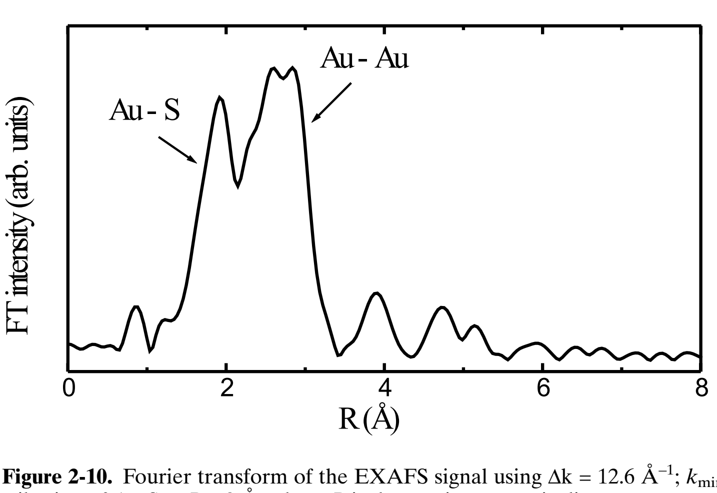

Figure 2-10. Fourier transform of the EXAFS signal using Δk = 12.6 Å^{-1}; k_{min} = 3.4 Å^{-1}. Note the contribution of Au-S at $R \approx 2$ Å, where *R* is the raw inter-atomic distance, not corrected by phase shift.

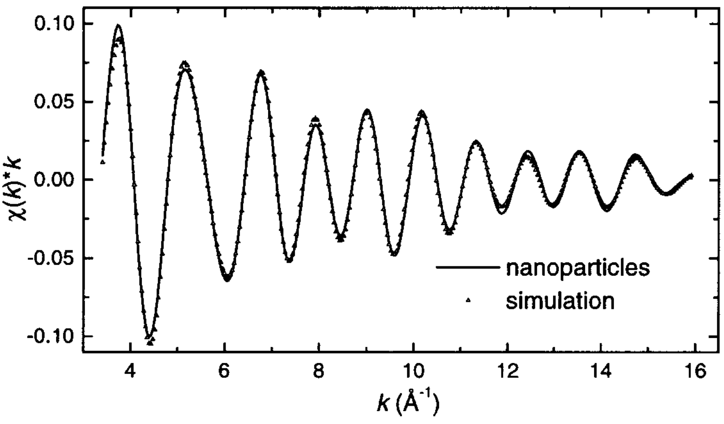

Figure 2-11. Fourier filtering of the nanoparticles first coordination shell and corresponding simulation, which includes both Au-Au and Au-S contributions ($\Delta R = 1.85$ Å, $R_{min} = 1.55$ Å).

can be associated with the number and type of backscatterers. It is usual to truncate the FT at a lower limit ~ $k_{min} = 3$ Å^{-1}, in order to avoid the contamination by multiple scattering effects (XANES region). Figure 2-10 shows the resulting FT curve; in this particular case, only the first Au-Au coordination shell can be clearly identified due to the small size of particles (2 nm).

2.4.3.3 Isolation of a specific coordination shell

A selected r-space range can be transformed again, from r-space to k-space. This has been done in Fig. 2-11, where the k-space signal now refers to what is the first coordination shell. In this particular case, the difference between Au-Au and Au-S inter-atomic distances is too close to separate out the two contributions by FT, and as a result, it will be necessary to treat the two shells together.

2.4.3.4 Fitting procedure

The last step consists of a procedure to estimate the structural parameters (N, r, σ) by least-squares. Values for the atomic parameters: $\lambda(k)$, $A(k)$, $\phi(k)$ and $S_0^2(k)$ must be provided. Because there are two contributions (Au-Au, Au-S) to be modeled, two sets of atomic parameters are necessary. We have used a thin gold film to derive the Au-Au shell atomic parameters ($N = 12$, $r = 2.865$ Å, $\sigma = 0$), whereas Au-S parameters were obtained theoretically (McKale tables [41], $r_{Au\text{-}S} = 2.32$ Å). In the first case, an identical EXAFS procedure is applied to experimental data of the standard compound however now, in the fit, the known parameters are the structural ones. The resulting parameters are presented in Table 2-2; uncertainty estimates were obtained by doubling the residual at the minimum [42].

Table 2-2. Fit results of EXAFS spectrum for 2.0 nm nanoparticles. Bulk gold structural parameters are: $r_{Au\text{-}Au}$ = 2.865 Å and $N_{Au\text{-}Au}$ = 12; $\sigma_{Au\text{-}Au}$ is assumed to be equal zero. ΔE_0 takes into account the threshold energy refinement.

	Au-Au	Au-S
r [Å]	2.843 ± 0.007	2.34 ± 0.02
N	7.2 ± 0.8	0.8 ± 0.2
σ [Å]	0.078 ± 0.004	0.06 ±0.02
ΔE_0 [eV]	0.0 ± 0.6	10 ± 2

In this example, the EXAFS analysis reveals two important effects: the existence of a slight Au-Au inter-atomic distance contraction of about 0.8% ($r_{Au\text{-}Au}$ = 2.843 Å) and a short Au-S distance ($r_{Au\text{-}S}$ = 2.34 Å), comparable to other gold-sulfur systems [43]. These results indicate that the expected contraction, verified in gold particles immersed in a weakly interacting matrix (~ 1.4% [37]), may be partially compensated by the bonding with thiol molecules. It has already been established that the presence of sulfur on (100) surfaces of fcc metals induces an expansion between surface planes [44]. As for the coordination number (N), the estimated value (7.2) is smaller than the expected one (≈ 9.3) for an ideal 2 nm fcc particle formed by ≈ 200 atoms. Several experimental factors, such as thickness variations in the sample, may affect the determination of N, and account for this discrepancy. However, it is important to realize that the error in N is usually quite large (10–20%) and its relationship to other sample parameters (such as nanoparticle size) needs to be handled with care.

2.4.4 Troublesome points in the data treatment

In the example above, we have chosen to use the conventional method of analysis, by Fourier transforms, because of its mathematical simplicity, which makes it easier to understand the processes involved. Although we have only analyzed the first coordination shell, it is also possible to treat higher order coordination shells in systems where these can be easily identified, such as bigger particles or when the Debye-Waller factor is small enough. However, the analysis of higher-order shells is usually more complex, because of possible multiple scattering processes (ex. focusing); also, additional care must be taken to account for possible mean free path effects [2].

The formulation of the EXAFS spectrum presented in Section 2.4.2 is valid in the small structural disorder limit, or the harmonic approximation, where the Debye-Waller factor is given by $\exp(-2\sigma^2k^2)$. However, this expression is not valid for systems with a high degree of disorder or high-temperature experiments, where anharmonic contributions are no longer negligible. In fact, for nanosystems, due to the intrinsic asymmetry of the surface atomic potential, the temperature effect can be much more pronounced than in bulk materials. In many cases, it is necessary to use a more general equation, where the probability of finding the jth species in the range r_j to r_j+dr_j is represented by the distribution function $P(r)$, which may be asymmetric. However, in such cases the data treatment becomes more complex due to the inclusion of additional free parameters in the fitting procedure [2, 45, 46]. It is worth pointing out that the existence of an asymmetric distribution function, if not properly taken into

account, leads to serious errors in calculated structural parameters. In general, the main consequences will be a reduction in the coordination number and a fictitious inter-atomic distance contraction [46].

One alternative to solve the more general EXAFS problem is to use the method of cumulants, which involves the expansion of a function associated with $P(r)$ in a moment-series; deviations from a Gaussian distribution are represented by the higher-order terms of the expansion [2]. Unfortunately, the inclusion of these extra terms may lead to trouble in the data analysis, such as strong correlations among the parameters [37]. In addition, for the system where two types of atom constitute the first shell, as studied here, this method has to be applied with care.

Another approach is to analyze the absorption spectrum directly, instead of just the EXAFS oscillations. In this method, the background and all the coordination shells are fitted simultaneously. This provides a more complete description of the absorption phenomenon but requires more complex theoretical calculations. In particular, it is necessary to use a cluster model that is close to the actual structure. This method has been implemented in a software package called GNXAS, which was initially developed for disordered structures and it has also been applied to nanosystems [45, 47]. The EXAFS technique, as presented above, has been used widely in materials research because of its relatively straightforward data treatment.

The use of more sophisticated packages, although essential in particular cases, make it more difficult to ascribe physical meaning to the additional parameters included in an analysis. In general, in a first attempt, one should try to analyze and evaluate possible sources of asymmetry in the distribution function. In particular, performing measurements at low temperature avoids problems with anharmonic terms [48]. In our example, this was clearly demonstrated: room temperature experiments suggested an inter-atomic distance (2.82 ± 0.01 Å) shorter than the one measured at 8 K (2.843 ± 0.007 Å). Another source of problems is high structural disorder, it is prudent to use complementary techniques, such as XRD and HRTEM to evaluate the importance of this in a particular study.

As in all experimental data analysis, results from the EXAFS fits should be qualified with uncertainty estimates for each parameter, as well as the correlations between them. There are some well-established and specific guidelines for EXAFS analysis that must be considered in the data treatment [42]. In particular, it is necessary to take care about the correlation between N and σ (related to the oscillation amplitude) and r and E_0 (related to the oscillation frequency).

In this section, we have attempted to give a basic introduction to EXAFS as well as the treatment of data when applied to nanosystems. There are, however, new analytical procedures that have been implemented and it was not intended to cover all possible methodologies here. Readers will find ample details in the specialized literature, where there are many other examples related to nanostructured materials [31–38, 47, 48].

2.5 Conclusions

X-ray methods of characterization represent a powerful approach to the study of nanophase materials. The advantage of these techniques is to provide meaningful ensemble-averaged information about both medium range, and local, atomic structure

in nanosystems. By characterizing the sample as a whole, they are an essential complement to other high-resolution methods, which provide rather detailed information on only a few particles.

In particular, we have discussed the application of two of the most popular X-ray based structural probes: diffraction and EXAFS. We have shown that it is possible to acquire detailed information about the structure of very small gold particles (2 nm in diameter), identifying and characterizing non-crystallographic atomic arrangements in the sample, as well as making a precise measurement of the nearest-neighbor distance in the clusters.

We do not wish the reader to conclude that the application of EXAFS and XRD are limited by the parameters of our two examples. Concerning EXAFS, we have only discussed the details of inter-atomic distance determination in small metal clusters. However, in favorable cases, a more extensive study, could yield reliable estimates of other parameters, such as structure [32, 35, 36], mean particle diameter [34] and structural disorder [32, 35, 36]. It is important to note that our examples dealt with gold, where the very interesting occurrence of MTP structures greatly complicates the analysis. MTPs are multi-domain structures in which the constituent units represent slight distortions of the fcc lattice. Both EXAFS and XRD methods could be expected to perform much better in systems of nanoparticles where the structural variety of clusters is better differentiated, such as semiconductors (e.g.: the transition between wurzite and zinblende structures [35]).

In dealing with nanoparticle samples, it must be stressed that results of high-quality can only be acquired if very careful attention is paid to both the measurement of raw data and its subsequent processing and interpretation. Synchrotron radiation sources are virtually a necessity to obtain measurements of sufficient quality; such data can then be subjected to detailed analysis, and valuable information derived. Modern optics and the existence of special devices, such as wigglers allow measurements of small quantities of sample material at good signal levels.

For EXAFS in particular, the association of more intense sources with an optimized setup for low temperature measurements would allow inclusion of the additional structural information in the high k-range (> 16 Å^{-1}); thereby improving the precision in parameter estimates through the use of the Fourier transform in EXAFS analysis.

For diffraction, it would be desirable to include a greater range of scattering parameter in future studies. The range should be extended to collect data both at larger values of s, and in the low-angle region. The latter provides direct information about particle size and shape, complementing the results of DFA. This would allow a more definitive statement to be made about the numbers of defective structures in the sample, by allowing comparison of particle size information (from small-angles) with domain size information (from wide-angles). Experiments performed with higher energy photons would permit measurements to be extended out to higher values of s. Such measurements would capture more structural information and thus improve the selectivity of the DFA method. If the range of s can be made sufficiently great, then it is also possible to use Fourier techniques to invert the diffraction pattern, thereby obtaining the distribution of inter-atomic distances in the clusters. This information could be compared directly with estimates of nearest-neighbor distance determined by EXAFS.

We hope that the examples presented will have shown the reader the possibilities offered by X-ray techniques in probing nanosystems, and that the information provided may assist in the correct application of the methods described.

Acknowledgement

The authors acknowledge the invaluable help of the LNLS staff, and thank H. Tolentino for stimulating discussions. DZ and DU are indebted to FAPESP (Contracts 96/12550–8, 97/04236-4) and CNPq for funding. BDH gratefully acknowledges financial support for travel under the NZ/BRAP STC Agreement Programme (99-BRAP-11-HALL).

References

[1] B. D. Cullity, *Elements of X-Ray Diffraction*, Reading, Addison-Wesley Publishing Co. Inc., **1978**.
[2] D. C. Koningsberger and R. Prins, *X-Ray Absorption: Principles, Applications, Techniques of EXAFS, SEXAFS and XANES*, New York, John Wiley & Sons, **1988**, Chapters 1, 6 and 9.
[3] A. Guinier and G. Fournet, *Small-Angle Scattering of X-Rays*, New York, Wiley, **1955**.
[4] O. Glatter and O. Kratky, *Small-Angle X-Ray Scattering*, London, Academic Press, **1982**.
[5] G. Margaritondo, *Introduction to Synchrotron Radiation*, Oxford, Oxford University Press, **1988**, Chapter 1.
[6] A. Guinier, *X-ray diffraction in crystals, imperfect crystals, and amorphous bodies*, New York, Dover, **1994**.
[7] A. J. C. Wilson (Ed.), *International Tables for Crystallography*, Dordrecht, Netherlands, Kluwer Academic, **1992**.
[8] C. W. B. Grigson and E. Barton, *Brit. J. Appl. Phys.* **1967**, *18*, 175.
[9] J. B. Cohen, *Ultramicroscopy* **1990**, *34*, 41.
[10] S. Ino, *J. Phys. Soc. Japan* **1966**, *21*, 346; S. Ino and D. Ogawa, *J. Phys. Soc. Japan* **1967**, *22*, 1365; J. G. Allpress and J. V. Sanders, *Surf. Sci.* **1967**, *7*, 1.
[11] L. D. Marks, *Rep. Prog. Phys.* **1994**, *57*, 603.
[12] C. L. Briant and J. J. Burton, *Surf. Sci.* **1975**, *51*, 345.
[13] A. L. Mackay, *Acta Cryst.* **1962**, *15*, 916.
[14] S. Ino, *J. Phys. Soc. Jpn.* **1969**, *26*, 1559; S. Ino, *J. Phys. Soc. Jpn.* **1969**, *27*, 941.
[15] B. G. Bagley, *Nature* **1965**, *208*, 674.
[16] C. Y. Yang, *J. Cryst. Growth* **1979**, *47*, 274.
[17] J. W. Lee and G. D. Stein, *J. Phys. Chem.* **1987**, *91*, 2450.
[18] D. Reinhard, B. D. Hall, D. Ugarte, and R. Monot, *Phys. Rev. B* **1997**, *55*, 7868.
[19] B. D. Hall, M. Flüeli, R. Monot and J.-P. Borel, *Z. Phys. D* **1989**, *12*, 97.
[20] B. D. Hall, M. Flüeli, R. Monot, and J. -P. Borel, *Phys. Rev. B* **1991**, *43*, 3906.
[21] D. Reinhard, B. D. Hall, P. Berthoud, S. Valkealahti and R. Monot, *Phys. Rev. Lett.* **1997**, *79*, 1459.
[22] D. Reinhard, B. D. Hall, P. Berthoud, S. Valkealahti and R. Monot, *Phys. Rev. B* **1998**, *58*, 4917.
[23] V. Gnutzmann and W. Vogel, *J. Phys. Chem.* **1990**, *94*, 4991.
[24] W. Vogel, B. Rosner and B. Tesche, *J. Phys. Chem.* **1993**, *97*, 11611; W. Vogel, D. A. H. Cunningham, K. Tanaka and M. Haruta, *Catal. Lett.* **1996**, *40*, 175.
[25] B. D. Hall, *J. Appl. Phys., submitted.*
[26] B. W. van de Waal, *Phys. Rev. Lett.* **1996**, *76*, 1083.
[27] M. Brust, M. Walker, D. Bethell, D. J. Schiffrin and R. Whyman., *J. Chem. Soc., Chem. Commun.* **1994**, 801.
[28] D. Zanchet et al., *J. Phys. Chem. B., submitted.*
[29] W. H. Press, S. A. Teukolsky, W. T. Vetterling, and B. P. Flannery, *Numerical Recipes in C: The Art of Scientific Computing*, Cambridge, Cambridge UK, **1992**.
[30] B. K. Teo, *EXAFS: Basic Principles and Data Analysis*, Heidelberg, Springer-Verlag, **1986**.
[31] P. A. Montano, G. K. Shenoy, E. E. Alp, W. Schulze and J. Urban, *Phys. Rev. Lett.* **1986**, *56*, 2076.
[32] M. A. Marcus, M. P. Andrews, J. Zegenhagen, A. S. Bommannavar and P. Montano, *Phys. Rev. B* **1990**, *42*, 3312.
[33] A. Balerna et al., *Phys. Rev. B* **1985**, *31*, 5058.
[34] M. Borovisky, *J. Phys. IV* **1997**, *7*, C2-259.
[35] J. Rockenberger et al., *J. Phys. Chem.* **1997**, *101*, 2691.
[36] A. Balerna et al., *Surf. Sci.* **1985**, *156*, 206.
[37] A. Pinto et al., *Phys. Rev. B* **1995**, *51*, 5315.
[38] A. Balerna and S. Mobilio, *Phys. Rev. B* **1986**, *34*, 2293.

[39] C. W. Mays, J. S. Vermaak and D. Kuhlmann-Wilsorf, *Surf. Sci.* **1968**, *12*, 134.
[40] We have used the software packaged "EXAFS pour le MAC" developed by A Michailowitz, Ph.D. Thesis, Université Paris Val de Marne 1990.
[41] A. G. McKale, *J. Amer. Chem. Soc.* **1988**, *110*, 3763.
[42] F. W. Lytle, D. E. Sayers and E. A. Stern, *Phys. B* **1989**, *158*, 701.
[43] R. C. Elder et al., *ACS Sym. Ser.* **1983**, *209*.
[44] F. Sette, T. Hashizume, F. Comin, A. A. MacDowell and P. H. Citrin, *Phys. Rev. Lett.* **1988**, *61*, 1384.
[45] A. Filipponi, A. Di Cicco and C. R. Natoli, *Phys. Rev. B* **1995**, *52*, 15122; A. Filipponi and A. Di Cicco, *Phys. Rev. B* **1995**, *52*, 15135; A. Di Cicco, *Phys. B* **1995**, *208&209*, 125.
[46] P. Eisenberg and G. S. Brown, *Solid State Commun.* **1979**, *29*, 481.
[47] R. E. Benfield et al., *Phys. B* **1995**, *208&209*, 671.
[48] L.B. Hansen, P. Stoltze, J. K. Noskov, B. S. Clausen, W. Niemann, *Phys. Rev. Lett.* **1990**, *64*, 3155.

Characterization of Nanophase Materials. Edited by Zhong Lin Wang
Copyright © 2000 Wiley-VCH Verlag GmbH
ISBNs: 3-527-29837-1 (Hardcover); 3-527-2960009-4 (Electronic)

3 Transmission Electron Microscopy and Spectroscopy of Nanoparticles

Zhong Lin Wang

One of the typical characters of nanophase materials is the small particle sizes. Although some structural features can be revealed by x-ray and neutron diffraction, direct imaging of nanoparticles is only possible using transmission electron microscopy (TEM) and scanning probe microscopy. TEM is unique because it can provide a real space image on the atom distribution in the nanocrystal and on its surface [1]. Today's TEM is a versatile tool that provides not only atomic-resolution lattice images, but also chemical information at a spatial resolution of 1 nm or better, allowing direct identification the chemistry of a single nanocrystal. With a finely focused electron probe, the structural characteristics of a single nanoparticle can be fully characterized. To reveal the capabilities of a modern TEM, this chapter is designed to illustrate the fundamentals of TEM and its applications in characterization of nanophase materials. The fundamentals and applications of scanning transmission electron microscopy (STEM) will be given in Chapter 4.

3.1 A transmission electron microscope

A modern TEM can be schematically shown in Figure 3-1, which is composed of a illumination system, a specimen stage, an objective lens system, the magnification system, the data recording system(s), and the chemical analysis system. The electron gun is the heart of the illumination system, which typically uses LaB_6 thermionic emission source or a field emission source. The LaB_6 gun gives a high illumination current but the current density and the beam coherence are not as high as those of a field emission source. Field emission source is unique for performing high coherence lattice imaging, electron holography and high spatial resolution microanalysis. The illumination system also includes the condenser lenses that are vitally important for forming a fine electron probe. Specimen stage is a key for carrying out structure analysis, because it can be used to perform in-situ observations of phenomena induced by annealing, electric field, or mechanical stress, giving the possibility to characterize the physical properties of individual nanostructures. The objective lens is the heart of an TEM, which determines the limit of image resolution. The magnification system consists of intermediate lenses and projection lenses, and it gives a magnification up to 1.5 million. The data recording system tends to be digital with the use of a charge coupled device (CCD), allowing quantitative data processing and quantification. Finally, the chemical analysis system is the energy dispersive x-ray spectroscopy (EDS) and electron energy-loss spectroscopy (EELS), both can be used complimentary to quantify the chemical composition of the specimen. EELS can also provide information about the electronic structure of the specimen.

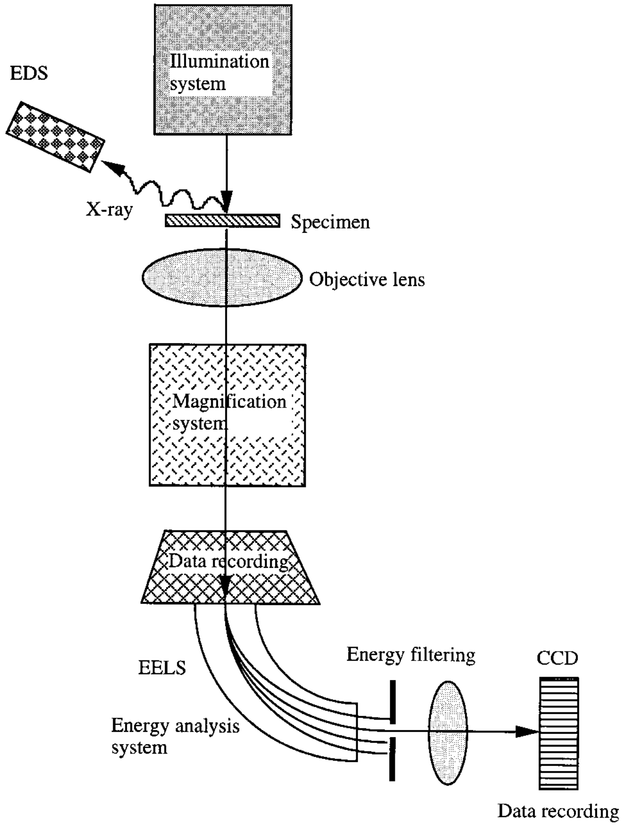

Figure 3-1. Schematic structure of a transmission electron microscope.

3.2 High-resolution TEM lattice imaging

3.2.1 Image formation

As a start, we first illustrate the image formation process in an TEM [2]. For easy illustration, an TEM is simplified into a single lens microscope, as given in Figure 3-2, in which only a single objective lens is considered for imaging and the intermediate lenses and projection lenses are omitted. This is because the resolution of the TEM is mainly determined by the objective lens. The entrance surface of a thin foil specimen is illuminated by a parallel or nearly parallel electron beam. The electron beam is diffracted by the lattices of the crystal, forming the diffracted beams which are propagating along different directions. The electron-specimen interaction results in phase and amplitude changes in the electron wave that are determined by quantum mechanical diffraction theory. For a thin specimen and high-energy electrons, the transmitted wave function $\Psi(x, y)$ at the exit face of the specimen can be assumed to be composed of a forward-scattered wave.

The non-near-axis propagation through the objective lens is the main source of non-linear information transfer in TEM. The diffracted beams will be focused in the back-focal plane, where an objective aperture could be applied. An ideal thin lens brings the parallel transmitted waves to a focus on the axis in the back focal plane.

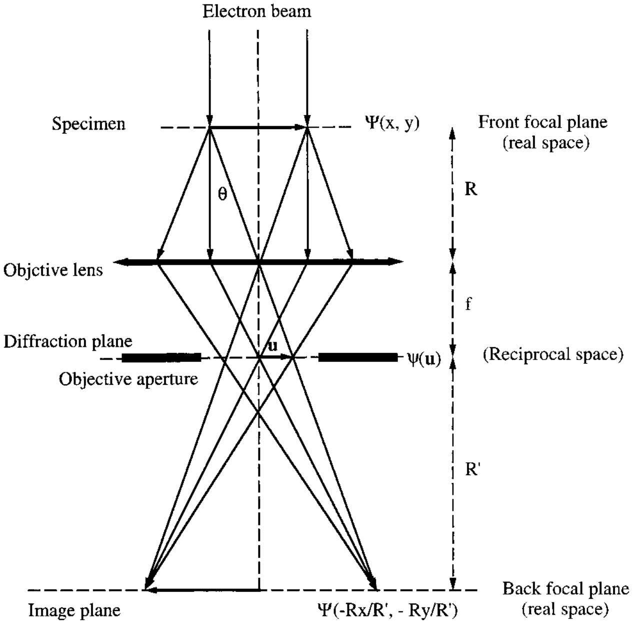

Figure 3-2. Abbe's theory of image formation in an one-lens transmission electron microscope. This theory is for a general optical system in TEM.

Waves leaving the specimen in the same direction (or angle θ with the optic axis) are brought together at a point on the back focal plane, forming a diffraction pattern. The electrons scattered to angle θ experience a phase shift introduced by the chromatic and spherical aberrations of the lens, and this phase shift is a function of the scattering angle, thus, the diffraction amplitude at the back-focal plane is modified by

$$\psi'(\mathbf{u}) = \psi(\mathbf{u}) \exp[i\chi(\mathbf{u})] \qquad (3\text{-}1)$$

where $\psi(\mathbf{u})$ is the Fourier transform of the wave $\Psi(\mathbf{r})$ at the exit face of the specimen, $\mathbf{u}$ is the reciprocal space vector that is related to the scattering angle by $u = 2 \sin\theta / \lambda$, and $\chi(\mathbf{u})$ is determined by the spherical abberation coefficient C_s of the objective lens and the lens defocus Δf [3]

$$\chi(\mathbf{u}) = \frac{\pi}{2} C_s \lambda^3 u^4 - \pi \Delta f \lambda u^2 \qquad (3\text{-}2)$$

where λ is the electron wavelength. The aberration and defocus of the lens is to modulate the phases of the Bragg beams distributed in reciprocal space.

The electron image is the interference result of the beams scattered to different angles, and this interference pattern is affected by the phase modulation introduced by the aberration of the objective lens. The image is calculated according to

$$I(x,y) = |\Psi(\mathbf{r}) \otimes t_{obj}(x,y)|^2 \qquad (3\text{-}3)$$

where $\otimes$ indicates a convolution calculation of (x, y), $t_{obj}(x,y)$ is the inverse Fourier transform of the phase function $\exp[i\chi(\mathbf{u})]$. The convolution of the lens transfer function introduces the non-linear information transfer characteristics of the objective lens, leading to complexity in image interpretation.

3.2.2 Contrast mechanisms

Images in TEM are usually dominated by three types of contrast. First, diffraction contrast [4], which is produced due to a local distortion in the orientation of the crystal (by dislocations, for example), so that the diffracted intensity of the incident electron beam is perturbed, leading to contrast observed in bright-field image. The nanocrystals oriented with their low-index zone-axis parallel or nearly parallel to the incident beam direction usually exhibit dark contrast in the bright field image, that is formed by selecting the central transmitted beam. Since the diffraction intensities of the Bragg reflected beams are strongly related to the crystal orientations, this type of image is ideally suited for imaging defects and dislocations. For nanocrystals, most of the grains are defect-free in volume, while a high density of defects are localized at the surface or grain boundary, diffraction contrast can be useful for capturing strain distribution in nanocrystals whose sizes are larger than 15 nm. For smaller size nanocrystals, since the resolution of diffraction contrast is in the order of 1–2 nm, its application is limited.

Secondly, phase contrast is produced by the phase modulation of the incident electron wave when transmits through a crystal potential [1]. This type of contrast is sensitive to the atom distribution in the specimen and it is the basis of high-resolution TEM. To illustrate the physics of phase contrast, we consider the modulation of a crystal potential to the electron wavelength. From the *de Brogli relation*, the wavelength λ of an electron is related to its momentum, p, by

$$\lambda = \frac{h}{p} \tag{3-4}$$

When the electron goes through a crystal potential field, its kinetic energy is perturbed by the variation of the potential field, resulting in a phase shift with respect to the electron wave that travels in a space free of potential field. For a specimen of thickness d, the phase shift is

$$\phi \approx \sigma V_p(\mathbf{b}) = \sigma \int_0^d dz\, V(\mathbf{r}) \tag{3-5}$$

where $\sigma = \frac{\pi}{\lambda U_0}$, $\mathbf{b} = (x, y)$, U_0 is the acceleration voltage, and $V_p(\mathbf{b})$ the thickness-projected potential of the crystal. Therefore, from the phase point of view, the electron wave is modulated by a phase factor

$$Q(\mathbf{b}) = \exp[i\sigma V_p(\mathbf{b})] \tag{3-6}$$

This is known to be the *phase object approximation*. (POA), in which the crystal acts as a phase grating filter. If the incident beam travels along a low-index zone-axis, the variation of $V_p(\mathbf{b})$ across atom rows is a sharp function because an atom can be approximated by a narrow potential well and its width is in the order of 0.2–0.3 Å. This sharp phase variation is the basis of *phase contrast*, the fundamental of atomic-resolution imaging in TEM.

Finally, mass-thickness or atomic number produced contrast. Atoms with different atomic numbers exhibit different powers of scattering. If the image is formed by collecting the electrons scattered to high-angles, the image contrast would be sensitive to the average atomic number along the beam direction. This type of imaging is usually performed in STEM (see Chapter 4).

3.2.3 Image interpretation

In high-resolution TEM (HRTEM) images, one usually wonders if the atoms are dark or bright. To answer this question one must examine the imaging conditions. For the clarity of following discussion, the *weak scattering object approximation* (WPOA) is made. If the specimen is so thin that the projected potential satisfies $|\sigma V_p(\mathbf{b})| << 1$, the phase grating function is approximated by

$$\Psi(\mathbf{b}) \approx 1 + i\sigma V_p(\mathbf{b}) \tag{3-7}$$

From Eq. (3-3) and ignoring the σ^2 term, the image intensity is calculated by

$$I(x,y) \approx 1 - 2\,\sigma V_p(\mathbf{b}) \otimes t_s(\mathbf{b}) \tag{3-8}$$

where $t_s(\mathbf{b}) = \mathrm{Im}[t_{obj}(\mathbf{b})]$. The second term in Eq. (3-8) is the interference result of the central transmitted beam with the Bragg reflected beams. Any phase modulation introduced by the lens would result in contrast variation in the observed image. Under the Scherzer defocus, $t_s(\mathbf{b})$ is approximated to be a negative Gaussian-like function with a small oscillating tail, thus, the image contrast, under the WPOA, is directly related to the two-dimensional thickness-projected potential of the crystal, and the image reflects the projected structure of the crystal. This is the basis of structure analysis using HRTEM. On the other hand, the contrast of the atom rows is determined by the sign and real space distribution of $t_s(\mathbf{b})$. The convolution of $t_s(\mathbf{b})$ with the potential changes the phases of the Bragg reflected beams, which can be explicitly illustrated as following.

A Fourier transform is made to the both sides of Eq. (3-8), yielding

$$\mathbf{FT}[I_p] \approx \delta(\mathbf{u}) - 2\,\sigma\mathbf{FT}[V_p(\mathbf{b})]\; T_s(\mathbf{u}) \tag{3-9}$$

The $\delta(\mathbf{u})$ function represents a strong central transmitted (000) beam. The Fourier transform of the crystal potential, $\mathbf{FT}[V_p(\mathbf{b})]$, is the diffraction amplitude of the Bragg beams under the kinematic scattering approximation. The contribution from each diffracted beam to the image is modified by the function $T_s(\mathbf{u}) = \sin\chi\; E(\mathrm{u})$, and $E(\mathrm{u})$ is the envelope function due to a finite energy spread of the source, the focus spread, beam convergence, the mechanical vibration of the microscope, the specimen drift during the recording of the image, and electric voltage and lens current instability. The envelope function defines the maximum cut-off frequency that can be transferred by the optic system. $T_s(\mathbf{u})$ is known as the *phase-contrast transfer function* (PCTF), characterizing the information transfering property of the objective lens. To illustrate this result, we consider a *fcc* structured crystal which gives {111}, {200}, {220} and {311} reflections. The angular distribution of these beams are schematically shown on the horizontal u axis. The diffraction amplitudes $\phi_{\{111\}}$ and $\phi_{\{220\}}$ of beams {111} and {220}, respectively, are chosen as two representatives to show the characteristics of

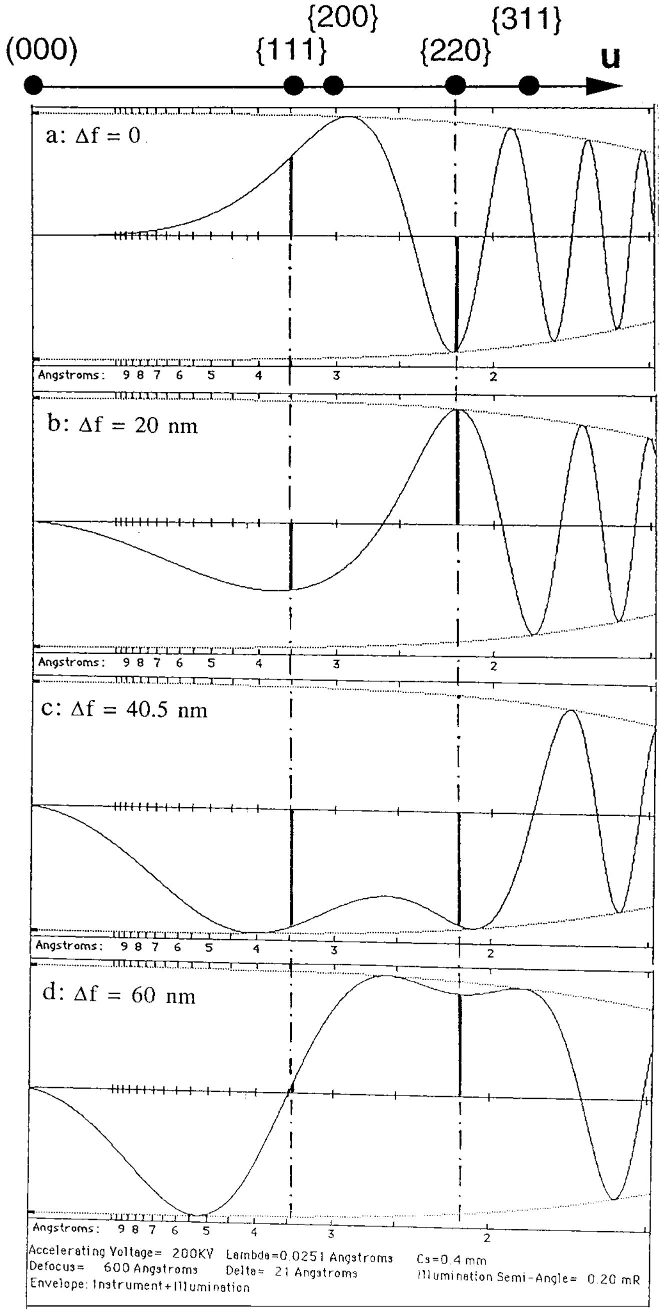

Figure 3-3. Calculated contrast transfer function sinχ for several defocus values showing information transfer under different conditions (see text). The horizontal axis is labeled with the corresponding image resolution R (in Å), corresponding to a reciprocal space vector $\mathbf{u} = 1/R$. The dashed lines indicate the angular positions of the {111} and {220} beams.

phase transfer. When the defocus is zero (Figure 3-3a), $\phi_{\{111\}}$ is transferred with positive sign ($\sin\chi > 0$), while $\phi_{\{220\}}$ is transferred with negative sign ($\sin\chi < 0$). The sign reverse of $\phi_{\{220\}}$ with respect to $\phi_{\{111\}}$ results in a contrast reversal in the interference pattern due to the destructive summation of the two. At $\Delta f = 20$ nm (Figure 3-3b), the two amplitudes are transferred with the same sign except the relative weight factor of the two is changed. At $\Delta f = 40.5$ nm (Figure 3-3c), $\phi_{\{111\}}$ and $\phi_{\{220\}}$ are both transferred with the negative sign, and there is no relative phase change between $\phi_{\{111\}}$ and $\phi_{\{220\}}$, thus, the interferences between $\phi_{\{000\}}$, $\phi_{\{111\}}$ and $\phi_{\{220\}}$ give the image that is directly related to the crystal structure (i.e., the atom rows and planes).

The PCTF depends sensitively on the defocus of the objective lens. The interpretable image resolution that is directly associated with the crystal structure (e.g., the structural resolution) is determined by the width of the information passing band. It was first investigated by Scherzer [5] that the highest structural resolution of $R = 0.66\ \lambda^{3/4}\ C_s^{1/4}$ would be obtained at defocus $\Delta f = (4/3\ C_s\lambda)^{1/2}$. In this focus condition, the $t_s(\mathbf{b})$ function is approximated to be a negative Gaussian function, thus, the atoms tend to be in dark contrast for thin crystals. This is the most desirable imaging condition of HRTEM.

As a summary, the image contrast in HRTEM is critically affected by the defocus value. A slight change in defocus could lead to contrast reversal. A change in signs of the diffraction amplitudes makes it difficult to match the observed image directly with the projection of atom rows in the crystal. This is one of the reasons that image simulation is a key step in quantitative analysis of HRTEM images.

3.2.4 Image simulation

Image simulation needs to include two important processes, the dynamic multiple scattering of the electron in the crystal and the information transfer of the objective lens system. The dynamic diffraction process is to solve the Schrödinger equation under given boundary conditions. There are several approaches for performing dynamic calculations [6]. For a finite size crystal containing defects and surfaces, the multislice theory is most adequate for numerical calculations. The multislice many-beam dynamic diffraction theory was first developed based on the physical optics approach [7]. The crystal is cut into many slices of equal thickness Δz in the direction perpendicular or nearly perpendicular to the incident beam (Figure 3-4). When the slice thickness tends to be very small the scattering of each slice can be approximated as a phase object, the transmission of the electron wave through each slice can be considered separately if the backscattering effect is negligible, which means that the calculation can be made slice-by-slice. The defect and 3-D crystal shape can be easily accounted for in this approach.

The transmission of the electron wave through a slice can be considered as a two step processes – the phase modulation of the wave by the projected atomic potential within the slice and the propagation of the modulated wave in "vacuum" for a distance Δz along the beam direction before striking the next crystal slice. The wave function before and after transmitting a crystal slice is correlated by

$$\Psi(\mathbf{b},z+\Delta z) = [\Psi(\mathbf{b},z)\ Q(\mathbf{b},z+\Delta z)] \otimes P(\mathbf{b},\Delta z) \quad (3\text{-}10)$$

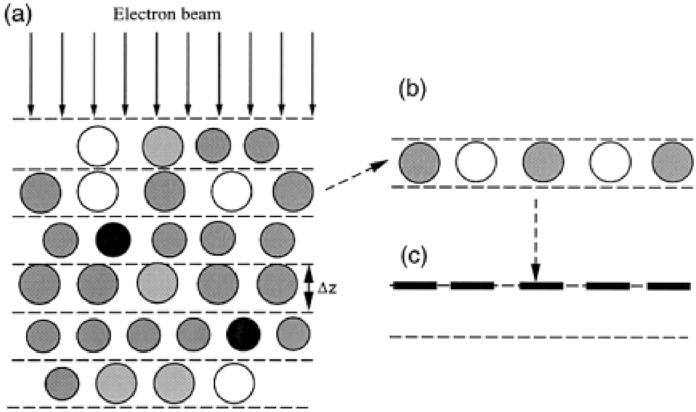

Figure 3-4. (a) A schematic diagram showing the physical approach of the multislice theory for image and diffraction pattern calculations in TEM. (b) Transmission of electron wave through a thin crystal slice. (c) An approximated treatment of the wave transmission through a thin slice.

where $Q(\mathbf{b},z+\Delta z) = \exp[i\sigma\int_{z}^{z+\Delta z} dz V(\mathbf{b},z)]$ is the phase grating function of the slice, and $P(\mathbf{b},\Delta z) = \frac{\exp(\pi i K|\mathbf{b}|^2/\Delta z)}{i\lambda\Delta z}$ is the propagation function. The most important characteristic of this equation is that no assumption was made regarding the arrangement of atoms in the slices, so that the theory can be applied to calculate the electron scattering in crystals containing defects and dislocations. This is the most powerful approach for nanocrystals.

The next step is the information transfer through the objective lens system. By taking a Fourier transform of the exit wave function, the diffraction amplitude is multiplied by the lens transfer function $\exp(i\chi)\ E(u)$, where the defocus is a variable. The defocus value of the objective lens and the specimen thickness are two important pa-

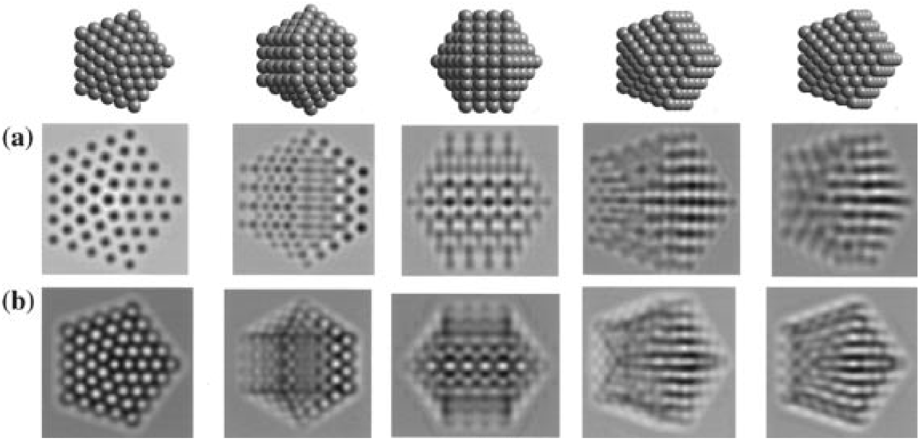

Figure 3-5. Theoretically simulated images for a decahedral Au particle at various orientations and at focuses of (A) Δf = 42 nm and (B) Δf = 70 nm. The Fourier transform of the image is also displayed (Courtsey of Drs. Ascencio and M. José-Yacamán).

rameters which can be adjusted to match the calculated images with the observed ones. Figure 3-5 shows systematic simulations of a decahedral Au particle in different orientations. The particle shape can only be easily identified if the image is recorded along the five-fold axis [8]. The group A and group B images were calculated for two different defocuses, exhibiting contrast reversal from dark atoms to bright atoms. In practice, with consideration the effects from the carbon substrate, it would be difficult to identify the particle shape if the particle orientation is off the five-fold axis.

3.3 Defects in nanophase materials

Nanocrystals exhibiting distinctly different properties from the bulk are mainly due to their large portions of surface atoms and the size effect and possibly the shape effect as well. A particle constituting a finite number of atoms can have a specific geometrical shape, and most of the defects are on the surface, while the volume defects are dominated by twins, stacking faults and point defects. Surface defects and planar defects can be imaged directly using HRTEM, but the analysis of point defects is still a challenge.

3.3.1 Polyhedral shape of nanoparticles

Surface energies associated with different crystallographic planes are usually different, and a general sequence may hold, $\gamma_{\{111)} < \gamma_{\{100)} < \gamma_{\{110)}$. For a spherical single-crystalline particle, its surface must contain high index crystallography planes, which possibly result in a higher surface energy. Facets tend to form on the particle surface to increase the portion of the low index planes. Therefore, for particles smaller than 10-20 nm, the surface is a polyhedron. Figure 3-6a shows a group of cubo-octahedral

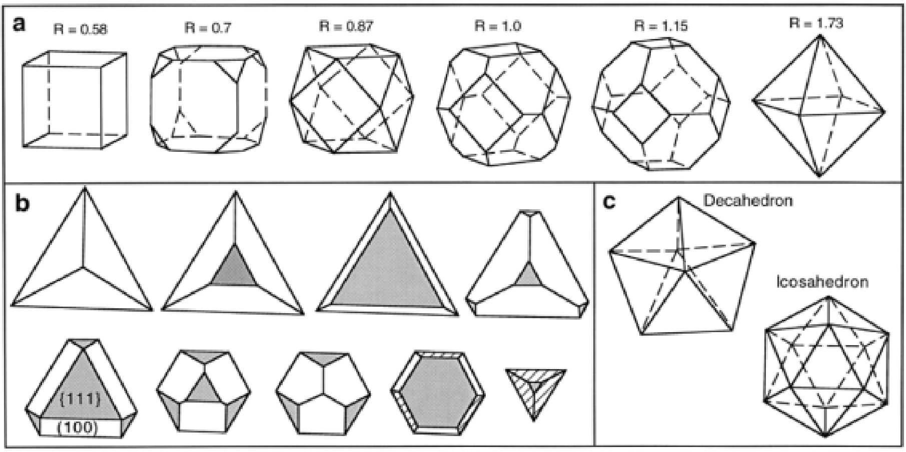

Figure 3-6. (a) Geometrical shapes of cubo-octahedral nanocrystals as a function of the ratio, *R*, of the growth rate along the <100> to that of the <111>. (b) Evolution in shapes of a series of (111) based nanoparticles as the ratio of {111} to {100} increases. The beginning particle is bounded by three {100} facets and a (111) base, while the final one is a {111} bounded tetrahedron. (c) Geometrical shapes of multiply twinned decahedral and icosahedral particles.

shapes as a function of the ratio, R, of the growth rate in the <100> to that of the <111>. The longest direction in a cube is the <111> diagonal, the longest direction in the octahedron is the <100> diagonal, and the longest direction in the cubo-octahedron ($R = 0.87$) is the <110> direction. The particles with $0.87 < R < 1.73$ have the {100} and {111} facets, which are named the truncated octahedral (TO). The other group of particles has a fixed (111) base with exposed {111} and {100} facets (Figure 3-6b). An increase in the area ratio of {111} to {100} results in the evolution of particle shapes from a triangle-based pyramid to a tetrahedron.

If the particle is oriented along a low index zone axes, the distribution of atoms on the surface can be imaged in profile, and the surface structure is directly seen with the full resolution power of an TEM [9, 10]. This is a powerful technique for direct imaging the projected shapes of nanoparticles particularly when the particle size is small. With consideration the symmetry in particle shapes, HRTEM can be used to determine the 3-D shape of small particles although the image is a 2-D projection of a 3-D object.

Figure 3-7a gives a profile HRTEM image of a cubic Pt nanocrystals oriented along [001] [11]. The particle is bounded by {100} facets and there is no defect in the bulk of the particle. The distances between the adjacent lattice fringes is the interplanar distance of Pt {200), which is 0.196 nm, and the bulk structure is face centered cubic. The surface of the particle may have some steps and ledges particularly at the regions near the corners of the cube. To precisely image the defects and facets on the cubic particles, a particle oriented along [110] is given (Figure 3-7b). This is the optimum orientation for imaging cubic structured materials. The {110} facets are rather rough, and the {111} facets are present. These higher energy structural features are present because the particles were prepared at room temperature.

An octahedron has eight {111} facets, four {111} facets are edge-on if viewed along [110] . If the particle is a truncated octahedron, six {100} facets are created by cutting the corners of the octahedron, two of which are edge-on while viewing along [110]. Figures 3-8a and b show the HRTEM images of [110] oriented truncated octahedron and octahedral Pt particles, respectively. A variation in the area ratio of {100} to {111} results in a slight difference in particle shapes.

A tetrahedral particle is defined by four {111} faces and it usually gives a triangular shape in HRTEM. Figure 3-9 gives two HRTEM images of truncated tetrahedral particles oriented along [110]. Two {111} facets and one {001} facet (at the top of the

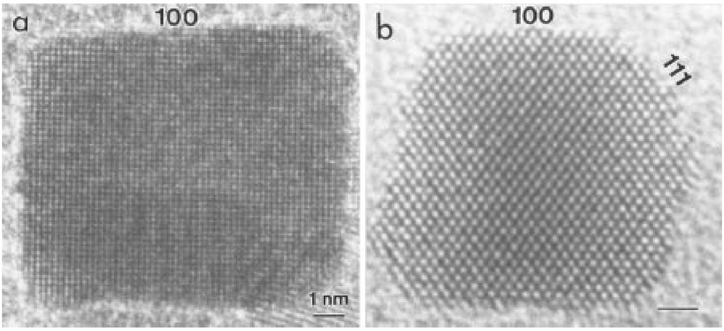

Figure 3-7. HRTEM images of cubic Pt nanocrystals oriented along (a) [001] and (b) [110], showing surface steps/ledges and the thermodynamically unequilibrium shapes.

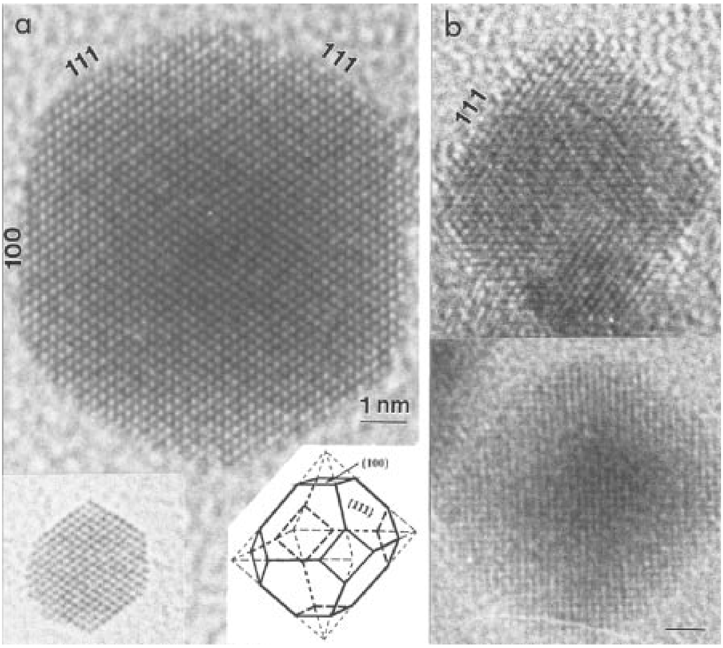

Figure 3-8. HRTEM images of Pt nanocrystals (a) with a truncated octahedral shape and oriented along [110], and (b) with a octahedral shape and oriented along [110] and [001]. The inset in (a) is a model of the particle shape.

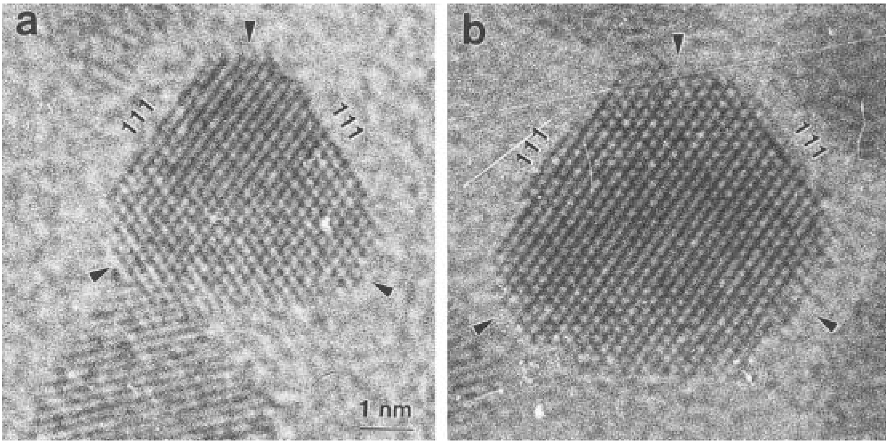

Figure 3-9. HRTEM images of truncated tetrahedral Pt nanocrystals oriented along [110]. The surface steps and ledges at the truncated corners are clearly resolved.

image as a result of truncation) are imaged edge-on. There are some atom-high surface steps on the {111} surfaces and the corners. These atomic-scale structures are likely important for enhancing the catalysis activities of the nanocrystals.

3.3.2 Surface reconstruction

Simply speaking, surface atoms have less bonds in comparison to the atoms in the bulk because of the loss in nearest neighbors. The surface atoms tend to find new equilibrium positions to balance the forces, resulting in surface reconstruction. The most typical example is the Si {111} 7×7 reconstruction [12]. Surface restructure can be the rearrangement of the surface atoms and/or the relaxation of the top few layers. A classical example of surface reconstruction in nanocrystals is the Au (110) 2×1 [13].

Figure 3-10 gives a group of images recorded from Pt nanocrystals. The {111} faces in Figures 3-10a, c and d are relatively flat, while the {100} faces show a large deviation from the perfect lattice structure, suggesting the occurrence of a non-ordered surface reconstruction. Surface relaxation is clearly seen in Figure 3-10b in the layers indicated by arrowheads. Surface stress due to the capillary effect may have significant influence on the lattice constant of nanocrystals [14, 15].

Figure 3-11a gives a bright-field TEM image of a monolayer self-assembled Pt nanocrystals, most of which are single crystalline without twins or stacking faults. The dark-field image is formed using an objective aperture that selects a small section of the {111} and {200} reflection rings, so that the particles whose Bragg reflections falling into the angular range of the aperture would display bright contrast, while those not falling into the angular range are expected to exhibit dark-contrast. The dark-field image, however, displays some ring contrast in some of the particles. The size of the rings corresponds well to the actual size of the particles in the bright-field TEM image and the ring contrast is not the thickness fringes because the particle size is less than

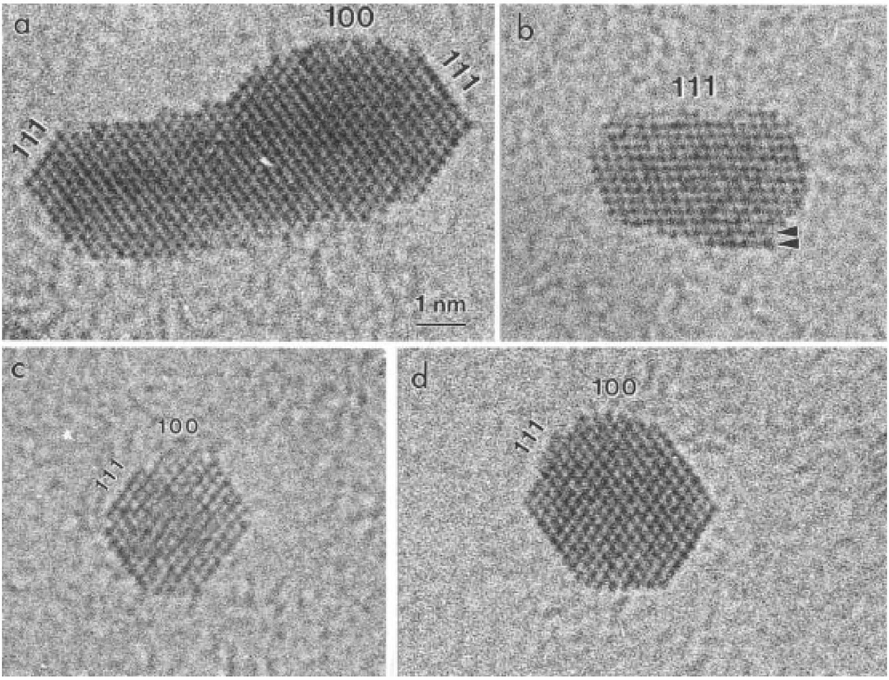

Figure 3-10. HRTEM images of Pt nanocrystals oriented along [110], showing the reconstructed {100} surfaces and surface relaxation (indicated by arrowheads).

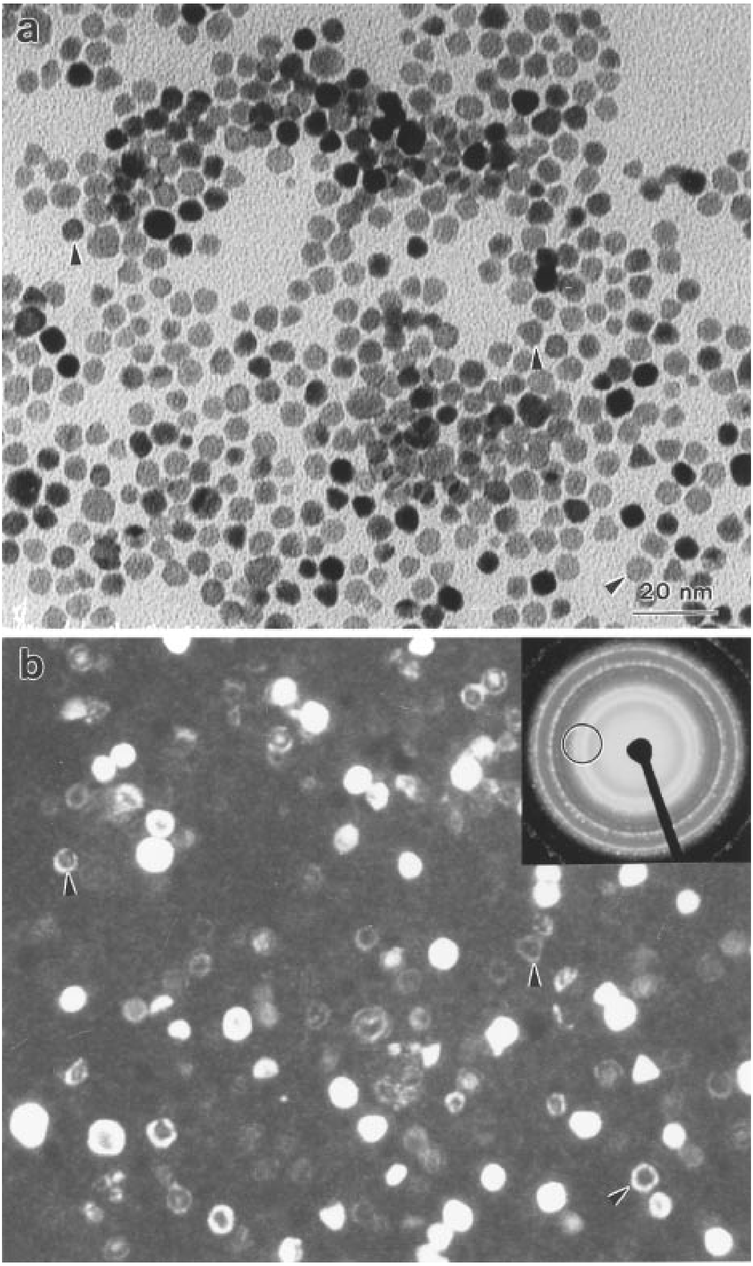

Figure 3-11. A pair of (a) bright-field and (b) dark-field images from Pt nanocrystals, showing a ring shape contrast in the dark field image (see the particles indicated by arrowheads), which is likely due to the diffuse scattering from the surface reconstructed/relaxed layers. The dark field image was recorded using a small objective aperture, as shown in the inserted electron diffraction pattern, positioned on the {111} and {200} reflection rings.

10 nm, smaller than the extinction distances of Au {111) (15.9 nm) and Au (200) (17.9 nm). This type of contrast is due to the diffuse scattering generated from the top few atomic layers of the nanocrystal owing to surface reconstruction/relaxation. A non periodic perturbation to the crystal lattice would produce diffuse scattering that is distributed between the Bragg reflections in the entire diffraction plane. In the angular selection range of the aperture, the particles whose Bragg reflections are not falling into the aperture should be completely dark, but the diffuse scattering from the particles would be partially collected, resulting in a bright ring at the edge of the particle. This is another way to image the reconstruction/relaxation of the surface atoms in nanocrystals.

3.3.3 Twining structure and stacking faults

Twining is one of the most popular planar defects in nanocrystals, and it is frequently observed for fcc structured metallic nanocrystals. Twining is the result of two subgrains by sharing a common crystallographic plane, thus, the structure of one subgrain is the mirror reflection of the other by the twin plane. Figure 3-12a gives a HRTEM image of a Pt particle oriented along [110], which is composed of two grains connected at a twin relation. The twin plan is indicated by a dotted line. The fcc structured metallic nanocrystals usually have {111} twins, which is the fundamental defect mechanism for the growth of spherical-like particles (see Section 3.2.4).

Stacking faults are a typical planar defect. Stacking faults are produced by a distortion on the stacking sequence of atom planes. The (111) plane stacking sequence of a *fcc* structure follows A-B-C-A-B-C-A-B-C-. If the stacking sequence is changed to A-B-C-A-B-A-B-C-, a stacking fault is created. Figure 3-12b shows an Au particle that contains a twin and a stacking fault. It is know that nanocrystals usually contain no dislocation but strain. Twins and stacking faults are created probably due the high strain energy in the volume.

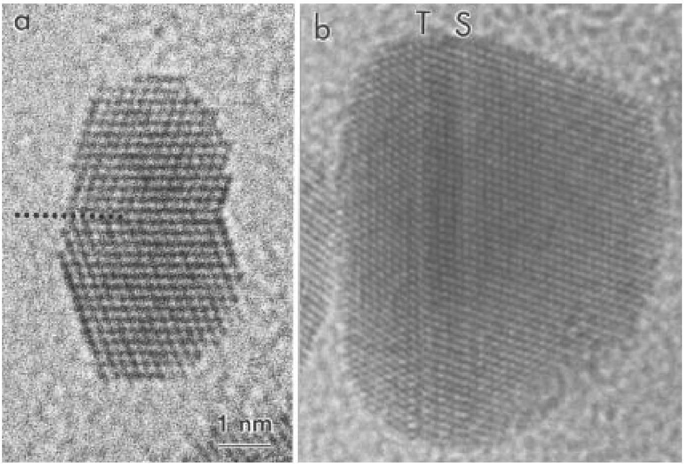

Figure 3-12. HRTEM images of Pt nanocrystals having twin (T) and stacking fault (S) structures. The nanocrystals are oriented along [110] and the twin plane and stacking fault are parallel to the direction of the electron beam.

3.2.4 Decahedral and icosahedral particles

The two most typical examples of multiply twinned particles (MTP) are decahedron and icosahedron [16, 17]. Starting from a *fcc* structured tetrahedron, a decahedron is assembled from five tetrahedral sharing an edge (Figure 3-13a). If the observation direction is along the five-fold axis and in an ideal situation, each tetrahedron shares an angle of 70.5°, five of them can only occupy a total of 352.6°, leaving a 7.4° gap. Therefore, strain must be introduced in the particle to fill the gap [18]. An icosahedron is assembled using 20 tetrahedra via sharing an apex (Figure 3-13b and c). The icosahedral and decahedral particles are the most extensively studied twinned nanocrystals [19–21].

The most easy orientation for identifying the MTPs are along the five fold symmetry axis. Figure 3-14a shows a large decahedral Au particle, the five fold twin structure is clearly seen. The strain inteoduced is also visible. High-resolution TEM image for a smaller one clearly shows the crystal structure of the particle (Figure 3-14b). Identification the shape of small MTPs in TEM is not trivial because the image depends sensitively on the orientation of the particle [8, 21]. With the presence of a thin amorphous carbon substrate, it is even more difficult to identify the particle shape directly.

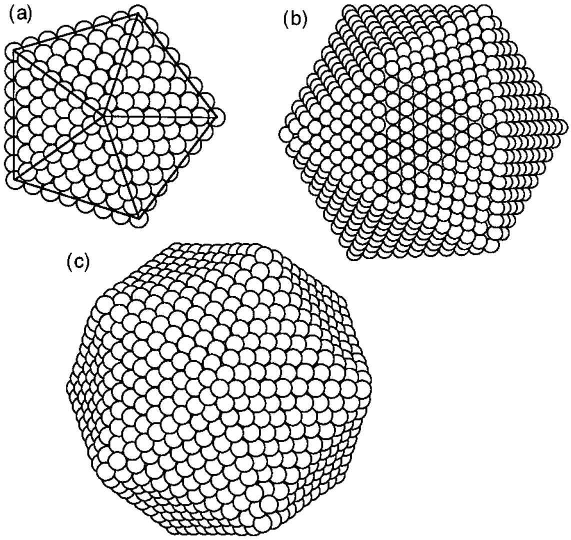

Figure 3-13. Atomic models of (a) decahedral, (b) and (c) icosahedral nanocrystals.

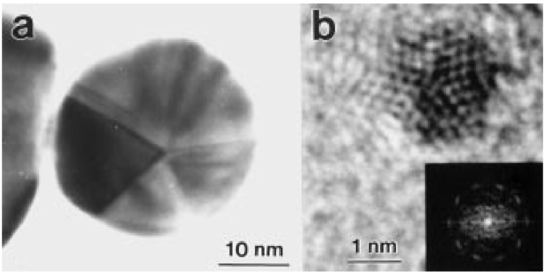

Figure 3-14. TEM images of decahedral Au nanocrystals when the incident electron beam is parallel or nearly parallel to the five-fold symmetry axis. The strain field introduced by the five-fold twins is apparent in (a). A Fourier transform of the image clearly reveals the five-fold symmetry.

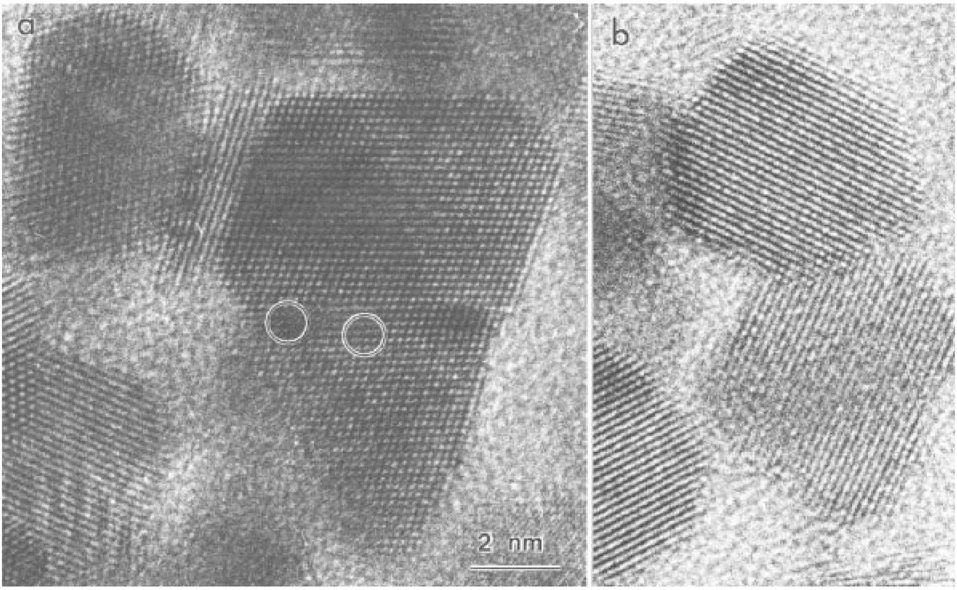

Figure 3-15. HRTEM observations of dislocations at low-angle and high-angle grain boundaries of Pt nanocrystals.

3.3.5 Interface defects and dislocations

Engineering materials made of nanocrystals must involve grain boundaries. The misorientation or lattice mismatch between nanocrystals creates interface dislocations. Figure 3-15a shows a coherent interface formed by two Pt nanocrystals, where the lattices of the two particles are closely aligned and matched fairly well, while edge dislocations are still seen at regions indicated by the circles. Edge dislocations are commonly seen at interfaces to accommodate the accumulated strain created by lattice rotation/mismatch. The interface angle of a coherent interface is usually small. The interface seen in Figure 3-15b is a large angle grain boundary, where the lattices exhibit large incoherence and the grain boundary energy is expected to be higher.

3.4 Electron holography

In conventional HRTEM, the phase and amplitude images of the exit electron wave are mixed non-linearly and convoluted with the phase contrast transfer function. It is usually a rather sophisticated and complex process to retrieve the phase and amplitude images. Electron holography is a technique which can recover the true object image. There are numerous ways of performing electron holography in TEM and STEM [22]. The most popular technique is the off-axis holography. The principle of electron holography was first introduced by Gabor [23] in an attempt to exceed the point-to-point resolution of an electron microscope. Holography is based on the interference and diffraction properties of waves, thereby producing a true image of an object (including amplitude and phase) without any distortion of the lenses. The

development of high-brightness high-coherence electron sources has made it possible to obtain holograms using electron waves in TEM [24–26]. The high spatial coherence of the source is the key to perform holography.

3.4.1 Principle of off-axis holography in TEM

Electron holography is designed as a two-step imaging technique [27]. The first step is to form an interference hologram as shown in Figure 3-16a. A high spatial coherent electron wave is emitted from the source, half of which will transmit through a thin specimen and the other half is reserved as a reference wave. The reference wave is the standard to determine the phase shift image of the wave went through the specimen. The interference of the two waves is possible by inserting a positively charged biprism at the intermediate focal plane of the projection lenses. The biprism defects the electrons on the both sides towards with each other and introduce an additional phase shift function due to the Aharonov-Bohm effect, resulting in the formation of an interference hologram.

The second step is to reconstruct the phase image from the hologram (Figure 3-16b). This can be achieved optically or digitally. In the optical reconstruction, a laser beam illuminates the recorded hologram. Due to the presence of interference fringes in the hologram, the transmitted beam will be diffracted along the direction perpendicular to the fringes, forming two side-bands and a center band. The side-band is directly associated with the electron wave function at the exit face of the specimen, and it gives both the amplitude and phase images of the object.

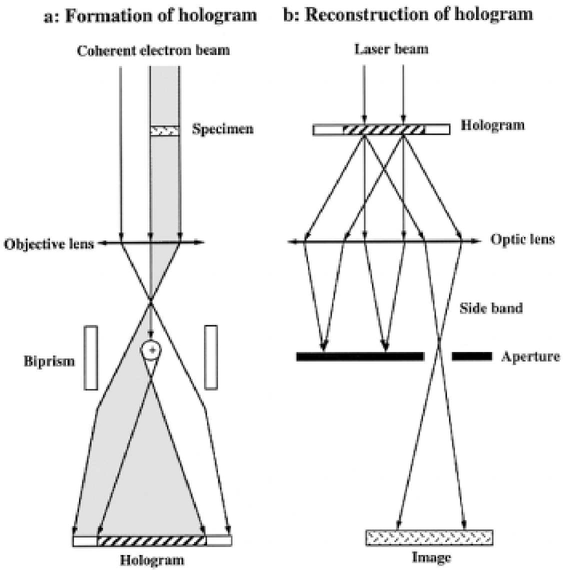

Figure 3-16. (a) Formation of off-axis electron hologram in TEM using an electrostatic biprism, and (b) reconstruction of electron hologram using laser diffraction.

3.4.2 Imaging electrostatic field and charge distribution

The phase image can provide the distribution of electrostatic field around a charged particle as well as the thickness projected potential image of a nanocrystal. The former can be used to extract the charge distribution in the particle [28], and the latter is useful to determine if the particle contains a hard core or an empty cavity [29]. This measurement is based on the electron phase shift after transmission a region with electrostatic potential. The perturbation of the field to the electron wave results in a change in the electron wavelength. From the discussion given in Section 3.2.2, the relative phase shift of the electron wave with respect to the reference wave is given by Eq. (3-5). For a homogeneous specimen with constant thickness, in addition to the average potential introduced by the atoms in the crystal, charge barrier can be created at interfaces and defects. If the former contributes only a background, the latter can be retrieved experimentally.

Figure 3-17 shows a phase image of the MgO cubic crystal oriented along [210]. The MgO cube is bounded by four {100} faces. A thickness projection of the cube along [210] results in rapid variation in the projected mass-thickness towards the edge of the cube, while there is no change in the projected-thickness at the center (see the inset). This result is clearly revealed by the phase image reconstructed from the hologram.

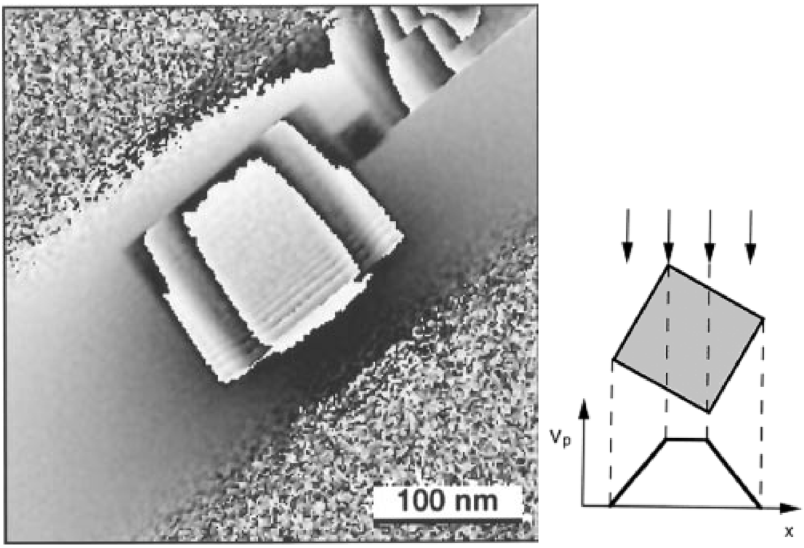

Figure 3-17. A phase image of a MgO cube oriented along [210], showing the phase variation resulted from the change in the projected potential. A schematic model of the projection geometry is given, where the profile of the projected potential across the particle is illustrated (Courtesy of Dr. B. Frost).

3.4.3 Imaging magnetic domains and flux lines

Imaging of magnetic domains and interdomain interaction is vitally important for understanding the behavior and improving the properties of magnetic materials. Although domain structures can be directly seen using Fresnel contrast and Lorentz mi-

croscopy, electron holography is probably the only technique which can provide quantitative information about the structure of domains and the field distribution around it [24, 30]. The mechanism of imaging magnetic domains in magnetic materials relies on the Aharonov-Bohm effect [31], which describes the relative phase shift of the two electron waves traveling along two routes enclosing a zone with magnetic field distribution,

$$\Delta\phi = \frac{2\pi e}{h}\int_s \mathbf{B}\cdot d\mathbf{S} \tag{3-11}$$

where d**S** is a surface integral over the area enclosed by the two routes. Equation (3-11) means that the phase difference is determined by the magnetic flux enclosed by the two electron trajectories. If a magnetic specimen is inset on the way of the object wave, measurement of the electron phase shift directly gives the magnetic flux enclosed by the two trajectories. Figure 3-18a is a bright-field TEM image of a barium ferrite particle with a truncated octahedral shape. The phase image of the particle

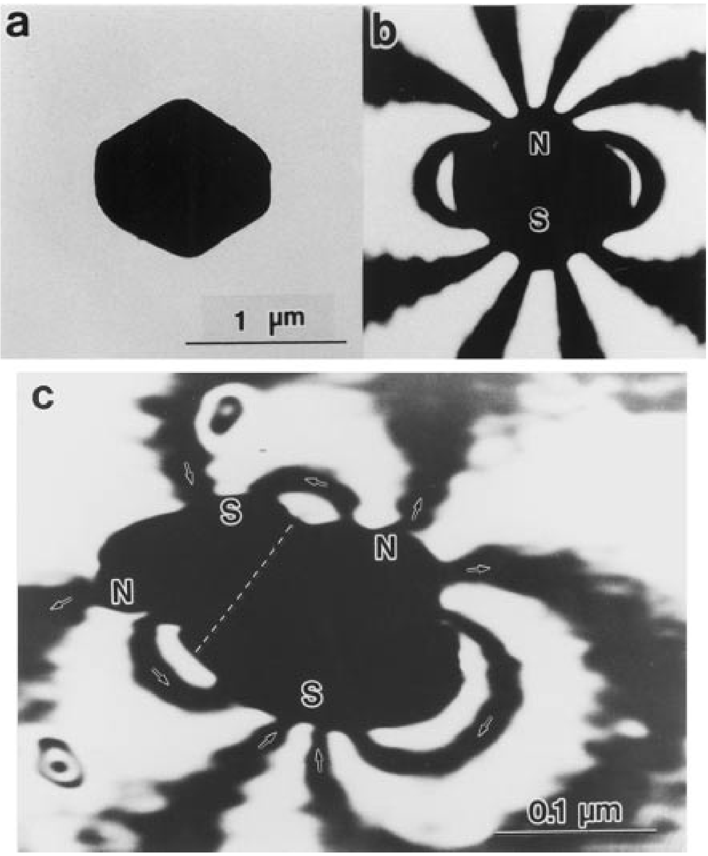

Figure 3-18. (a) A bright-field TEM image of a barium ferrite particle and (b) the corresponding phase image of the particle, reconstructed from a hologram, exhibiting the distribution of magnetic force lines. This particle is single domain. (c) Phase image of a two-domain magnetic barium ferrite particle. The phase is magnified ten time to amplify the effect (Courtesy of Drs. T. Hirayama and A. Tonomura).

(Figure 3-18b) shows the single magnetic domain structure, where the N and S poles of the magnetic domain can be clearly identified [32]. A particle consisting of two domains is given in Figure 3-18c and the domain size can be as small as 80 nm.

A key step in observation of magnetic flux lines is to create a magnetic field-free zone in which the specimen to be examine is placed. This can be achieved either by switching off the objective lens or by using a Lorentz objective lens. In the former, the experiments can be performed using a conventional TEM equipped with an FEG at the expense of image magnification, which is usually reduced by 50–80 times. The image resolution is also greatly reduced. Thus, the technique can only be applied to image magnetic domains of large sizes. On the other hand, the concomitant reduction in image magnification can be compensated by the optics of the electron energy filtering system attached to the microscope, which provides an addition magnification of 25x (at the CCD plane), thus, a magnification as large as 450,000x can be achieved, which is suitable for imaging particles smaller than 10 nm. Unfortunately, the image resolution is still limited by the aberration effects of the intermediate lenses and the projection lenses. With the use of a Lorentz lens the image magnification is unsacrificed and the image resolution is still preserved.

3.5 In-situ microscopy

In-situ studying the temperature induced phase transformation, structural and chemical evolution of nanocrystals are important for understanding the structure and structural stability of nanomaterials. TEM is an ideal system for conducting this type of experiments, in which a specimen can be cooled down to the liquid nitrogen or liquid helium temperature or heated to 1300 °C. The in-situ process can be recorded at TV rate (27 frames per second) for exhibiting the time and temperature dependent phenomena. In-situ observation can also be carried out for the mechanical stress, electric current and magnetic field induced phenomena. This section focuses mainly on the in-situ behavior of nanocrystals due to the effects of temperature and electric field.

3.5.1 Thermodynamic properties of nanocrystals

The large percentage of surface atoms in nanocrystals is the origin of their unique properties. The melting of Pt particles and the surface sublimation of Au nanorods are taken here as examples to illustrate the unusual thermodynamic properties of nanocrystals. The catalytic activity and selectivity of nanosize colloidal platinum (Pt) nanocrystals may depend strongly on their sizes and shapes. We had successfully demonstrated that platinum nanoparticles with a high percentage of cubic-, tetrahedral- and octahedral-like shapes, respectively, can be synthesized by changing the ratio of the concentration of polymer capping material (polyacrylate) to that of Pt^{2+} being reduced by H_2 from K_2PtCl_4 at room temperature [33]. The polymer acts not only as the passivative protection layer of the nanocrystals, but also the key factor in controlling their shapes [34, 35]. To determine the shape dependent catalytic behavior of Pt nanocrystals, the passivation layer on the nanocrystal must be removed. Several questions need to be considered: (1) how high does the annealing temperature need to be to remove the capping polymer while the particle shape is still preserved? (2) to what temperature is the particle shape still stable? (3) is there a temperature induced shape

transformation due to surface diffusion? and (4) how high is the melting point of the Pt particles? In-situ TEM observation of the particle shape transformation and melting can provide answers to these questions [36].

Figure 3-19 shows a series of TEM images recorded from the same region when the specimen temperature was increased from 25 to 610 °C. For easy notation, particles are labeled as groups to trace their shape transformation behavior. Most of the parti-

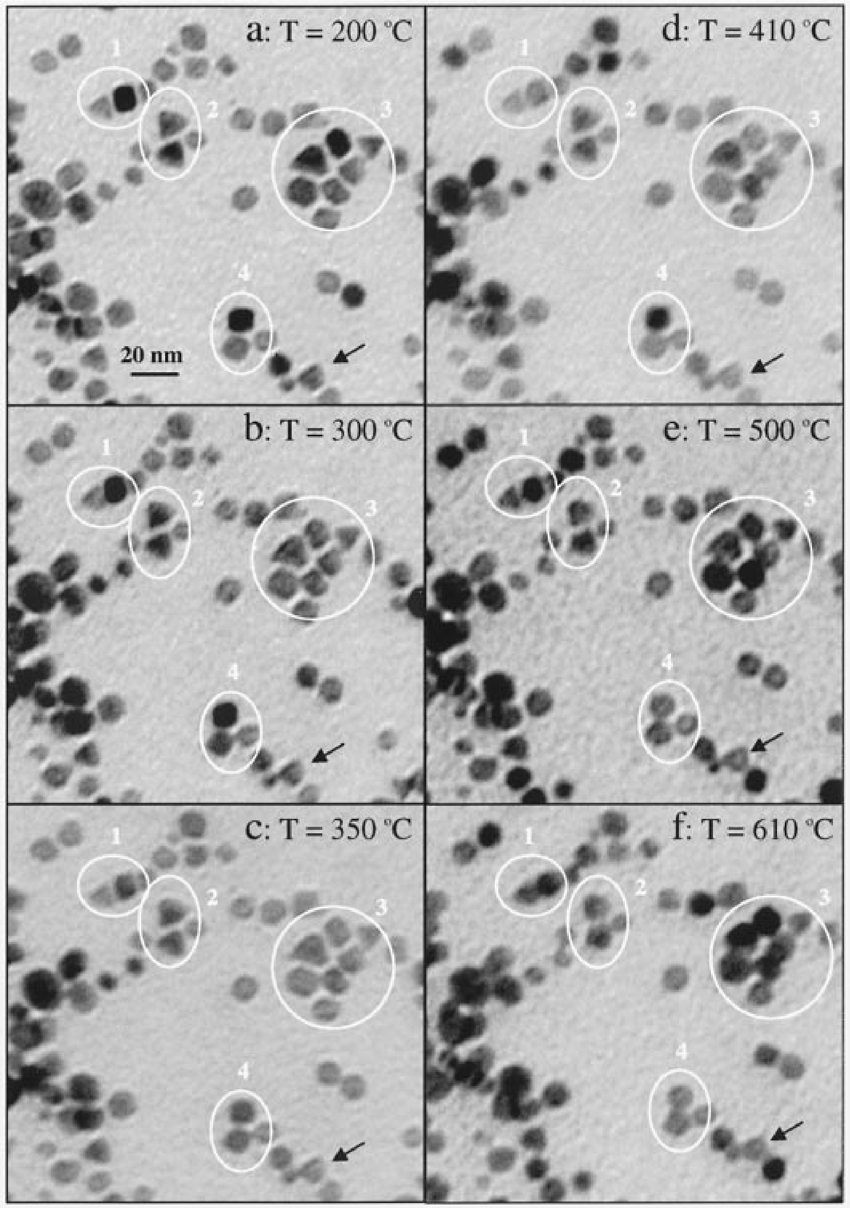

Figure 3-19. A series of in-situ TEM images recorded at different specimen temperatures, displaying the shape and structural transformation of Pt nanocrystals.

cle shapes showed no significant change when the specimen temperature was below 350 °C (Figures 3-19a-c). Truncated cubic and tetrahedral particles were formed when the temperature arrived 410 °C (Figure 3-19d). The corners and edges of the particles were disappearing because the local atoms have higher energy. The tetrahedral particles could still be identified even when the temperature reached 500 °C (Figure 3-19e), while the cubic particles became spherical-like when the temperature was above 500 °C. This indicates that the tetrahedral particles are more stable than cubic ones possibly because the {111} surfaces have lower surface energy than the {100}. A feature observed in Figure 3-19 is that the tetrahedral shape of a particle indicated by an arrowhead was preserved when the specimen temperature was as high as 610 °C. This is possibly due to the contact of the apexes of the particle with the adjacent particles, so that the interparticle diffusion can still sustain the shape of the apexes. Our results indicate that the surface capping polymer is removed by annealing the specimen to a temperature of 180–250 °C, while the particle shape shows no change up to ~ 350 °C. In a temperature range of 350 to 450 °C, a small truncation occurs in the particle shape but no major shape transformation. The particle shape experiences a dramatic transformation into spherical-like shape when the temperature is higher than ~ 500 °C.

The thermodynamic properties of nanocrystals depend strongly on not only the crystal size but also their shapes [37]. The thermodynamic properties of Au nanorods is an example. Gold nanorods were prepared by an electrochemical method [38]. To

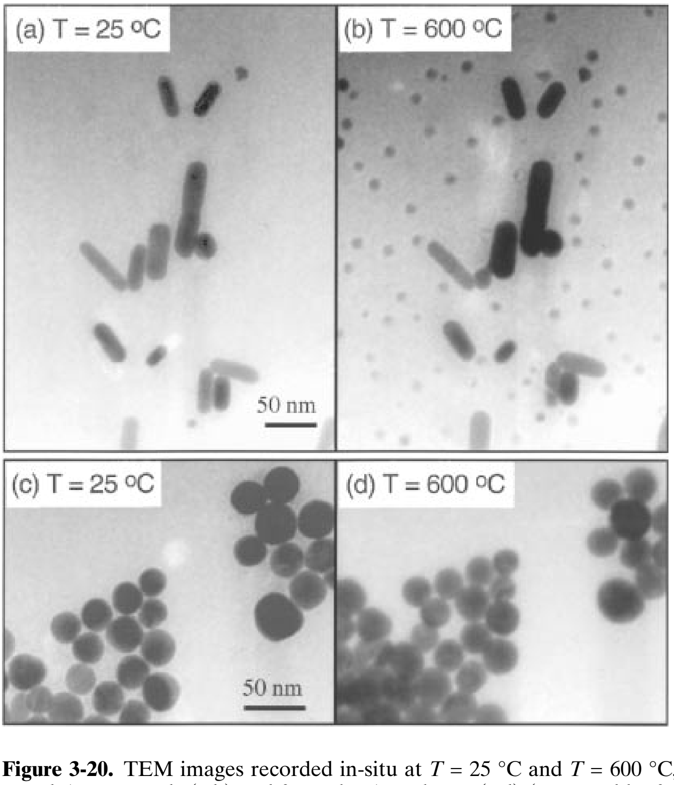

Figure 3-20. TEM images recorded in-situ at T = 25 °C and T = 600 °C, respectively, from the as-prepared Au nanorods (a,b) and from the Au spheres (c,d) (prepared by femtosecond laser photothermal conversion of the Au nanorods), showing the dependence of gold atoms sublimation rates on the shape of gold nanocrystals.

reveal the unique surface processes associated with Au nanorods, they were photoisomerized to form gold nanospheres by the influences of femtosecond laser pulses [39]. The structural evolution in the gold sphere and gold rods at 25 °C and 600 °C, respectively, is compared in Figs. 3-20 (a,b) and (c,d). Both the nanospheres and nanorods have the same average volume and almost equally exposed surface areas (with consideration of the contact of the particle with the substrate), thus, the size effect of the two geometrical shapes should not make a significant difference. After being heated to as low as 220 °C, small Au particles had formed on the substrate in the as-prepared nanorods specimen, while no particles were formed near the gold nanosphere. This clearly shows that the newly formed Au particles are unique characteristics of Au nanorods.

Using HRTEM, it has found that the nanorods have the unstable {110} facets [37], in addition to the {100} and {111} facets present in the spheres. For the face-centered Au nanocrystals, the surface energy follows a relationship of $\gamma_{\{110\}} > \gamma_{\{100\}} > \gamma_{\{111\}}$. The presence of a significant percentage of gold atoms on the {110} surface suggests that the nanorod is relatively thermodynamically unstable. The {111} and {100} faceted Au spheres have lower surface energy. Thus, their atoms may not sublime at relatively low temperatures. Therefore, the sublimation of Au atoms from the nanorods at lower temperatures may be contributed in part by the shape of the nanorods, which has the unstable {110} surfaces.

3.5.2 Electric field driven phenomena

In-situ structural evolution can also be driven by an electric field. Studying of domain boundary movement in ferroelectric crystals is an example. For nanocrystals, TEM provides a powerful approach for directly imaging the nanostructure under the application of an electric field/current.

A key step in this study is to build a specimen holder which can apply a controllable voltage across the specimen. We have demonstrated the study of quantum conductance of multiwalled carbon nanotubes [40, 41]. The nanotubes conduct current ballistically and don't dissipate heat. A current density of $J > 10^7$ A/cm^2 can pass a single nanotube at ambient temperature, setting a new record of room temperature superconductivity. These results strongly suggest that carbon nanotubes are ideal candidate of the interconnects in future molecular electronics.

Figure 3-21a shows an TEM image, in which a carbon fiber is connected with a mercury drop by a single carbon nanotube. The current conducted through the tube can be measured by applying a voltage across the two electrodes, and this measured transport property can be directly linked to the microstructure of the tube revealed by electron imaging and diffraction [42]. On the other hand, at the non-contacting case, an electric potential can be applied across the electrodes, resulting in charging up of the nanotube (Figures 3-21c). This is an ideal case for studying the field emission at individual nanotube. The electric field due to the electrostatic potential causes the charged nanotube to deflect, as can be seen by comparing the images before (Figure 3-21b) and after (Figure 3-21c) applying an electrostatic potential of 40 V. The geometry of the deflected tube can be modeled using the elasticity theory, providing a potential technique for quantifying the charge distribution on the tube if its Young's modules is known (see Figures 1-2 and 1-3 for details).

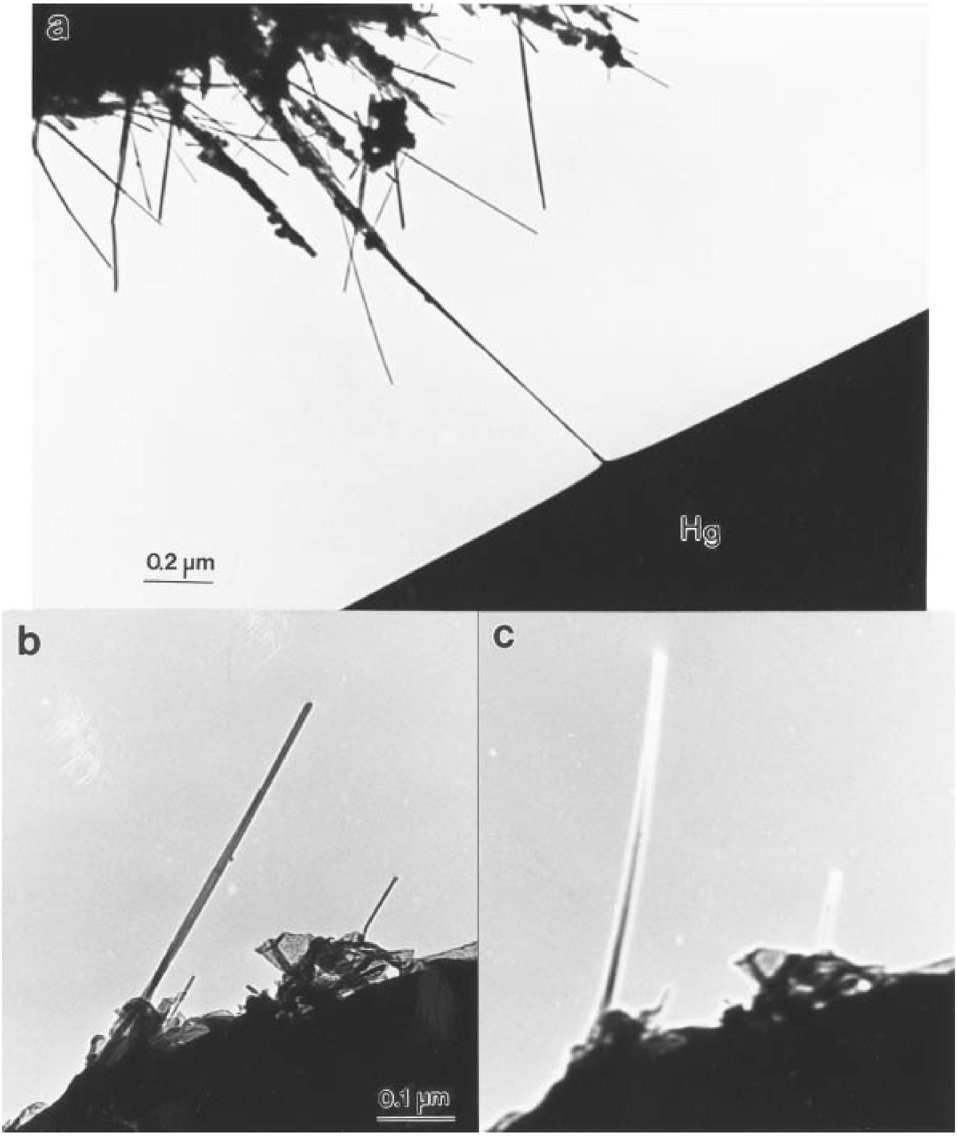

Figure 3-21. (a) TEM image recorded in-situ when a carbon nanotube at the tip of a carbon fiber is in contact with a mercury drop, while an electric current flows through. TEM images of carbon nanotubes recorded at a large defocus condition (b) before and (c) after an electrostatic potential of 40 V is applied across the electrodes. The bright contrast at the tips of the tubes is due to the charging up effect.

3.6 Electron energy-loss spectroscopy of nanoparticles

HRTEM is a powerful technique for identifying the crystal structure of nanophase materials, but it may not be sensitive enough to detect a small change in atomic number. To precisely determine the content of a particular element in a specimen, one must know the characteristics of the atoms. The structure of an atom is usually charac-

terized by the quantized energy levels and the associated electronic states. Under the impact of an incident electron, the electrons bounded to the atoms may be excited either to a free electron state or to a unoccupied energy level with a higher energy. The quantum transitions associated with these excitations will emit photons (or x-rays) and electrons such as secondary electrons, Auger electrons and ionized electrons, these inelastic scattering signals are the finger prints of the elements that can provide quantitative chemical and electronic structural information.

Figure 3-22 shows the main inelastic processes that may be excited in high-energy electron scattering [6, 43]. When a fast electron passes through a thin metal foil, the most noticeable energy-loss is to plasmon oscillations in the sea of conduction electrons. For an ideal case in which the electrons can move "freely" in the sea, the system can be treated as an electron gas. This case is best represented by aluminum, in which the outer-shell electrons can be considered as free electrons. The negatively charged particles are mixed with nuclei, forming a solid state plasmon "gas". The resonance frequency of this *plasmon* is directly related to the density of electrons in the solid. The decay of plasmons results in the emission of *ultraviolet light*. The *cathodulumines-cence* (C.L.) technique is based on the detection of the visible light, which is emitted when an electron in a higher-energy state (usually at an impurity) fills a hole in a lower state that has been created by the fast electron.

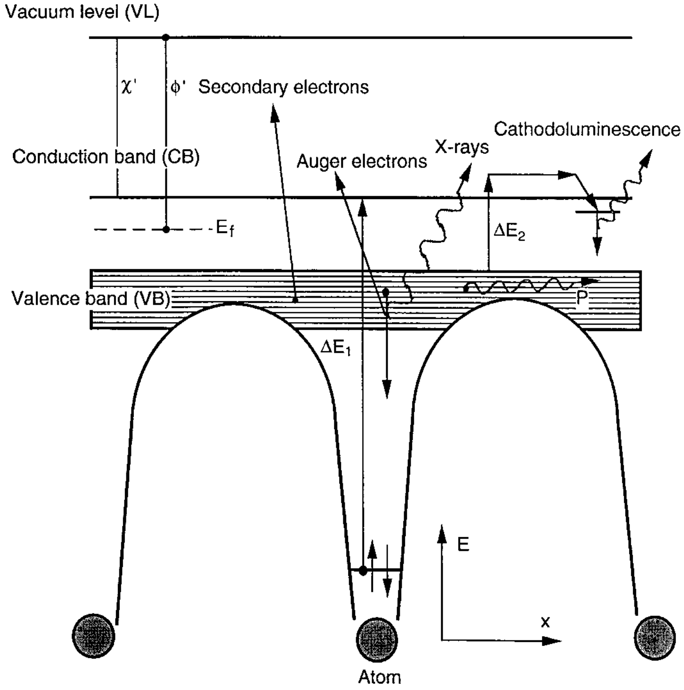

Figure 3-22. Schematic one-electron energy level diagram plotted against the positions of atoms showing the characteristics excitations by an incident electron in a semiconductor material. Here, E_f is the Fermi level, E_b the binding energy, and C.B., V.B. and V.L. are the conduction-band minimum, valance-band maximum, and vacuum level, respectively. ΔE_1 a K shell excitation; ΔE_2 a single-electron excitation; C.L. cathodoluminescence photon; P a plasmon.

Second, *atomic inner-shell ionization* is excited by the energy transfer of the incident electrons, resulting in an ejected electron from a deep-core state (Figure 3-23a). Since only one inner-shell electron is involved in the excitation, this process is also called *single-electron excitation*. The excitation introduces an energy-loss in the range of a few tens to thousands eV which is the finger print of the element. Since the intensity and threshold energy of the inner shell electron transition are determined not only by the binding energy of the atom but also by the density of states in the valence band, the energy-loss near edge structure usually carries some solid state effects, and this is the basis of analyzing the valence states of an element. Analogous to C.L., the holes created at deep core states tend to be filled by the core-shell electrons from higher energy levels, the energy is released in the form of photons (or x-rays) (Figure 3-23b). The energies of the emitted x-rays are quantized and they are fingerprints of the corresponding elements and are used for chemical microanalysis. The holes, created by the ionization process, in deep-core states may alternatively be filled by the electrons from outer shells, the energy released in this process may ionize another outer shell electron (Figure 3-23c), resulting in the emission of *Auger electrons*. Accompanying to these processes, *second electrons* can be emitted from the valence band. The difference between Figures 3-23b and 3-23c is the emission of photon in the former and the Auger electron in the latter, and the two processes are complimentary.

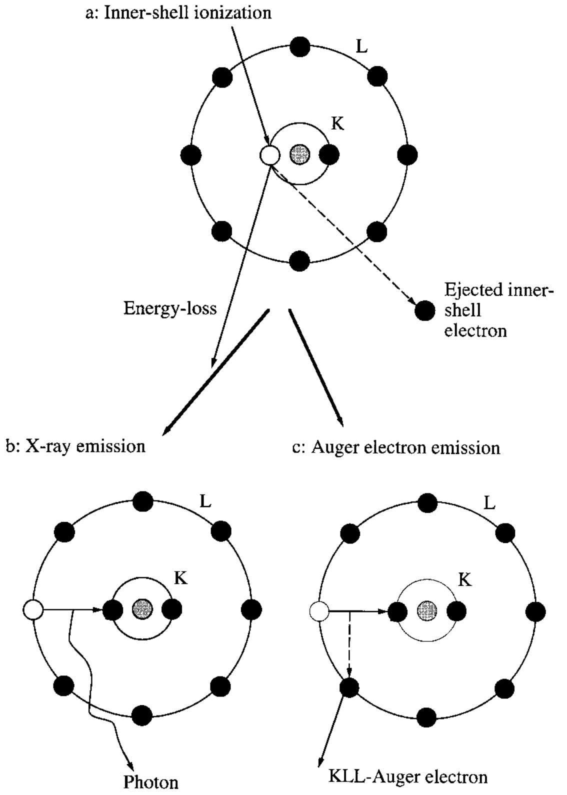

Figure 3-23. (a) Ionization of an atom bounded inner-shell electron by an incident electron, resulting in (b) X-ray emission and (c) Auger electron emission (see text).

In other words, the elements with higher Auger electron yields have lower x-ray emission, and vice versa. Thus, the Auger electron spectroscopy is more sensitive to light elements while EDS is to heavier elements.

The last characteristic inelastic excitation is *phonon scattering* (or *thermal diffuse scattering*, TDS) [44], which is the result of atomic vibrations in crystals. This process does not introduce significant energy-loss but produces large momentum transfers, which can scatter the incident electron into a high angular range. This is a localized inelastic scattering process. As will be shown in Chapter 4 the collection of TDS electrons can produce compositional sensitive images.

3.6.1 Valence excitation spectroscopy

In studying of nanoparticles, it is necessary to probe the electronic structure of a single nanocrystal. This is possible only with the use of a probe that is smaller than the size of the nanocrystal. The valence excitation spectrum of a nanoparticle is most sensitive to its electronic structure and size effects [45, 46]. The spectra can be acquired in TEM and STEM using a fine electron probe. The quantification of the spectra relies on theoretical calculation. The valence band excitation of a nanoparticle is most easily and accurately described using the dielectric response theory. The impact of an incident electron is equivalent to a time-dependent pulse, which causes transitions of valence electrons. In classical dielectric response theory, an incident electron is treated as a particle following a pre-defined trajectory, which is assumed not being affected by the interaction between the incident electron and the dielectric media, as shown in Figure 3-24. Electron energy-loss is a continuous process, in which the electron is decelerated due to the attractive force $F_z = (-\,e)E_z$ owing to the field of the induced charges, resulting in energy-loss. For a general case in which the incident electron is moving along the z-axis and under non-relativistic approximation, if the instantaneous position of the electron is denoted by $\mathbf{r}_0 = (x_0, 0, z'=vt)$, where x_0 is called the impact parameter, the energy-loss spectrum of an incidence electron due to surface plasmon excitation of a finite dielectric medium is calculated by [45, 47]

$$\frac{dP(\omega)}{d\omega} = \frac{e}{\pi\hbar v^2}\int_{-\infty}^{\infty} dz' \int_{-\infty}^{\infty} dz\, \omega \mathrm{Im}\{-\exp\,[i\omega(z'-z)/v]\; V_i(\mathbf{r},\mathbf{r}_0)\}\Big|_{\mathbf{r}=(x_0,0,z),\ \mathbf{r}_0=(x_0,0,z')} \tag{3-12}$$

where $Vi(\mathbf{r},\mathbf{r}_0)$ is the potential due to the induced charge when a "stationary" electron is located at $\mathbf{r}_0 = (x_0, 0, z')$, i.e., it is the homogeneous component of V satisfying

$$\nabla^2 V(\mathbf{r},\mathbf{r}_0) = -\frac{e}{\varepsilon(\omega)\varepsilon_0}\,\delta(\mathbf{r}-\mathbf{r}_0) \tag{3-13}$$

for the dielectric media considered. It is important to note that $Vi(\mathbf{r},\mathbf{r}_0)$ is ω-dependent. The potential distribution in space is a quasi-electrostatic potential for each point along the trajectory of the incident electron. The integral over z' is to sum over the contributions made by all of the points along the trajectory of the incident electron. Therefore, the calculation of valence-loss spectra is actually to find the solution of the electrostatic potential for a stationary electron located at $\mathbf{r}_0$ in the dielectric media system. We now use a spherical particle as an example to illustrate the application of this theory.

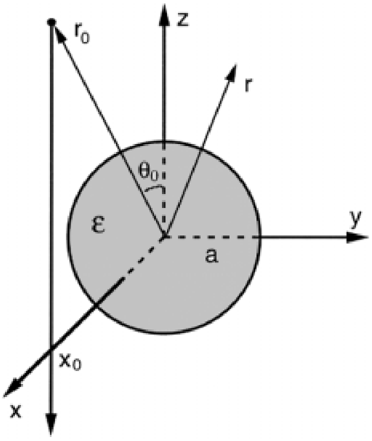

Figure 3-24. Excitation of a spherical particle by an external incident electron with an impact parameter of x_0 ($x_0 > a$). The radius of the sphere is a and its dielectric function is $\varepsilon(\omega)$.

Consider a point electron moving at a constant velocity **v** in vacuum along a trajectory specified by $\mathbf{r}_0 = (x_0, 0, z')$, as schematically shown in Figure 3-24. For simplicity one assumes that the electron does not penetrate the particle. In terms of spherical coordinates (r,θ,ϕ), $r = (x_0^2 + z^2)^{1/2}$, $\cos\theta = z/r$, $r_0 = (x_0^2 + z'^2)^{1/2}$ and $\cos\theta_0 = z'/r_0$. The potential due to the incident electron in free-space for $r_0 > r$ is

$$V_e(\mathbf{r},\mathbf{r}_0) = -\frac{e}{4\pi\varepsilon_0|\mathbf{r}-\mathbf{r}_0|} = -\frac{e}{4\pi\varepsilon_0 r_0}\sum_{L=0}^{\infty}\sum_{m=0}^{L} N_{Lm}\,(r/r_0)^L\,P_{Lm}(\cos\theta)\,P_{Lm}(\cos\theta_0)\cos(m\phi) \tag{3-14a}$$

where P_{Lm} is the associated Legendre function and

$$N_{Lm} = \frac{(2-\delta_{0m})(L-m)!}{(L+m)!} \tag{3-14b}$$

where δ_{0m} is unity if $m = 0$ and is zero otherwise. If $r > r_0$, then r and r_0 are exchanged in Eq. (3.149). The solution of Eq. (3-13) consists of the field by the free point charge and the induced charge. The potential outside the sphere has a form of

$$V_{out}(\mathbf{r},\mathbf{r}_0) = V_e(\mathbf{r},\mathbf{r}_0) - \frac{e}{4\pi\varepsilon_0}\sum_{L=0}^{\infty}\sum_{m=0}^{L} A_{Lm}\,\frac{1}{r}\,(a/r)^{L+1}\,P_{Lm}(\cos\theta)\,P_{Lm}(\cos\theta_0)\cos(m\phi) \tag{3-15}$$

and inside the sphere the potential is

$$V_{in}(\mathbf{r},\mathbf{r}_0) = -\frac{e}{4\pi\varepsilon_0 a}\sum_{L=0}^{\infty}\sum_{m=0}^{L} B_{Lm}\,(r/a)^L\,P_{Lm}(\cos\theta)\,P_{Lm}(\cos\theta_0)\cos(m\phi) \tag{3-16}$$

Matching boundary conditions:

$$V_{out}(\mathbf{r},\mathbf{r}_0)|_{r=a} = V_{in}(\mathbf{r},\mathbf{r}_0)|_{r=a}, \text{ and } \frac{\partial V_{out}(\mathbf{r},\mathbf{r}_0)}{\partial r}\Big|_{r=a} = \varepsilon(\omega)\,\frac{\partial V_{in}(\mathbf{r},\mathbf{r}_0)}{\partial r}\Big|_{r=a} \tag{3-17}$$

the A_{Lm} and B_{Lm} coefficients are determined to be:

$$A_{Lm} = N_{Lm}\frac{L(1-\varepsilon)}{L\varepsilon+L+1}(a/r_0)^{L+1}, \text{ and } B_{Lm} = N_{Lm}\frac{2L+1}{L\varepsilon+L+1}(a/r_0)^{L+1} \quad (3\text{-}18)$$

Substituting Eq. (3-15) into (3-14), performing the analytical integral with the use of an identity

$$\int_{-\infty}^{\infty} dt\, r_0^{-(L+1)} P_{Lm}(\cos\theta_0)\exp(i\omega t) = \frac{2i^{L-m}|\omega/v|^{L} K_m(|\omega x_0/v|)}{v(L-m)!}(\omega/|\omega|)^{L-m} \quad (3\text{-}19)$$

the spectrum is given by

$$\frac{dP}{d\omega} = \frac{e^2 a}{\pi^2 \varepsilon_0 \hbar v^2}\sum_{L=0}^{\infty}\sum_{m=0}^{L} M_{Lm}[K_m(\omega x_0/v)]^2(\omega a/v)^{2L}\,\mathrm{Im}\left[\frac{L(\varepsilon(\omega)-1)}{L(\varepsilon(\omega)+L+1}\right] \quad (3\text{-}20a)$$

where

$$M_{Lm} = \frac{(2-\delta_{0m})}{(L-m)!(L+m)!} \quad (3\text{-}20b)$$

From the energy-loss function, the resonance free frequencies of the surface plasmons are determined by [50]

$$L\varepsilon(\omega) + L + 1 = 0 \quad (3\text{-}21)$$

The homogeneous medium theory has been extended recently for the cases of anisotropic dielectric medium, such as carbon onion structure and carbon nanotubes [48, 49]. Shown in Figure 3-25a are a group of calculated EELS spectra for a carbon onion

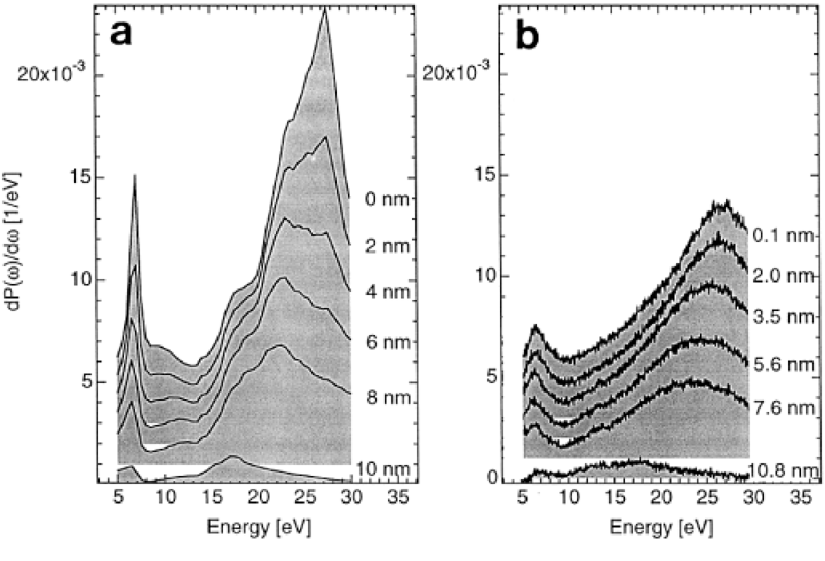

Figure 3-25. (a) Calculated EELS spectra of a carbon sphere (radius = 10 nm) with graphitic onion-like structure as a function of the electron impact parameter x_0. (b) Experimentally observed EELS spectra from a carbon sphere (Courtesy of T. Stöckli).

of radius 10 nm as a function of the electron impact parameter. The calculation has to consider the anisotropic dielectric properties of the graphitic onion-like structure. At small impact parameters, the excitation is dominated by volume plasmon, and at larger impact parameters, the surface excitation becomes dominant. When the electron probe is outside of the sphere, the entire spectrum is the surface excitation. This type of calculation gives quantitative agreement with experimental observations (Figure 3-25b) and it can be used to quantify the dielectric properties of a single nanostructure.

3.6.2 Quantitative nanoanalysis

Energy dispersive x-ray spectroscopy (EDS) and electron energy-loss spectroscopy (EELS) in TEM have been demonstrated as powerful techniques for performing microanalysis and studying the electronic structure of materials [43]. Atomic inner shell excitations are often seen in EELS spectra due to a process in which an atom-bounded electron is excited from an inner shell state to a valence state accompanied by incident electron energy loss and momentum transfer. This is a localized inelastic scattering process, which occurs only when the incident electrons are propagating in the crystal. Figure 3-26 shows an EELS spectrum acquired from $YBa_2Cu_4O_8$. Since the inner-shell energy levels are the unique features of the atom, the intensities of the ionization edges can be used effectively to analyze the chemistry of the specimen.

After subtracting the background, an integration is made to the ionization edge for an energy window of width Δ accounted from the threshold energy. Thus, the intensity oscillation at the near edge region is flattered, and the integrated intensity is dominated by the properties of single atoms. This type of information is most useful in material analysis and the integrated intensity is given by

$$I_A(\Delta) \approx I_0(\Delta)\, \sigma_A(\Delta,\beta)\, n_A\, d \tag{3-22}$$

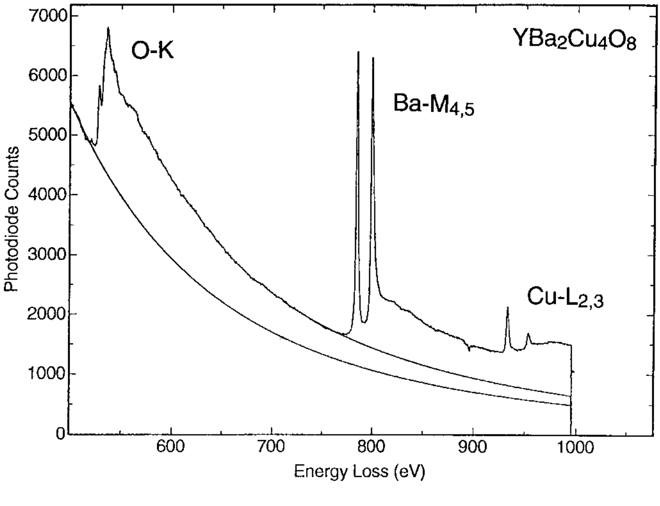

Figure 3-26. An EELS spectrum acquired from $YBa_2Cu_4O_8$ showing the application of EELS for quantitative chemical microanalysis, where the smooth lines are the theoretically simulated background to be subtracted from the ionization regions.

where $I_0(\Delta)$ is the integrated intensity of the low-loss region including the zero-loss peak for an energy window Δ; $\sigma_A(\Delta,\beta)$ is the energy and angular integrated ionization cross-section. In imaging mode, β is mainly determined by the size of the objective aperture or the upper cut-off angle depending on which is smaller. In diffraction mode, the β angle is determined not only by the size of the EELS entrance aperture and the camera length but also by the beam convergence. In general, the width of the energy window is required to be more than 50 eV to ensure the validity of Eq. (3-21), and Δ = 100 eV is an optimum choice. If the ionization edges of two elements are observed in the same spectrum, the chemical composition of the specimen is

$$\frac{n_A}{n_B} = \frac{I_A(\Delta)}{I_B(\Delta)} \frac{\sigma_B(\Delta,\beta)}{\sigma_A(\Delta,\beta)} \tag{3-23}$$

This is the most powerful application of EELS because the spatial resolution is almost entirely determined by the size of the electron probe. The key quantity in this analysis is the ionization cross-section. For elements with atomic numbers smaller than 14, the K edge ionization cross-section can be calculated using the SIGMAK program [43], in which the atomic wave function is approximated by a single-electron hydrogen-like model. The ionization cross-section for elements with $13 < Z < 28$ can be calculated using the SIGMAL program. For a general case, the ionization cross-section may need to be measured experimentally using a standard specimen with known chemical composition.

3.6.3 Near edge fine structure and bonding in transition metal oxides

The energy-loss near edge structure (ELNES) is sensitive to the crystal structure. This is a unique characteristics of EELS and in some cases it can serve as a "fingerprint" to identify a compound. A typical example is the intensity variation in the π^* and σ^* peaks observed in the C-K edge, as shown in Figure 3-27. Diamond is almost completely dominated by the σ^* bonding, while the π bonding appears in graphite and

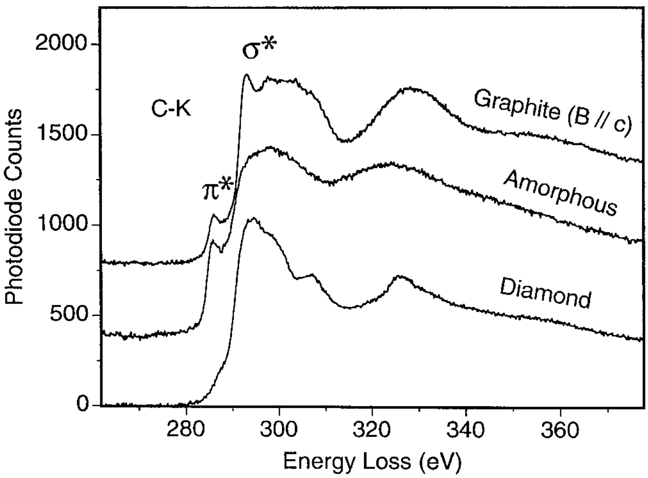

Figure 3-27. EELS C-K edge spectra acquired from diamond, amorphous carbon and graphite, respectively, showing the sensitivity of EELS to bonding in carbon related materials.

amorphous carbon. The disappearance of the π* peak in C-K edge can be uniquely used to identify the presence of diamond bonding in a carbon compound. It must be pointed out that the spectrum for graphite shown here was acquired when the incident beam parallel to the c-axis. If a small size aperture is used, only a small portion of electrons corresponding to the π* peak is collected.

In EELS, the L ionization edges of transition-metal and rare-earth elements usually display sharp peaks at the near edge region (Figure 3-28), which are known as *white lines.* For transition metals with unoccupied 3d states, the transition of an electron from 2p state to 3d levels leads to the formation of white lines. The L_3 and L_2 lines are the transitions from $2p^{3/2}$ to $3d^{3/2}3d^{5/2}$ and from $2p^{1/2}$ to $3d^{3/2}$, respectively, and their intensities are related to the unoccupied states in the 3d bands. Numerous EELS experiments have shown that a change in valence state of cations introduces a dramatic change in the ratio of the white lines, leading to the possibility of identifying the occupation number of 3d orbital using EELS.

EELS analysis of valence state is carried out in reference to the spectra acquired from standard specimens with known cation valence states. Since the intensity ratio of L_3/L_2 is sensitive to the valence state of the corresponding element, if a series of EELS spectra are acquired from several standard specimens with known valence states, an empirical plot of these data serves as the reference for determining the valence state of the element present in a new compound [51–59]. The L_3/L_2 ratios for a few standard Co compounds are plotted in Figure 3-29a. EELS spectra of Co-$L_{2,3}$ ionization edges were acquired from $CoSi_2$ (with Co^{4+}), Co_3O_4 (with $Co^{2.67}+$), $CoCO_3$ (with Co^{2+}) and $CoSO_4$ (with Co^{2+}). Figure 3-29b shows a plot of the experimentally measured intensity ratios of white lines L_3/L_2 for Mn. The curves clearly show that the ratio of L_3/L_2 is very sensitive to the valence state of Co and Mn. This is the basis of our experimental approach for measuring the valence states of Co or Mn in a new material.

Determination the crystal structure of nanoparticles is a challenge particularly when the particles are smaller than 5 nm. The intensity maxim observed in the x-ray or electron diffraction patterns of such small particles are broadened due to the crystal shape factor, greatly reduced the accuracy of structure refinement. The quality of the

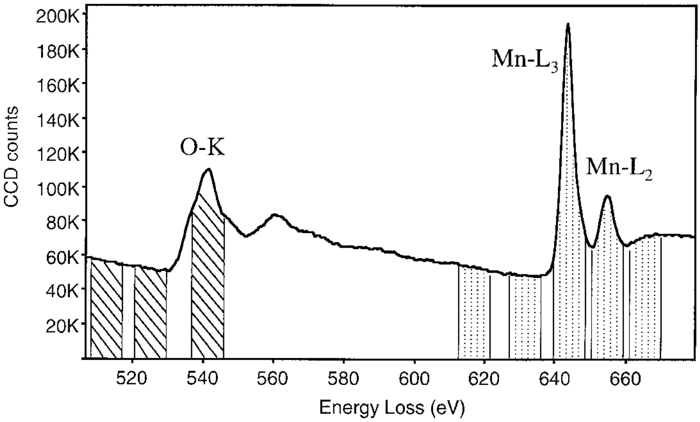

Figure 3-28. EELS spectrum acquired from MnO_2 showing the Mn-L_3 and Mn-L_3 white lines. The five windows pasted in the Mn-L edge are to be used for extracting the image formed by the ratio of white lines.

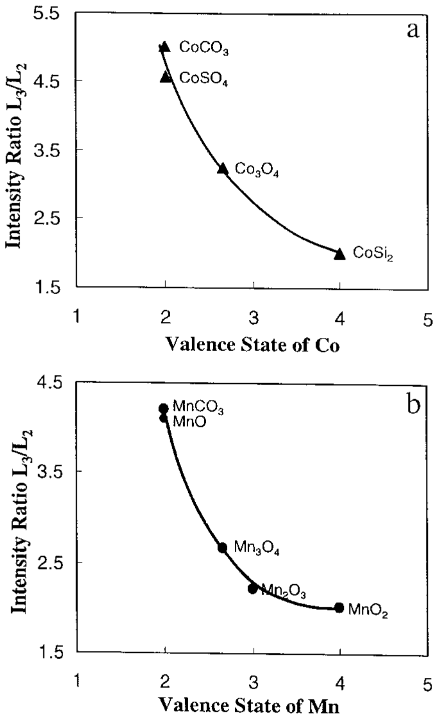

Figure 3-29. Plots of the intensity ratios of L_3/L_2 calculated from the spectra acquired from (a) Co compounds and (b) Mn compounds as a function of the cation valence. A nominal fit of the experimental data is shown by a solid curve.

high-resolution TEM images of the particles is degraded because of the strong effect from the substrate. This difficulty arises in our recent study of CoO nanocrystals whose shape is dominated by tetrahedral of sizes smaller than 5 nm [60]. Electron diffraction indicates the crystal has a fcc-type cubic structure. To confirm the synthesized nanocrystals are CoO, EELS is used to measure the valence state of Co. Figure 3-30

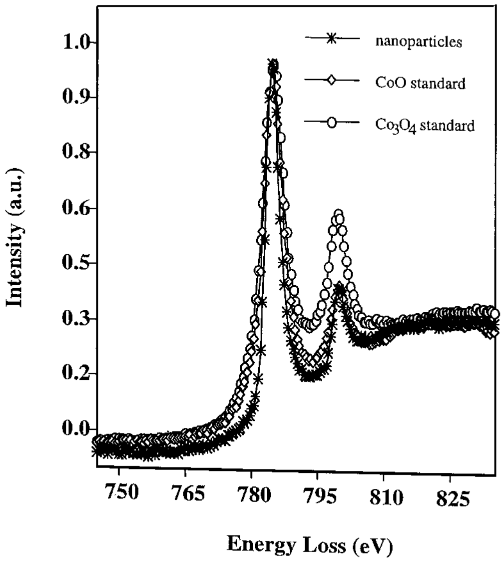

Figure 3-30. A comparison of EELS spectra of $Co\text{-}L_{2,3}$ ionization edges acquired from Co_3O_4 and CoO standard specimens and the synthesized nanocrystals, proving that the valence state of Co is 2+ in the nanocrystals. The full width at half maximum of the white lines for the Co_3O_4 and CoO standards is wider than that for the nanocrystals, possibly due to size effect.

shows a comparison of the spectra acquired from Co_3O_4 and CoO standard specimens and the synthesized nanocrystals. The relative intensity of the Co-L_2 to Co-L_3 for the nanocrystals is almost identical to that for CoO standard, while the Co-L_2 line of Co_3O_4 is significantly higher, indicating that the Co valence in the nanocrystals is 2+, confirmed the CoO structure of the nanocrystals.

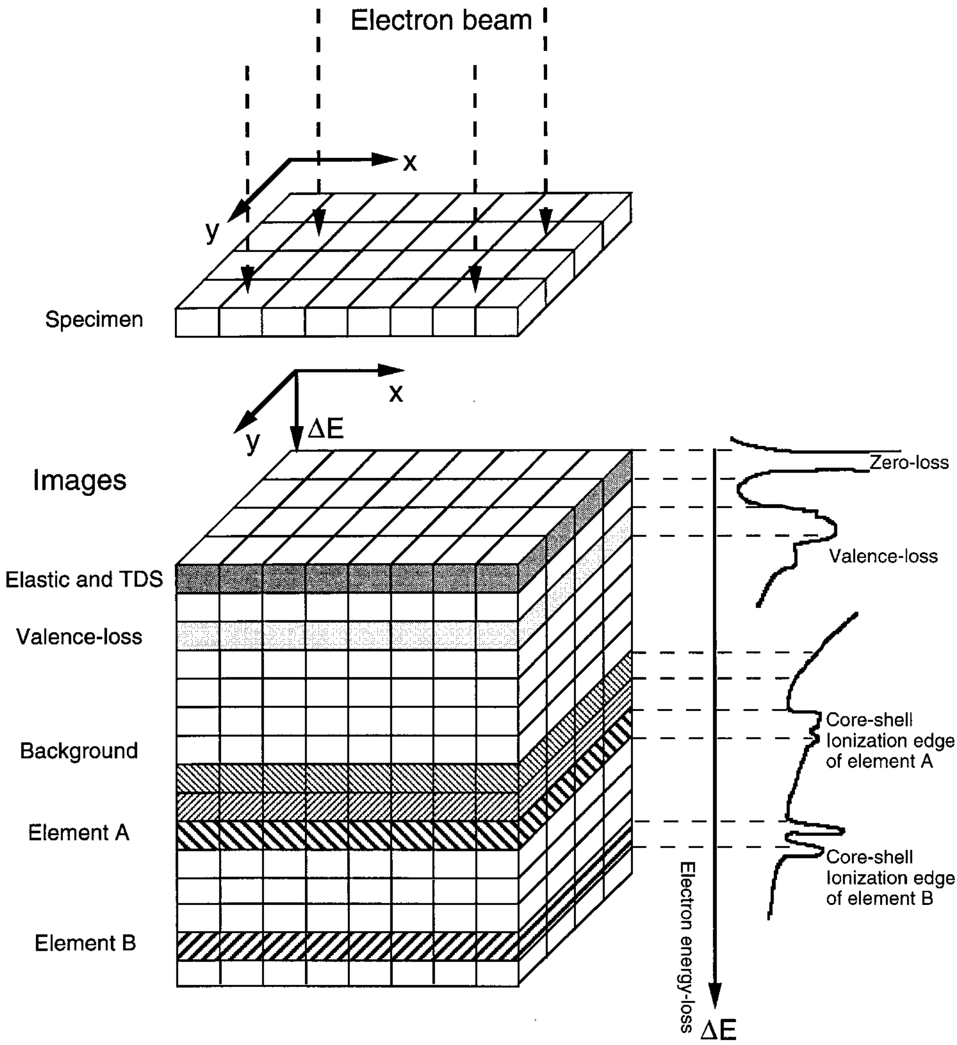

Figure 3-31. A schematic diagram showing energy-filtered electron imaging in TEM. The conventional TEM image is recorded by integrating the electrons with different energy losses. The energy-selected electron images corresponding to different characteristic energy-loss features are shown, which can be used to extract useful structural and chemical information of the specimen.

3.7 Energy-filtered electron imaging

3.7.1 Energy filtering in TEM

Energy-filtered transmission electron microscopy (EF-TEM) is a rapid developing field for high spatial-resolution chemical imaging. With an energy-filter, images (or diffraction patterns) formed by electrons with specific energy-losses can be obtained (see Figure 3-31) [61]. The energy-selected electron images can be simply illustrated using a 3-D data space, in which the z-axis is replaced by the energy-loss of the electrons, and x and y are the real space coordinates of the 2-D image of the specimen. All the inelastic scattering processes introduced above are observed in the EELS spectrum, as schematically shown on the right-hand side of Figure 3-31. The zero-loss (or 0-loss) peak is composed of elastically and thermal diffusely scattered electrons. The images/diffraction patterns produced by the elastically scattered and by thermal diffusely scattered electrons are incoherent. The low-loss region is dominated by valence excitations. However, as was discussed previously, the energy-selected image of valence-loss (or plasmon-loss for metals) electrons is not strongly composition sensitive because their scattering is closely related to the valence-band structure of the material. Atomic inner-shell ionization edges can be employed to form composition-sensitive images. The background observed in the EELS spectrum is produced by scattering processes of multiple valence losses, electromagnetic radiation and electron Compton scattering. In order to extract composition-sensitive images, the contribution made by these processes must be subtracted from the recorded data.

3.7.2 Composition-sensitive imaging using inner-shell ionization edges

Energy-selected electron images of atomic inner-shell ionization edges can also be performed in STEM [62, 63]. The image is formed by processing the EELS spectra acquired at each beam position, so that the thickness integrated elemental map is

$$n_A\, d = \frac{1}{\sigma_A(\Delta,\beta)} \frac{I_A(\Delta)}{I_0(\Delta)} \tag{3-24}$$

Figure 3-32 gives a pair of energy-filtered TEM images using the C-K and Ag-L edges, respectively, from a specimen of Ag nanocrystals passivated with $SC_{12}H_{25}$ thiolate chains. The carbon distribution represents the local thickness-projected density of the adsorbed molecules. In the region with less Ag particles, the stronger carbon signal indicates the accumulation of the molecules. The image using Ag-L edge clearly shows the distribution of Ag cores. Energy-filtered image using the O-K edge proves that the particles are not oxidized.

3.7.3 Mapping the bonding and valence state using fine edge structures

If the energy-selected electron image can be formed using the fine features at the near edge region, one can map the spatial distribution of the valence states. The most typical example of mapping the valence state distribution is the case of using the σ^* and π^* peaks observed in C-K edge of diamond specimens [64, 65]. Here we illustrate a new approach that can map the distribution of the valence states of transition metal

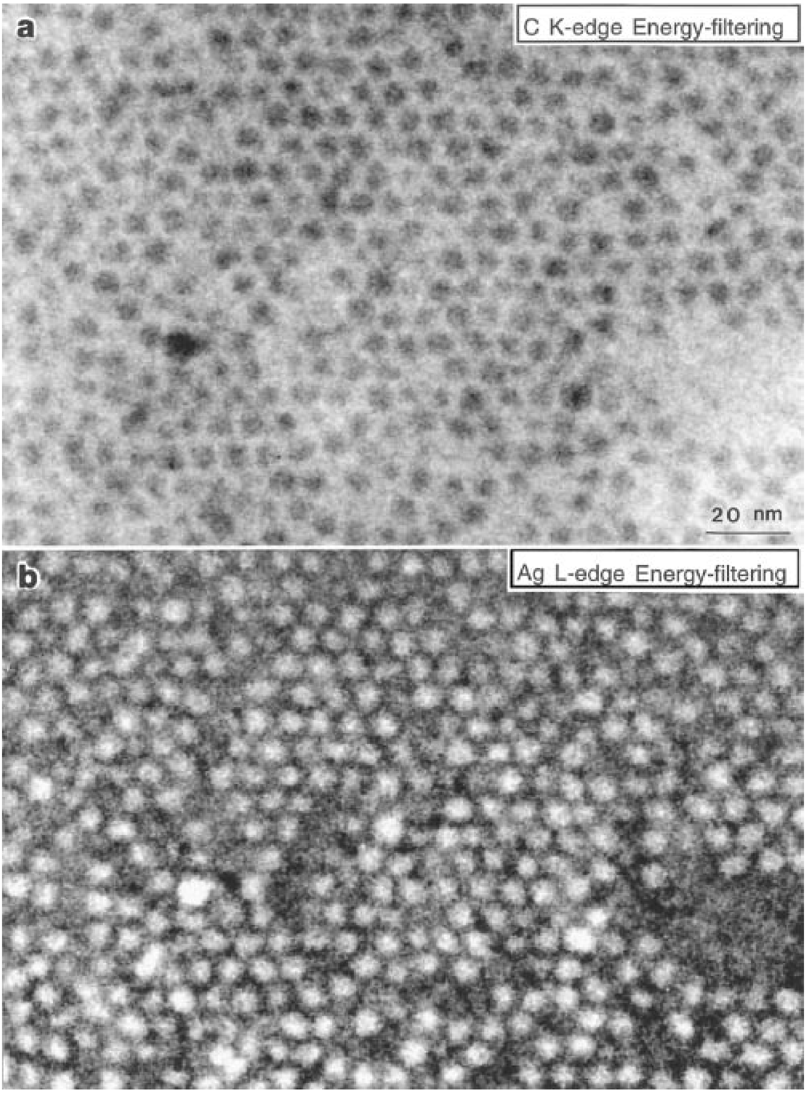

Figure 3-32. Energy-filtered TEM images recorded using (a) the C-K edge and (b) the Ag-L edge from a specimen of Ag nanocrystals passivated with $SC_{12}H_{25}$ molecules and dispersed on an amorphous silica substrate. The energy window width was 20 eV.

elements in oxides [66]. In EF-TEM, an energy window of 12 eV in width is required to isolate the L_3 from L_2 white lines (Figure 3-28). A five-window technique is introduced: two images are acquired at the energy-losses prior to the L ionization edges, and they are to be used to subtract the background for the characteristic L edge signals; two images are acquired from the L_3 and L_2 white lines, respectively, and the fifth image is recorded using the electrons right after the L_2 line that will be used to subtract the continuous background underneath the L_3 and L_2 lines. Then, a L_3/L_2

ratio image will be obtained, which reflects the distribution of valence state across the specimen. It must be pointed out that the thickness effect has been removed in the L_3/L_2 image.

A partially oxidized CoO specimen that contains CoO and Co_3O_4 grain structure was chosen for this study [67]. The CoO and Co_3O_4 phases are separated by clear boundaries and it is an ideal specimen for testing the optimum resolution. Figure 3-33 shows a group of energy-filtered TEM image from a triple point in the CoO-Co_3O_4 specimen. The energy-filtered images using the L_3 and L_2 lines and the post L_2 line region (Figures 3-33a-c) show distinctly difference in contrast distribution due to a difference in the relative white line intensities. From these three images the L_3/L_2 is calculated after subtracting the contribution from the continuous energy-loss region that is due to single atom scattering, and the image clearly displays the distribution of cobalt oxides having different valence states (Figure 3-33e), where the diffraction contrast disappears. The region with lower oxidation state (Co2+) shows stronger contrast, and the ones with high oxidation states show darker contrast (see the L_3/L_2 ratio displayed in Figure 3-29a). The O/Co image was calculated from the images recorded from the O-K edge and the $L_3 + L_2$ white lines for an energy window width of $\Delta = 24$ eV. Although the energy-filtered O-K edge image exhibit some diffraction contrast and the thickness effect, the O/Co compositional ratio image greatly reduces the effect. The high intensity region in the O/Co image indicates the relative high local concentration in oxygen (e.g., higher Co oxidation states), the low intensity region contain relatively less oxygen (e.g., lower Co valence state), entirely consistent with the information provided by the L_3/L_2 image. A spatial resolution of ~ 2 nm has been achieved. This is remarkable in comparison to any existing techniques.

3.7.4 Energy dispersive x-ray microanalysis (EDS)

X-rays emitted from atoms represent the characteristics of the elements and their intensity distribution represents the thickness-projected atom densities in the specimen. This is the energy dispersive x-ray spectroscopy (EDS) which has played an important role in microanalysis, particularly for heavier elements [68]. EDS is a key tool for identifying the chemical composition of a specimen. A modern TEM is capable of producing a fine electron probe of smaller than 2 nm, allowing direct identification the local composition of an individual nanocrystal. Details of this type of analysis will be give in Section 3.8.2.

3.8 Structure of self-assembled nanocrystal superlattices

Nanoparticles and the physical and chemical functional specificity and selectivity they possess, suggest them as ideal building blocks for two- and three-dimensional cluster self-assembled superlattice structures, in which the particles behave as well-defined molecular matter and they are arranged with long-range translational and even orientational order. Research has successfully fabricated *self-assembly passivated nanocrystal superlattices (NCS's) or nanocrystal arrays (NCA)* of metal, semiconductor and oxide clusters [35, 60, 69–74], which are a new form of materials with fundamental interests and technological importance. Self-assembled arrays involve self-organization into monolayers, thin films, and superlattices of size-selected nanoclus-

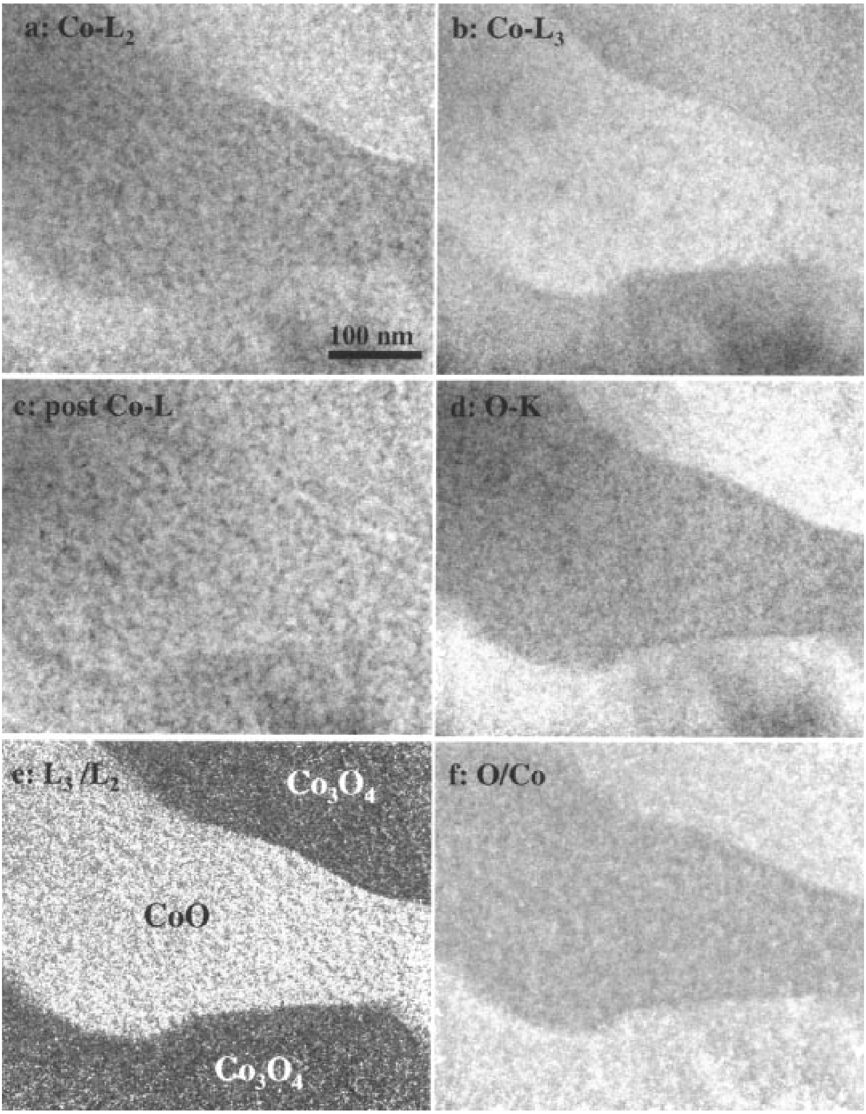

Figure 3-33. A group of images recorded from the same specimen region using signals of (a) the Co-L_3 edge, (b) the Co-L_2 edge, (c) the post Co-L_2 line, and (d) the O-K edge. (e) The processed L_3/L_2 image, displaying the distribution of the valence states. (f) The atomic concentration ratio image of O/Co. The continuous background contributed from the single atom scattering has been removed from the displayed Co-L_3 and Co-L_2 images. The O/Co image is normalized in reference to the standard composition of CoO for the low portion of the image in order to eliminate the strong influence on the ionization cross-section from the white lines. Each raw image was acquired with an energy window width of $\Delta = 12$ eV except for O-K at $\Delta = 24$ eV.

ters encapsulated in protective compact organic coating. By changing the length of the molecular chains, quantum transitions and insulator to conductor transition could be introduced, resulting in tunable electronic, optical and transport properties.

NCS's are characterized by unprecedented size-uniformity and translation and even orientation order, created through a multistage processing strategy involving self-assembly, annealing, etching of defects, reversible passivation by self-assembled monolayers, and macroscopic separation by size of the resulting assemblies. Particles that can be self-assembled usually have sizes smaller than 10 nm, it is in this size range that many exciting and unusual physical properties are enhanced. The nanocrystals are passivated by a monolayer of long-chain organic molecules, such as SR, where R = n–C_nH_{2n+1}, n = 4, 6, 8, 12…, called thiolates. The thiolate serves not only as the protection for the particles to avoid direct contact between the particles with a consequence of coalescing, but also the interparticle bonding.

3.8.1 Particle shape and assembling crystallography

If the nanocrystals can be taken as the building blocks, their 3-D assembling is unavoidably affected by the particle shape. In this section, the self-assembling of truncated octahedral Ag nanocrystals is taken as an example to illustrate the roles played by the particle shape in NCSs [2, 10]. Our main goal is to illustrate the formation of directional, interparticle molecular bonds by the thiolates. Figure 3-34a is an TEM image recorded from an Ag NCS deposited on a carbon substrate. The Ag nanocrystals have a truncated octahedral shape and they are oriented along the [110] of the Ag atomic lattice in the image, along which four {111} and two {100} facets are imaged edge-on. The unit cell of the NCS is also oriented along $[110]_s$ of *fcc*, where the subscript refers to the supercrystal. Therefore, the orientational relationship between the Ag particles and the nanocrystal lattice is $[110] \parallel [110]_s$ and $[001] \parallel [1\bar{1}0]_s$ (Figure 3-34c) [35, 69]. Accordingly, a structure model for the NCS is built (Figure 3-34d), in which the nanocrystals are oriented following an assembling principle of *face-to-face*.

Silver nanocrystals can also be dominated by icosahedral and decahedral. The spherical-like of these particles results in hexagonal closing packing [70]. The percentage of multiply twinned particle can be directly estimated from dark-field TEM image recorded using a small size objective aperture. Figure 3-35 shows an TEM image of a monolayer assembly of Ag nanocrystals. Many of the particles show double or even triple split contrast, suggesting these particles are not single crystalline, rather they contain twins. The particle would appear uniform in contrast if it is single crystalline. This is a easy method to estimate the population of the twinned particles. NCS's are rather rubust and they are stable to temperatures as high as 600 °C [75, 76].

3.8.2 Interdigitation of molecular bonds in nanocrystal self-assembly

A careful examination of the image shown in Figure 3-34a indicates there are some white spots in the image, corresponding to open channels formed by the thiolate molecules, suggesting that the thiolates are tethered on the faces of the nanocrystals and they are likely to be erected on the surface. The shortest distance between the face-to-face {100} facets of the two adjacent particles is only ~ 1.5 to 2 nm, almost equal to the 1.5 nm chain length of the thiolate molecules used for passivating the Ag nanocrystals. Therefore, the thiolate molecules tethered on the facets of the nanocrystals are likely to interpenetrate, forming the *interdigitative bonds*.

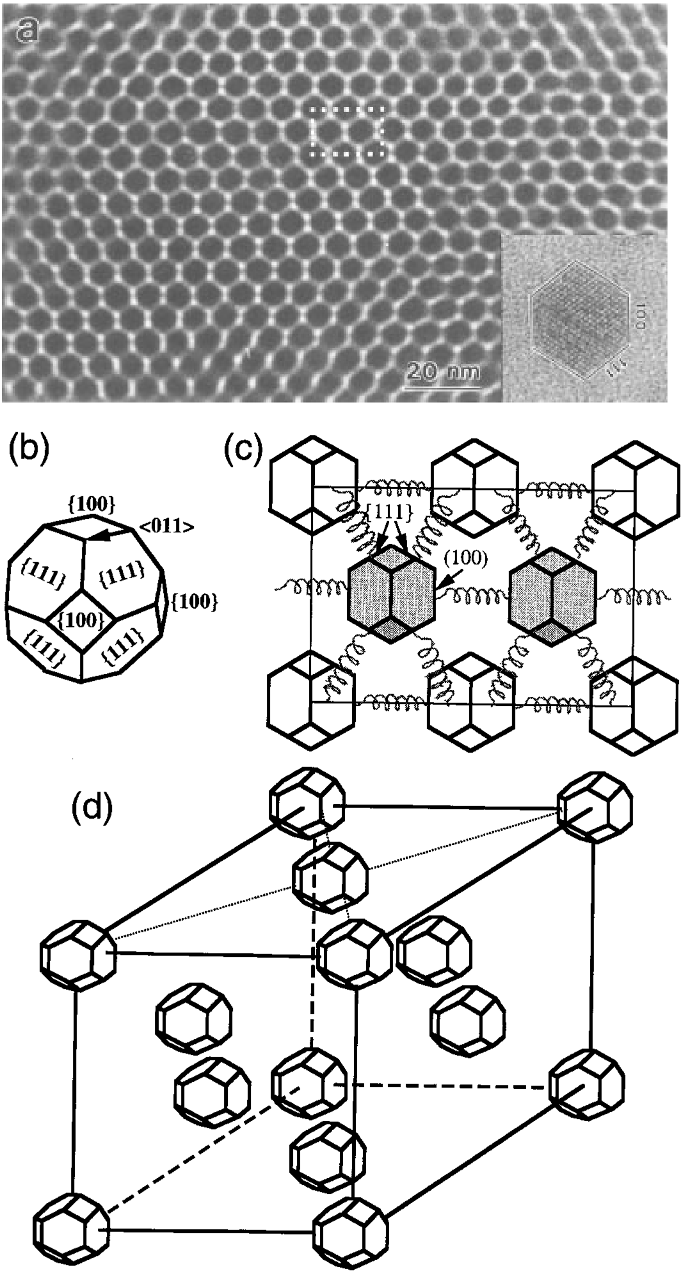

Figure 3-34. (a) TEM image of a face-centered cubic packed Ag nanocrystals whose shape is dominated by truncated octahedral (TO) (see the inset HRTEM image of a single Ag nanocrystal). The image displays the orientational relationship between the nanocrystals and the assembled superlattice. (b) A structural model of the TO particle, (c) the $[110]_s$ projection of the unit cell as indicated in (a), where the grey pasted particles are located at different z heights; and (d) the 3-D structural model of the fcc packing of nanocrystals.

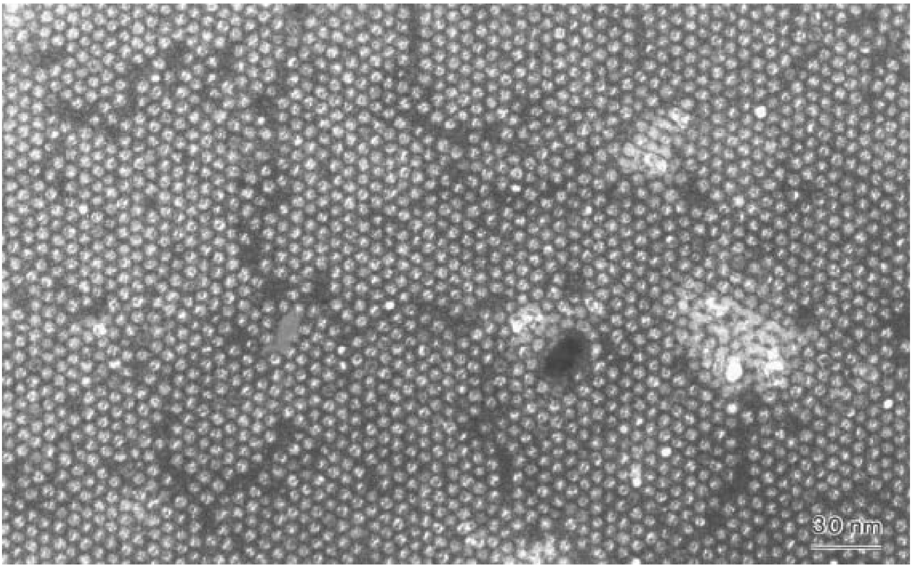

Figure 3-35. A dark-field TEM image recorded from a monolayer self-assembled Ag nanocrystals, showing the multiply split contract across each nanocrystal, and suggesting that the majority of the particles have twin structure.

A direct observation of the thiolates can be provided by the EF-TEM [77]. The thiolate molecules are composed of mainly carbon, thus the EF-TEM of the carbon K edge can give the distribution of the thiolates around the nanocrystals. For this analysis, Ag NCSs are deposited on an amorphous SiO_x substrate and the effects from the substrate can be removed by processing the experimental images acquired pre- and post-edge. The EF-TEM was performed for the Ag NCS oriented along $[110]_s$, which is the optimum orientation for imaging thiolate distribution between the particles. The EF-TEM image acquired using the carbon K edge from a Ag NCS gives an interesting contrast feature (Figure 3-36a). The projected carbon density between the particles shows a contrast pattern that is the strongest between the A and B types of particles, while the contrast is lower between the A and C or B and C types of particles. To interpret this phenomenon, we first construct the $[110]_s$ projection of the NCS based on the 3-D model given in Figure 3-36b, and the result is shown in Figure 3-36b. From the structural point of view, the molecular bonds tend to parallely align the facets on which they are tethered. For the nanocrystals A and B assembled by facing the {100} faces, in addition to the carbon density contributed by the interdigitative thiolates passivated on the {100} facets (which are edge-on while viewed along $[110]_s$), the thiolates passivated on the four {111} planes (not edge-on) also contribute to the projected carbon density although the {111} faces are at an angle with the projection direction. Therefore, the projected density of the thiolate molecules between particles A and B is expected to be higher than that between A and C (or B and C) if the size of {111} faces is the same as the that of {100} as well as the density of the thiolate passivation is the same on both {111} and {100}. With consideration the resolution of the EF-TEM of ~ 2 nm, the channels formed by the bundled thiolates may not be resolved

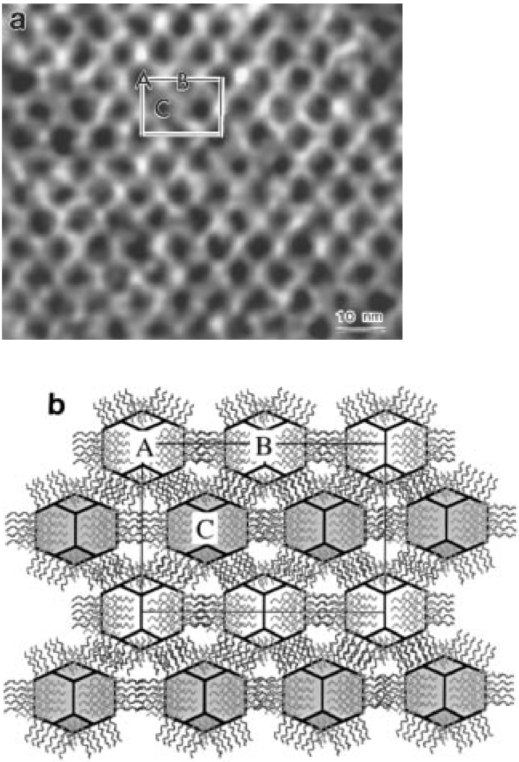

Figure 3-36. (a) Energy filtered TEM image of the Ag nanocrystal assembly using the carbon K ionization edge, showing the projected density of carbon along the $[110]_s$ of the NCS. (b) A model showing the distribution of passivated molecules between the nanocrystals. The projected unit cell is represented by a rectangle.

in this type of images. This result proves that the adsorbed molecules are distributed on the surfaces of the nanocrystals, and they form interdigitative bundling that holds the nanocrystal together.

3.9 Summary

This chapter was concentrated on introduction of TEM and associated techniques for characterization of nanophase materials. The objective was to review the versatility of TEM and the complimentary applications of the techniques. In additional to the high-resolution capability, TEM is also powerful in identifying and quantifying the chemical and electronic structure of nanomaterials. High-spatial resolution analysis is vitally important for solving many of the practical problems of nanomaterials. Spectroscopy analysis of the solid state effects and the valence states mapping are a new direction of quantitative microscopy. Further exploration in the fine structures in EELS is likely to reveal rich information about bonding in crystals and at interfaces. In-situ TEM is anticipated to be important for characterizing and measuring the properties of individual nanostructures, from which the structure-property relationship can be clearly registered to a specific nanoparticle/structure.

Acknowledgment

The author is grateful to his collaborators, M.A. El-Sayed, J.M. Petroski, T. Ahmadi, R.L. Whetten, S.A. Harfenist and I. Vezmar, for kindly provide some of the specimens. Research was partially sponsored by NSF grant DMR-9733160.

References

[1] P. Buseck, J.M. Cowley and L. Eyring eds. *High Resolution Transmission Electron Microscopy and Associated Techniques*, New York, London, Amsterdam, Oxford University Press, **1988**.
[2] J.M. Cowley, *Diffraction Physics*, 3rd revised ed., New York, London, Amsterdam, Elsvier Science B.V., **1995**.
[3] Z.L. Wang, and Z.C. Kang, *Functional and Smart Materials – Structural Evolution and Structure Analysis,* New York, Plenum Press **1998**, Chap. 6.
[4] P.B. Hirsch, A. Howie, R.B. Nicholson, D.W. Pashley and M.J. Whelan, *Electron Microscopy of Thin Crystals*, New York, Roberts E. Krieger Publishing Company, **1977**.
[5] O. Scherzer, *J. Appl. Phys.* **1949**, *20*, 20.
[6] Z.L. Wang, *Elastic and Inelastic Scattering in Electron Diffraction and Imaging,* New York, Plenum Pub. Co., **1995**, Chaps. 2 and 3.
[7] J.M. Cowley and A.F. Moodie, *Acta Cryst.* **1957**, *10*, 609.
[8] J.A. Ascencio, C. Gutiérrez-Wing, M.E. Espinosa, M. Marin, S. Tehuacanero, C. Zorrilla and M. José-Yacamán, *Surf. Sci*. **1998**, *396*, 349.
[9] D.J. Smith and L.D. Marks, *Pil. Mag. A* **1981**, *44*, 735.
[10] M. Yao and D.J. Smith, *J. Microsc.*, **1994**, *175*, 252.
[11] Z.L. Wang, T.S. Ahmadi and M.A. El-Sayed, *Surf. Sci.*, **1996**, *380*, 302.
[12] K. Takayanagi, Y. Tanishiro, M. Takahashi and S. Takahashi, *Surf. Sci*. **1985**, *164*, 367.
[13] L.D. Marks and D.J. Smith, *Nature* **1983**, *303*, 316.
[14] R.G. Linford, *Solid State Surface Science*, ed. M. Green, New York, Dekker **1973**, *2*, 1.
[15] S. Onodera, *J. Phys. Soc. Japan* **1991**, *61*, 2191.
[16] S. Ino, *J. Phys. Soc. Japan,* **1966**, *21*, 346.
[17] J.G. Allpress and J.V. Sanders, *Surf. Sci.*, **1967**, *7*, 1.
[18] L. D. Marks, *Rep. Prog. Phys.*, **1994**, *57*, 603, and the references there in.
[19] C.Y. Yang, *J. Cryst. Growth*, **1979**, *47*, 274; ibid, **1979**, *47*, 283.
[20] P.-A. Buffat, M. Flüeli, R. Spycher, P. Stadelmann and J.-P. Borel, *Faradat Discuss.*, **1991**, *92*, 173.
[21] S. Ino, *J. Phys. Soc. Japan,* **1969**, *27*, 941.
[22] J.M. Cowley, *Ultramicroscopy* **1992**, *41*, 335.
[23] D. Gabor, *Proc. Roy. Soc. London A* **1949**, *197*, 454.
[24] A. Tonomura, *Electron Holography*, New York, Springer-Verlag **1993**.
[25] H. Lichte, *Adv. Optical and Electron Microsc.* **1991**, *12*, 25.
[26] A. Tonomura, L.F. Allard, G. Pozzi, D.C. Joy and Y.A. Ono eds. *Electron Holography*, Amsterdam, Elsevier Science B.V. **1995**.
[27] G. Möllenstedt, G. *Adv. Optical and Electrons* **1991**, *12*, 1.
[28] B.G. Frost, L.F. Allard, E. Volkl, and D.C. Joy, in *Electron Holography*, eds., A. Tonomura, L.F. Allard, G. Pozzi, D.C. Joy and Y.A. Ono, Amsterdam, Elsevier Science B.V., **1995**, 169.
[29] A.K. Datye, D.S. Kalakkad, E. Vöikl and L.F. Allard, in *Electron Holography*, A. Tonomura, L.F. Allard, G. Pozzi, D.C. Joy and Y.A. Ono eds., Amsterdam, Elsevier, **1995**, 199.
[30] M. Mankos, J. M. Cowley and M.R. Scheinfein, *Mater. Res. Soc. Bulletin,* XX (October) **1995**, 45.
[31] Y. Aharonov and D. Bohm, *Phys. Rev.* **1959**, *115*, 485.
[32] T. Hirayama, J. Chen, Q. Ru, K. Ishizuka, T. Tanji and A. Tonomura, in *Electron Holography*, A. Tonomura, L.F. Allard, G. Pozzi, D.C. Joy and Y.A. Ono eds., Amsterdam, Elsevier, **1995**, 145.
[33] T.S. Ahmadi, Z.L. Wang, T.C. Green, A. Henglein and M.A. El-Sayed, *Science*, **1996**, *28*, 1924.
[34] R.L. Whetten, J.T. Khoury, M.M. Alvarez, S. Murthy, I. Vezmar, Z.L. Wang, C.C. Cleveland, W.D. Luedtke, U. Landman, *Adv. Materials*, **1996**, *8*, 428.
[35] Z.L. Wang, *Adv. Materials*, **1998**, *10*, 13.
[36] Z.L. Wang, J. Petroski, T. Green and M.A. El-Sayed, *J. Phys. Chem. B*, **1998**, *102*, 6145
[37] Z.L. Wang, M. Mohamed, S. Link and M.A. El-Sayed, *surf. Sci.* **1999**, in press.
[38] Y.-Y. Yu, S.-S. Chang, C.-L. Lee and C.R. Wang, *J. Phys. Chem. B,* **1997**, *101*, 6661.
[39] M.B. Mohamed, K.Z. Ismail, S. Link and M.A. El-Sayed, *J. Phys. Chem. B* **1998**, *102*, 9370.
[40] S. Frank, P. Poncharal, Z.L. Wang, and W.A. de Heer, *Science*, **1998**, *280*, 1744.

[41] P. Poncharal, S. Frank, Z.L. Wang, and W.A. de Heer, Proceeding of the International Conference on Small Clusters **1998**, in press.
[42] P. Poncharal, Z.L. Wang, D. Ugarte and W.A. de Heer, *Science*, **1999**, *283*, 1513.
[43] R.F. Egerton, *Electron Energy-Loss Spectroscopy in the Electron Microscope*, 2nd ed., New York, Plenum Pub. Co., **1996**.
[44] Z.L. Wang, *Philos. Mag. B* **1992**, *65*, 559.
[45] Z.L. Wang, *Micron* **1996**, *27*, 265; and **1997**, *28*, 505.
[46] P. Schattschneider, and B. Jouffrey, B., in *Energy Filtering Transmission Electron Microscopy* , ed. L. Reimer, Springer Series in Optical Science, New York, Springer Verlag **1995**, *71*, 151.
[47] P.M. Echenique, J. Bausells, A. and Rivacoba, *Phys. Rev. B* **1987**, *35*, 1521.
[48] T. Stöckli, J.-M. Bonard, A. Châtelain, Z.L. Wang and P. Stadelmann, *Phys. Rev. B* **1998**, *57*, 15599.
[49] T. Stöckli, Z.L. Wang, J.-M. Bonard, A. Châtelain and P. Stadelmann, *Phil. Mag. B*, in press, **1999**.
[50] C. Colliex, Adv. Optical and Electron Microscopy, ed. V.E. Cosslett and R. Barer, London, Academic Press, **1984**, 9, 65.
[51] H. Kurata and C. Colliex, *Phys. Rev. B*, **1993**, *48*, 2102.
[52] D.H. Pearson, C.C. Ahn, and B. Fultz, *Phys. Rev. B*, **1993**, *47*, 8471.
[53] J.L. Mansot, P. Leone, P. Euzen, and P. Palvadeau, *Microsc. Microanal. Microstruct*, **1994**, *5*, 79.
[54] J.A. Fortner, and E.C. Buck, *Appl. Phys. Lett.*, **1996**, *68*, 3817.
[55] S.J. Lloyd, G.A. Botton, and W.M. Stobbs, *J. Microsc.* **1995**, *180*, 288.
[56] J. Yuan, E. Gu, M. Gester, J.A.C. Bland, and L.M. Brown, *J. Appl. Phys.* **1994**, *75*, 6501.
[57] Z.L. Wang, J.S. Yin, J.Z. Zhang, and W.D. Mo, *J. Phys. Chem. B*, **1997**, *101*, 6793.
[58] Z.L. Wang, J.S. Yin, Y.D. Jiang, and J. Zhang, *Appl. Phys. Lett.*, **1997**, *70*, 3362.
[59] Z.L. Wang and J.S. Yin *Philos. Mag. B*, **1998**, *77*, 49.
[60] J.S. Yin and Z.L. Wang, *Phys. Rev. Lett.*, **1997**, *79*, 2570.
[61] L. Reimer ed., *Energy Filtering Transmission Electron Microscopy* , Springer Series in Optical Science, New York, Springer Verlag, **1995**.
[62] A.J. Craven, and C. Colliex, *J. Microsc. Spectrosc. Electron*, **1977**, *2*, 511.
[63] R.D. Leapman and J.A. Hunt, *Microscopy: The Key Research Tool*, published by The Electron Microsc. Soc. of America, **1992**, *22*, 39.
[64] J. Mayer, J. M. Plitzko, *J. Microsc.* **1996**, *183*, 2.
[65] P.E. Batson, N.D. Browning and D.A. Muller, *MSA Bulletin*, published by the Microscoy Society of America, **1994**, *24*, 371.
[66] Z.L. Wang, J. Bentley and N.D. Evans, *J, Phys. Chem. B,* **1999**, *103*, 751.
[67] J. Bentley, S. McKernan, C.B. Carter, and A. Revcolevschi, *Microbeam Analysis*, edited by J.T. Armstrong and J.R. Porter, **1993**, *2* (Suppl.), S286.
[68] J.I. Goldstein, D.E. Newbury, P. Echlin, D.C. Joy, A.D. Romig, C.E. Lyman, C. Fiori, and E. Lifshin, *Scanning Electron Microscopy and X-ray Microanalysis, a text for biologists, materials scientists and geologists,* New York, Plenum Press, **1992**.
[69] S.A. Harfenist, Z. L. Wang, M. M. Alvarez, I. Vezmar, R. L. Whetten, *J. Phys. Chem.*, **1996**, *100*, 13904.
[70] S.A. Harfenist, Z. L. Wang, M. M. Alvarez, I. Vezmar and R. L. Whetten, *Adv. Mater.*, **1997**, *9*, 817.
[71] L. Motte, F. Billoudet, E. Lacaze, J. Douin, M.-P. Pileni, *J. Phys. Chem B*, **1997**, *101*, 138.
[72] R.P. Andres, T. Bein, M. Dorogi, S. Feng, J.I. Henderson, C.P. Kubiak, W. Mahoney, R.G. Osifchin, R. Reifenberger, *Science*, **1996**, *272*, 1323.
[73] C.B. Murray, C.R. Kagan and M.G. Bawendi, *Science*, **1995**, *270*, 1335.
[74] C.P. Collier, R.J. Saykally, J.J. Shiang, S.E. Henrichs and J.R. Heath, *Science*, **1997**, *277*, 1978.
[75] J.S. Yin and Z.L. Wang, *J. Phys. Chem.*, **1997**, *101*, 8979.
[76] S.A. Harfenist and Z. L. Wang, *J. Phys. Chem B*, **1999**, *103*, 4342.
[77] Z.L. Wang, S.A. Harfenist, R. L. Whetten, J. Bentley and N.D. Evans, *J. Phys. Chem. B*, **1998**, *102*, 3068.

Characterization of Nanophase Materials. Edited by Zhong Lin Wang
Copyright © 2000 Wiley-VCH Verlag GmbH
ISBNs: 3-527-29837-1 (Hardcover); 3-527-60009-4 (Electronic)

4 Scanning Transmission Electron Microscopy of Nanoparticles

Jingyue Liu

Ultimately, all materials and living organisms have their origins in the collective assemblies of a small number of atoms or molecules. Human beings have been fascinated by the interior world: the secrets of cells and the building blocks of matter. Ever since various types of microscopes were discovered, they have been the primary instruments for helping us to directly observe and understand matter or cells on an ever-decreasing scale. By understanding what the building blocks are and how they are arranged together to possess unique properties or to display specific functions, we hope to modify, manipulate, and sculpt matter at nanoscopic dimensions for desired purposes.

To understand the fundamental properties of nanoparticles or other nanosystems, it is necessary to characterize their structures at a nanometer or atomic level. This, in turn, allows us to understand the synthesis-structure-property relationships of nanoparticle systems, thus achieving the ultimate goal of the molecular engineering of nanoparticles for important industrial applications.

In Chapter 3, we discussed transmission electron microscopy (TEM) techniques and the use of these powerful techniques for characterizing nanoparticles. In this chapter, we will discuss scanning transmission electron microscopy (STEM) and associated imaging, spectroscopy, and diffraction techniques, as well as the applications of these STEM techniques to the characterization of nanoparticles.

4.1 Introduction to STEM and associated techniques

STEM instruments are tailor-made to provide structural, chemical, and morphological information about individual nanoparticles on a nanometer or atomic level. A remarkable capability of STEM instruments is the formation of high-brightness electron probes with diameters < 0.2 nm at 100 keV and as small as 0.13 nm at 300 keV. To form such an electron nanoprobe, the use of a field-emission gun (FEG) is necessary to provide sufficient signal strength for viewing and recording STEM images, spectra, and diffraction patterns. The FEG source has a brightness of at least 10^3 greater than that of a W or a LaB_6 filament, which is typically used in conventional TEM instruments, but with an effective electron source size of only 4–5 nm in diameter. Another attractive feature of STEM is its great flexibility in the detection system. Different signals generated from the same sample area can be collected either independently or simultaneously and can be analyzed in parallel to yield complementary information about the sample. Figure 4-1 shows a schematic diagram illustrating the available signals that can be used in a STEM instrument to give useful information about the sample.

Unlike in TEM where a stationary, parallel electron beam is used to form images, the STEM is a mapping device. In a STEM instrument, a fine electron probe, formed by using a strong objective lens to de-magnify a small electron source, is scanned over a specimen in a two-dimensional raster. Signals generated from the specimen are

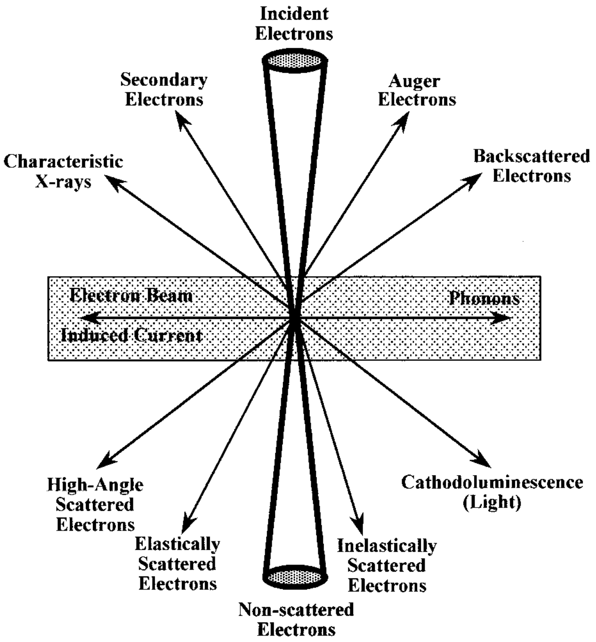

Figure 4-1. Signals generated inside a STEM microscope when a high-energy electron probe interacts with a thin specimen. These signals can be collected, individually or simultaneously, and analyzed to give useful information about the structure and chemistry of the sample.

detected, amplified, and used to modulate the brightness of a second electron beam that is scanned synchronously with the STEM electron probe across a cathode-ray-tube (CRT) display. Therefore, a specimen image is mapped onto the CRT display for observation (Fig. 4-2). If the area scanned on the sample is A_s and the corresponding area on the CRT display is A_d, then the magnification (M) of a STEM image is given by $M = A_d/A_s$. The STEM magnification is purely geometric in origin and can be easily changed by varying the scanned area on the sample.

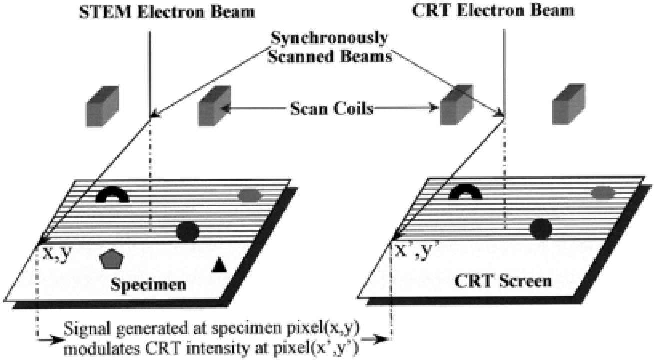

Figure 4-2. Schematic diagram illustrates the formation of a STEM image: signals generated from a thin specimen are detected, amplified, and used to modulate the brightness of a second electron beam scanned synchronously with the STEM electron probe across a cathode-ray-tube (CRT) display. A specimen image is "mapped" to the CRT display for observation.

Since STEM is a serial recording instead of a parallel recording system, the whole process of generating a STEM image is much slower than that in TEM. A STEM image usually builds up over several seconds to several minutes, depending on the types of signals used to produce the image. Unlike in TEM, there is no rotation between the object and image planes, and the microscope magnification can be changed without refocusing the electron beam to obtain a focused image. The resolution of STEM images is primarily determined by the incident probe size, the stability of the microscope, and the inherent properties of the signal generation processes.

Multiple imaging and analytical detectors have been developed to simultaneously collect several signals that can be displayed individually or combined in perfect register with each other. This unique capability makes the STEM a powerful nanoanalytical tool since multiple views of a sample, in different imaging, diffraction, and spectroscopy modes, can be collected, analyzed, and compared in a single pass of the incident electron beam. Figure 4-3 illustrates the available detectors commonly used for collecting imaging and analytical signals in dedicated STEM instruments.

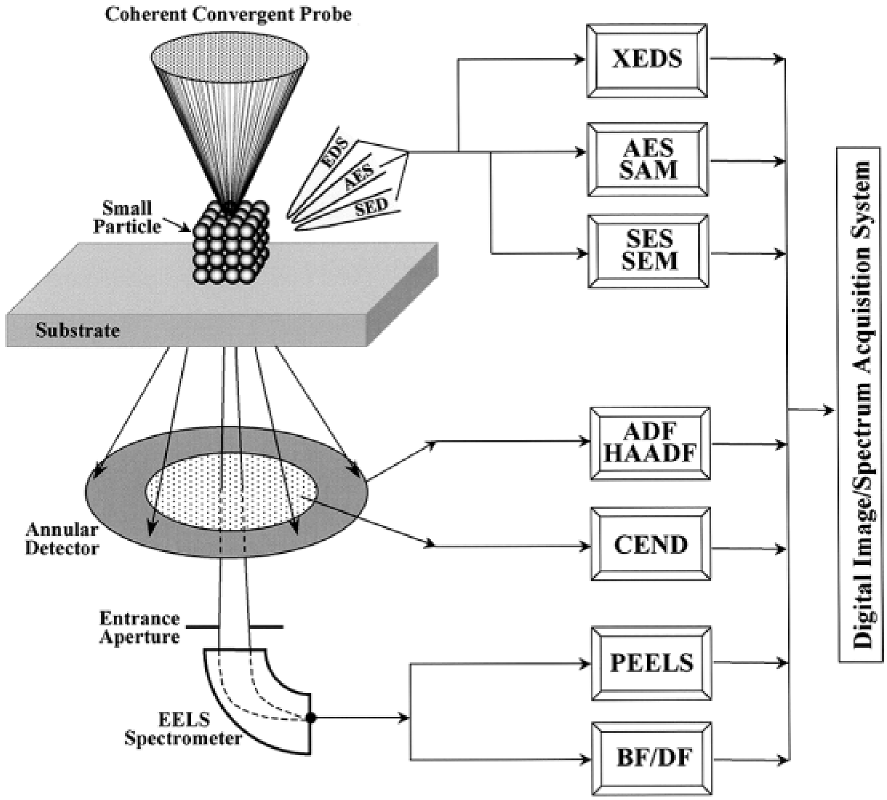

Figure 4-3. Schematic diagram illustrates imaging, diffraction, and spectroscopy modes commonly used in a dedicated STEM instrument: X-ray Energy Dispersive Spectroscopy (XEDS); Auger Electron Spectroscopy (AES) and Scanning Auger Microscopy (SAM); Secondary Electron Spectroscopy (SES) and Secondary Electron Microscopy (SEM); Annular Dark-Field (ADF) and High-Angle Annular Dark-Field (HAADF) microscopy; Coherent Electron Nano-Diffraction (CEND); Parallel Electron Energy-Loss Spectroscopy (PEELS); and Bright-Field (BF) and Dark-Field (DF) microscopy.

By collecting high-angle scattered electrons with an annular detector, high-angle annular dark-field (HAADF) images (or Z-contrast images) can be formed to provide information about structural variations across the sample at an atomic level. Electron energy-loss spectroscopy (EELS) and X-ray energy-dispersive spectroscopy (XEDS) can give quantitative data describing changes of elemental composition, electronic structure, or state of oxidation associated with inhomogeneous structures of the sample. The combination of XEDS and EELS with HAADF imaging technique can provide detailed information on the composition, chemistry, and electronic and crystal structure of nanoparticles with atomic resolution and sensitivity.

Information about surface topography or surface chemistry of nanoparticles can be obtained by collecting and analyzing secondary electron (SE) and Auger electron (AE) signals. By positioning an electron nanoprobe at the area of interest, diffraction patterns from individual nanoparticles can be acquired to provide information about the crystallographic structure of nanoparticles. The structural relationship of nanoparticles to the surrounding materials and, in some cases, the shape of nanoparticles can also be extracted from nanodiffraction patterns. The powerful combination of atomic resolution HAADF imaging with nanospectroscopy and nanodiffraction techniques has proved invaluable in solving a wide range of materials problems.

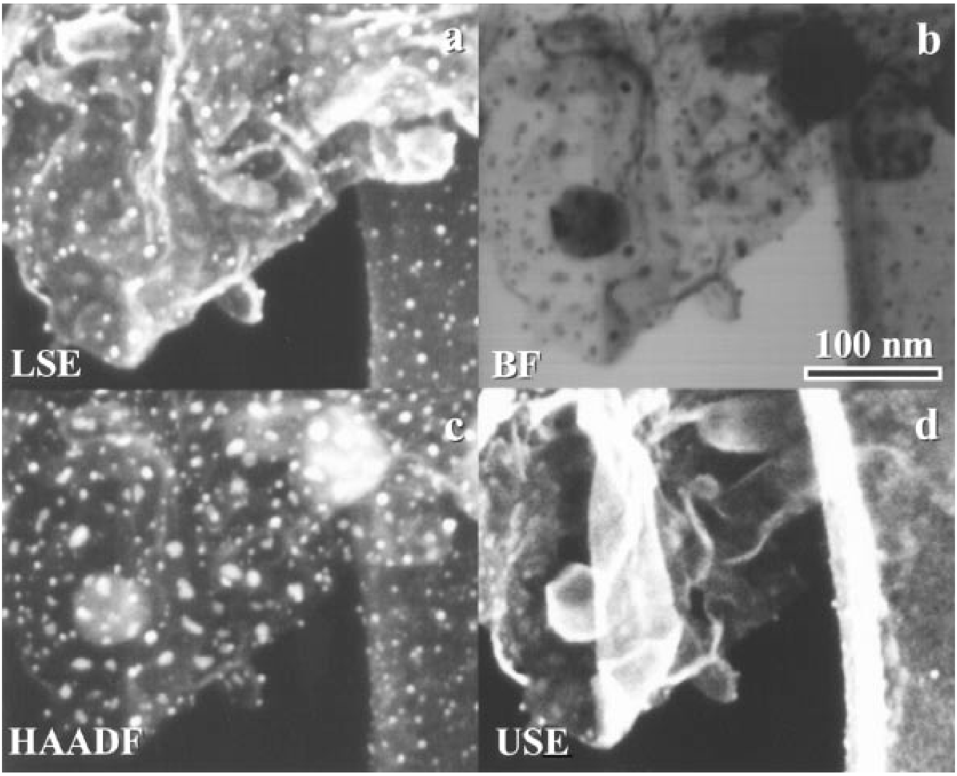

Figure 4-4. Simultaneously acquired STEM images of a supported catalyst: a) entrance-surface SE image; b) BF image; c) HAADF image; d) exit-surface SE image. The size distribution and the relative locations of the metal particles, as well as the morphology of the catalyst support, are clearly revealed in this set of STEM images.

Figure 4-4 shows a set of images, acquired simultaneously, of a supported metal catalyst. Figure 4-4a is an SE image of the entrance surface of the catalyst showing small particles and a detailed surface morphology of the catalyst support. Figure 4-4b is the corresponding bright-field (BF) STEM image, revealing small particles with a dark contrast. Metal particles of various shapes and sizes, dispersed in or on the catalyst support, are clearly revealed in the HAADF image (Fig. 4-4c). The exit-surface SE image (Fig. 4-4d) reveals an unusual surface topography of the catalyst support. Detailed analyses of such sets of images can provide important information about the catalyst: distribution of sizes and relative locations of various types of metal particles present in the supported catalyst. The SE images clearly indicate that the small, spherical particles are located on the entrance side of the support. The larger metal particles with irregular shapes are located in the interior of the catalyst support since these particles are clearly revealed in the HAADF image but are not shown in either the entrance- or the exit-surface SE images. XEDS analysis of these particles can give information about the composition of the individual nanoparticles. The correlation of HAADF images with SE images and XEDS spectra is very effective in identifying which type of the metal particles is exposed to the reacting molecules during a catalytic reaction.

4.2 STEM instrumentation

4.2.1 Dedicated STEM and STEM attachment in TEM

There are two types of STEM instruments commonly used by electron microscopists: dedicated STEM (DSTEM) and STEM attachment in TEM. The DSTEM instruments, which were exclusively made by VG Microscopes (UK), have unique designs and capabilities. A DSTEM microscope uses a cold field-emission gun to generate high-brightness electron probes with sub-nanometer sizes. The sizes of electron probes used in TEM/STEM instruments are generally much larger than those in DSTEM instruments. Furthermore, the operation of STEM attachments is not as flexible as that of DSTEM.

However, recent advances in field-emission technology and the increasing use of field-emission guns in high-resolution 200 kV TEM instruments have made the STEM attachment and associated STEM techniques dominant features in field-emission TEM (FE-TEM) microscopes. When operated in the STEM mode, the recent generation of FE-TEM instruments can provide high-brightness electron probes with sizes as small as those obtainable in DSTEM instruments. HAADF images can now be obtained in FE-TEM microscopes with a resolution similar to, or, in some instances, better than, that obtainable in DSTEM instruments. The distinction between DSTEM and STEM attachments in FE-TEM is rapidly diminishing. In the following, we will focus our discussion exclusively on DSTEM instruments. However, the fundamental principles of DSTEM and associated techniques discussed in this chapter equally apply to STEM operation in FE-TEM. Unless stated otherwise, we will use the acronym STEM to represent DSTEM for the rest of this chapter.

4.2.2 Principal features of a STEM instrument

In a STEM instrument, the cold field-emission gun is generally operated at 100 kV or 300 kV and is placed at the bottom of the microscope column to minimize mechanical disturbances of the field-emission tip. Two condenser lenses and a strong objective lens are usually used to form a small electron probe on the specimen. A virtual objective aperture (VOA) is usually placed before the condenser lenses to control the convergent angle of the incident electron probe. The use of VOA is desirable for reducing stray X-rays, generated inside the microscope column, and hence simplifying the interpretation of XEDS spectra and X-ray elemental maps. A real objective aperture situated just before the specimen is sometimes used to define the angle of incident beam convergence. The size and the intensity of the high-energy electron probe can be manipulated by adjusting the two condenser lenses and by selecting the proper size of the VOA or the real objective aperture.

In some STEM instruments, the electrons, passing through the specimen, directly reach the detector plane without the use of any post-specimen lenses. It is, however, desirable to have post-specimen lenses to offer great flexibility for effectively utilizing various detector configurations and for conveniently observing and recording nanodiffraction patterns.

The easy access to the top of the STEM column provides necessary versatility for modification or construction of various STEM detectors. Interchangeable annular detectors, for example, can be installed to provide flexibility for ADF imaging or for special imaging modes using configured detectors. The attachment of a series EELS or a parallel EELS (PEELS) detector to the top of the microscope column makes it possible to analyze the chemistry of the sample at an atomic resolution. It also allows BF or dark-field (DF) imaging with only elastically scattered electrons or with other selected energy-loss electrons.

A scintillator screen and a low-light level TV camera, together with a VCR, can be used to view or record nanodiffraction patterns at a TV rate. A charge coupled device (CCD) system can also be used for quantitative recording of nanodiffraction patterns, shadow images, or electron holograms.

For effectively collecting characteristic X-rays, a retractable, windowless XEDS spectrometer is usually attached to the column of a STEM instrument. Because of the small volume probed by the electron nanoprobe, the XEDS detector has to be placed close to the sample region to increase the strength of the collected X-ray signal. Two XEDS detectors can be interfaced to the microscope column to significantly increase the strength of the collected X-ray signal.

A stable operation of a cold field-emission gun requires the vacuum in the gun chamber to be better than 10^{-10} torr. The column vacuum is generally better than 10^{-8} torr to prevent significant back streaming of gas molecules into the gun chamber and to reduce the effects of contamination on the specimen surface. Most of the STEM instruments can be baked at moderate temperatures for extended periods to obtain a high vacuum.

Some STEM instruments were specifically designed and constructed to have a true UHV system for surface studies. These instruments have a vacuum better than 10^{-10} torr throughout the whole microscope system and have elaborate auxiliary chambers for preparing, testing, and manipulating specimens in situ. One of these special STEM instruments is the microscope code-named MIDAS (a Microscope for Imaging, Diffraction, and Analysis of Surfaces) which was specifically designed for the study of nanostructures of surfaces and small particles with high spatial resolution. The various

STEM imaging, analytical, and diffraction techniques can be performed on clean nanoparticles or thin films, prepared inside the specimen chamber and treated at different temperatures or with various gases. In addition, secondary and Auger electrons, emitted from both the entrance and the exit surfaces of a sample, can be collected to form surface images. Figure 4-5 shows a photograph of the essential components of the MIDAS system.

Because of the intrinsic nature of a mapping device, the STEM is ideal for digital imaging and for on-line or off-line processing of images, spectra, and nanodiffraction patterns. Signals from several detectors can be digitally acquired either simultaneously or independently; different signals can also be combined together by addition, subtraction, multiplication, or other mathematical manipulations to gain insight about the structure of the sample. These digital images or spectra can be electronically transferred to remote locations through the Internet or the World Wide Web for fast dissemination of vital information.

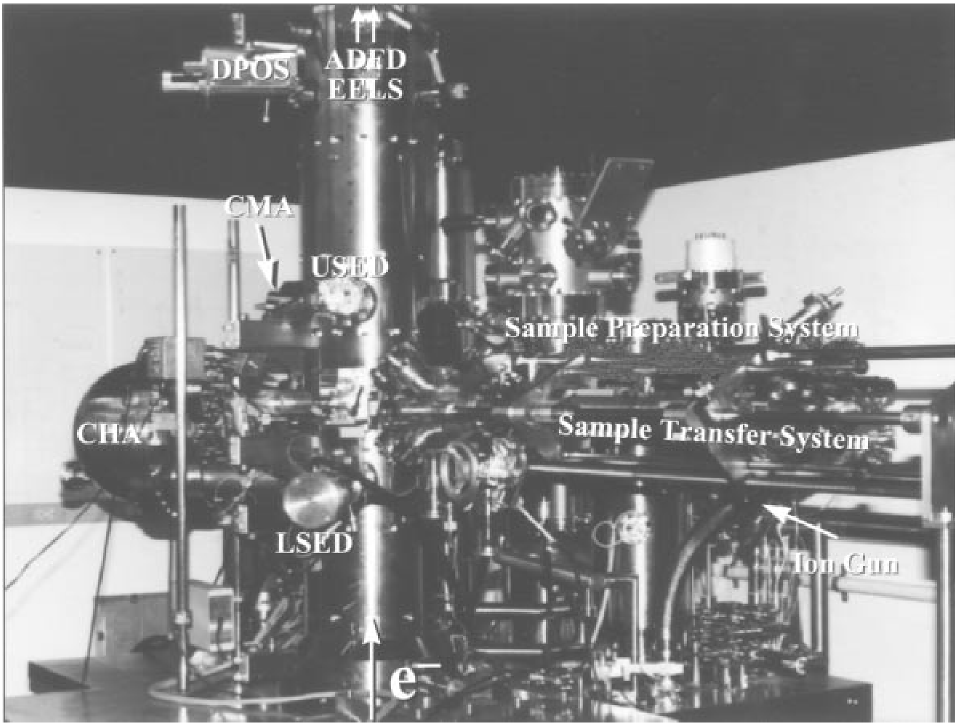

Figure 4-5. A photograph shows the main features of a specially designed UHV STEM HB-501S housed at Arizona State University (code-named MIDAS—Microscope for Imaging, Diffraction, and Analysis of Surfaces). The electron beam travels from bottom to top in dedicated STEM instruments. Annular Dark-Field Detector (ADFD); Electron Energy-Loss Spectrometer (EELS); Diffraction Pattern Observation Screen (DPOS); Cylindrical Mirror Analyzer (CMA); Concentric Hemispherical Analyzer (CHA); Upper Secondary Electron Detector (USED); Lower Secondary Electron Detector (LSED).

4.3 Imaging with high-energy electrons

4.3.1 The principle of reciprocity

The principle of reciprocity developed in the light optics can be equally applied to electron optical systems [1–2]. The wave amplitude at a point P due to a point source at Q is identical to the wave amplitude at Q due to a point source at P (Fig. 4-6). The essential components of a STEM imaging system are similar to those of a TEM microscope: the ray diagram of STEM is the reciprocal of that of TEM. This is demonstrated with the aid of the schematic ray-diagram of Fig. 4-6. The STEM detector replaces the TEM electron source; the STEM gun is placed in the detector plane of the TEM; and the scanning system translates the STEM source to cover the TEM recording plate. Therefore, for a particular detector configuration, the contrast of STEM images can often be inferred by finding the equivalent TEM geometry. For example, BF STEM images obtained by collecting electrons scattered into a small-angle θ can be interpreted the same way as those of BF TEM images obtained with an illumination angle of θ. Images obtained with a large BF STEM detector are similar to those obtained in TEM with a large illumination angle of the incident beam. The principle of reciprocity makes it possible to apply imaging theories developed in TEM to the interpretation of the corresponding STEM images.

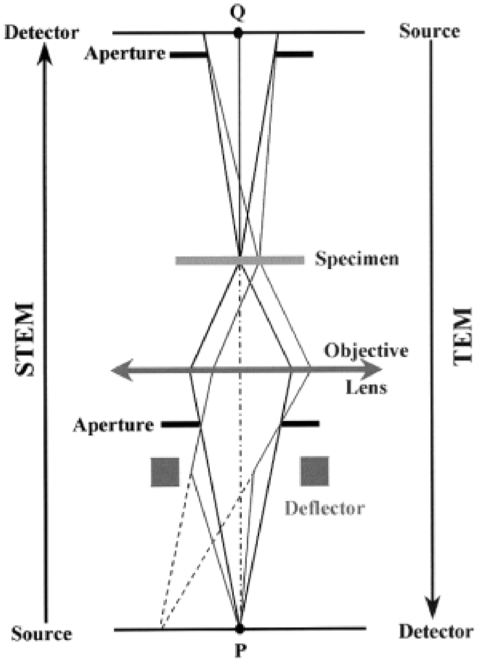

Figure 4-6. Schematic ray-diagram illustrates the Principle of Reciprocity in electron optics: the ray diagram of STEM is the reciprocal of that of TEM. The STEM detector replaces the TEM electron source; the STEM gun is placed in the detector plane of the TEM; and the scanning system translates the STEM source to cover the TEM recording plate.

4.3.2 Theoretical background

When a finely focused electron probe interacts with a thin specimen, the high-energy incident electrons are scattered by the sample electrons and nuclei. The amplitude distribution of the incident electrons at the exit surface of the sample can be described by a wave function $\Psi(\mathbf{K})$. The variable $\mathbf{K}$ is a two-dimensional vector in the reciprocal space with $|\mathbf{K}| = 2\sin(\theta/2)/\lambda$ (θ is the scattering angle and λ is the wavelength of the incident electrons). When the electron probe is scanned across the sample, variations of $\Psi(\mathbf{K})$ carry information about the electron beam-specimen interactions. If the exit wave function $\Psi(\mathbf{K})$ of the scattered high-energy electrons can be determined, we can extract structural information about the sample of interest. It is, however, not possible to directly measure $\Psi(\mathbf{K})$. What can be obtained experimentally are images of the sample formed by collecting the directly transmitted or scattered electrons. The observed image intensity, $I(\mathbf{X})$, as a function of the beam position $\mathbf{X}$ is related to $\Psi(\mathbf{K})$ by:

$$I(\mathbf{X}) = \int D(\mathbf{K})\, |\Psi(\mathbf{K}, \mathbf{X})|^2\, d\mathbf{K} \tag{4-1}$$

where $D(\mathbf{K})$ is the transmission function of the detector. The amplitude function $\Psi(\mathbf{K}, \mathbf{X})$, to first approximation [3, 4], can be expressed as:

$$\Psi(\mathbf{K}, \mathbf{X}) = Q(\mathbf{K}) * T(\mathbf{K}) \exp\{2\pi i \mathbf{K} \cdot \mathbf{X}\} \tag{4-2}$$

where $Q(\mathbf{K})$ is the Fourier transform of the object transmission function, $q(\mathbf{x})$, of the sample and the * symbol represents convolution. The transfer function of the microscope, $T(\mathbf{K})$, is given by:

$$T(\mathbf{K}) = A(\mathbf{K}) \exp\{i\chi(\mathbf{K})\} \tag{4-3}$$

The aperture function, $A(\mathbf{K})$, is given by:

$$A(\mathbf{K}) = \begin{cases} 1 & \text{for K} < \text{K}_0 \\ 0 & \text{for K} > \text{K}_0 \end{cases} \tag{4-4}$$

The aberration function of the objective lens, $\chi(\mathbf{K})$, is given by:

$$\chi(\mathbf{K}) = \pi \Delta \lambda K^2 + \pi C_s \lambda^3 K^4 / 2 \tag{4-5}$$

where Δ is the defocus value, C_s is the spherical aberration coefficient of the objective lens, and K_0 is the cut-off wave-vector determined by the size of the objective aperture.

The amplitude distribution of the incident probe, $t(\mathbf{x})$, is determined by the Fourier transform of $T(\mathbf{K})$ which is determined by the aperture function $A(\mathbf{K})$ and the aberration function $\chi(\mathbf{K})$ of the objective lens. The probe size, therefore, depends on the spherical aberration coefficient of the objective lens, the wavelength of the incident electrons, the size of the objective aperture, and the defocus of the electron beam.

To determine the transmission function of the object, $q(\mathbf{x})$, requires a reconstruction of the exit wave function and a solution to the inverse dynamic diffraction problem which is beyond the scope of this book. In order to gain insight about the image

resolution and contrast, however, various types of approximations can be made to simplify $q(\mathbf{x})$. In the phase object approximation [3, 4], for example, $q(\mathbf{x})$ can be expressed as:

$$q(\mathbf{x}) = \exp(-i\sigma\phi(\mathbf{x})) \tag{4-6}$$

where $\sigma = \pi/(\lambda E_0)$ = interaction constant, E_0 = accelerating voltage, and $\phi(\mathbf{x})$ = projected specimen potential along the incident beam direction. For most practical studies, however, rigorous dynamical calculations have to be performed to determine the image of specific specimen structures.

The detector function $D(\mathbf{K})$ plays a significant role in determining the final form of STEM images. For example, if $D(\mathbf{K}) \equiv 1$ for all scattering angles, the STEM image is formed by collecting all the high-energy electrons penetrating through a thin sample. Then, the image intensity $I(\mathbf{X})$ does not vary with the beam position $\mathbf{X}$ because of the conservation of the total number of high-energy electrons (we neglect here the effect of backscattered electrons which is negligible for very thin specimens). Therefore, no contrast will be observed in the STEM image, and no information about the specimen can be inferred.

If $D(\mathbf{K}) = \delta(\mathbf{K})$ or $\delta(\mathbf{K}-\mathbf{G})$ where $\mathbf{G}$ is a reciprocal lattice vector, the Eq. (4-1) reduces to: $I(\mathbf{X}) = |\Psi(\mathbf{0}, \mathbf{X})|^2$ or $|\Psi(\mathbf{G}, \mathbf{X})|^2$. This is exactly same as for BF or DF TEM imaging with parallel illumination. For other detector configurations, the evaluation of the Eq. (4-1) is not straightforward. Various types of approximations, however, can be made to gain insight into the characteristics of the images formed by collecting the corresponding signals [4].

With configured STEM detectors we can, nevertheless, rewrite the Eq. (4-1) as:

$$I_i(\mathbf{X}) = \int_{K_i}^{K_{i+1}} D_i(\mathbf{K})|\Psi(\mathbf{K}, \mathbf{X})|^2 \, d\mathbf{K} \tag{4-7}$$

$$\sum_i \int_{K_i}^{K_{i+1}} D_i(\mathbf{K})|\Psi(\mathbf{K}, \mathbf{X})|^2 \, d\mathbf{K} = 1 \tag{4-8}$$

where the summation is over the whole diffraction plane.

The resolution and contrast of STEM images depend on the configuration of the STEM detector used to form these images. By selecting the shape and the size of the STEM detector, a variety of imaging modes can be used to extract complementary information about the sample.

When a small electron probe is positioned on the sample, all information carried by high-energy electrons is contained in the whole diffraction pattern. The intensity distribution in the diffraction plane varies with the change of the incident beam position provided the electron probe is small enough to resolve the lattice spacings of a crystal. The total integrated intensity across the whole diffraction plane does not vary with the change of the probe position.

By digitally recording the whole diffraction pattern with energy (E) discrimination for each pixel (probe position $\mathbf{X}$) on the sample, a five-dimensional function $I(\mathbf{K}, \mathbf{X}, E)$ can be generated. All information about the specimen can be extracted by off-line processing of these digitally stored, energy-selected diffraction patterns. By selecting certain portion(s) of the scattered electrons as an input signal, various types of images can be formed to give information about the structure and the chemistry of the sample with atomic resolution. This process, however, needs a tremendous amount of compu-

ter work, fast image-acquisition systems, a large collection of data, and a high stability of the microscope parameters. Impressive progress has been made in the last few years [5–7]. In the following, we will focus our discussion on a few simple, but very powerful, imaging modes which can provide high-resolution structural information about nanoparticles.

4.3.3 High resolution BF and DF STEM imaging

When a finely focused STEM probe interacts with a thin crystal oriented along a principal zone-axis, an electron diffraction pattern consisting of a set of convergent beam discs is obtained. Each disc subtends the same semi-angle α, determined by the size of the objective aperture, at the specimen (Fig. 4-7a). If $\alpha > \theta_B$ (θ_B is the Bragg diffraction angle of the diffracting planes), then the convergent beam diffraction discs overlap. For thin, perfect crystals, the electron intensity within non-overlapping regions (e.g., the region indicated by the numeral 1 in Fig. 4-7b) is independent of the probe position and the aberrations of the probe forming lens [8]. The electron intensity within regions where discs do overlap depends on the probe position, the lens aberrations, and the defocus values of the objective lens. The intensity modulations in the

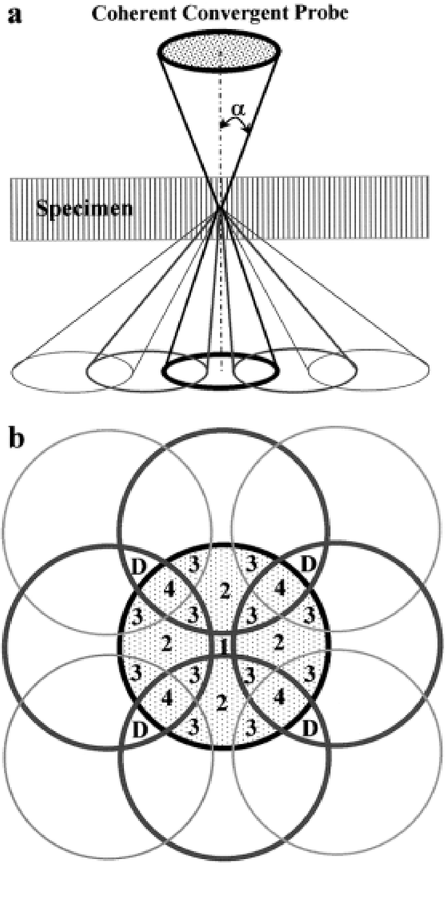

Figure 4-7. Schematic diagrams illustrate the overlap of diffraction discs in a convergent beam, electron diffraction pattern: (a) side view, (b) plane view. Lattice fringes can be obtained by positioning a small STEM detector at any point in the regions of overlapping discs. The numeral 2 stands for two-beam interference, 3 for three-beam interference, 4 for four-beam interference, and the letter D indicates detector positions for dark-field lattice imaging.

overlapping regions are caused by coherent interference of high-energy electrons with different incident directions. The intensity at any point in the overlapping regions varies, in simple cases, sinusoidally with the periodicity ($\lambda/2\theta_B$) of the crystal lattice [8].

If a STEM detector is positioned at any point in the overlapping regions, lattice fringes can be acquired by scanning the electron probe across the sample. Two-dimensional lattice fringes can be obtained by positioning the STEM detector at a point where three or more non-systematic diffraction discs overlap. These multiple-beam regions are labeled as numeral 3 (three-beam interference) and numeral 4 (four-beam interference) in Fig. 4-7b. High-resolution BF STEM images are, by invoking the principle of reciprocity, similar to high-resolution TEM images discussed in Chapter 3. Figure 4-8 shows such a BF STEM lattice image of oxide nanoparticles dispersed on a thin carbon film.

High-resolution DF STEM images can be easily obtained by moving the detector to a point outside the directly transmitted disk. For example, a two-dimensional DF STEM lattice image can be obtained by shifting the STEM detector to the position D labeled in Fig. 4-7b. DF STEM imaging technique is useful for identifying small particles in supported metal catalysts, defects in extended crystals, and different phases in polycrystalline nanophase materials.

The contrast of high-resolution STEM images varies with the displacement of the STEM detector. The movement of the STEM detector corresponds to beam tilt in TEM. In STEM, however, the relative shift of the BF detector is easily accomplished by deflecting the whole diffraction pattern with the use of scanning coils. Unlike beam tilt in TEM, the movement of scanning coils does not disturb the optical alignment of STEM microscopes. Thus, the contrast of specific features of a sample can be conveniently enhanced or reduced by shifting the position of the STEM detector without the

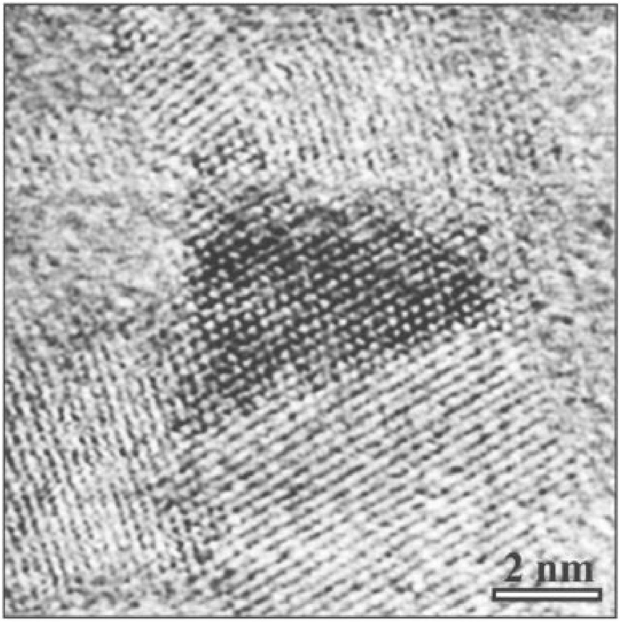

Figure 4-8. Atomic resolution BF STEM image of oxide nanoparticles supported on an amorphous carbon film.

complication of disturbing the microscope alignment. This method is useful for imaging highly inhomogeneous samples, especially for identifying small particles and for imaging interphase interfaces with enhanced chemical sensitivity.

There are some advantages of using BF STEM over TEM for examining thick specimens. Since inelastic scattering produces a spread of energies of the transmitted electrons, the chromatic aberration of the objective lens degrades the image resolution in TEM. In STEM, on the other hand, because the objective lens comes before the specimen, such energy spread does not affect the image resolution. Traditionally, the use of an electron energy-loss spectrometer gives more flexibility in STEM imaging. For example, STEM images can be formed with only elastically scattered electrons, or with plasmon-loss electrons, or any other energy-loss electrons. With the increasing use of energy filters in modern TEM instruments [9], however, the distinction between energy-filtered TEM and STEM imaging is rapidly abating.

4.3.4 Large-angle bright-field imaging

The phase contrast of STEM images rapidly decreases with the increase of the detector collection angle. Due to the principle of reciprocity, the increase of the collection angle in STEM is equivalent to the increase in the illumination convergent angle in TEM. The use of large convergent angle of illumination in TEM pushes the first crossover of the contrast transfer function (CTF) to higher values and causes a rapid damping of high frequency oscillations in the CTF obtained with parallel-beam illumination [10]. Thus, interpretable image resolution can be improved at the expense of image contrast.

For a STEM detector large enough to coincide with the disc of directly transmitted electrons, i.e. $D(\mathbf{K}) = A(\mathbf{K})$, imaging theory suggests that, with a phase object approximation, the image intensity can be approximated by [4, 11]:

$$I_{\mathrm{BF}}(\mathbf{X}) = 1-2[1-\cos(\sigma\phi(\mathbf{X}))]*|t(\mathbf{X})|^2 \tag{4-9}$$

In a weak phase object approximation $\cos(\sigma\phi(\mathbf{X})) \sim 1-½(\sigma\phi(\mathbf{X}))^2$, thus:

$$I_{\mathrm{BF}}(\mathbf{X}) = 1-(\sigma\phi(\mathbf{X})^2*|t(\mathbf{X})|^2 \tag{4-10}$$

This is a form of incoherent imaging: the phase contrast is washed out and the image resolution is determined by the probe current distribution inside the sample.

By changing the strength of the post-specimen lenses, the collection angle of the STEM detector can be easily varied. If we collect all the directly transmitted electrons, plus a large portion of the scattered electrons, a large-angle BF (LABF) image of the sample can be obtained. The dominant phase contrast visible in BF STEM images (Fig. 4-9a) is mostly suppressed in LABF images (Fig. 4-9b). The contrast of LABF images is predominantly due to absorption effects, weak diffraction contrast, plus an electron channeling effect.

For crystals with principal zone-axes aligned in the incident beam direction, the diffraction and phase contrast are significantly reduced in LABF images; but the image resolution is improved. Figure 4-10a shows a high-resolution BF STEM lattice image of a GaAs crystal oriented in the [110] zone-axis. Figure 4-10b shows a corresponding image obtained with a LABF detector (semi-collection angle of about 30 mrad). The LABF image clearly shows a better image resolution and an enhanced image contrast.

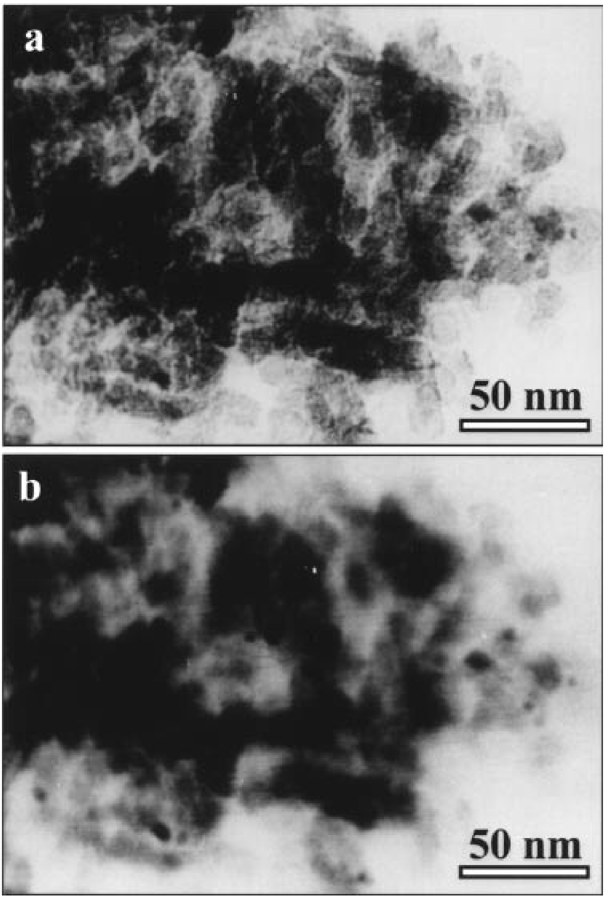

Figure 4-9. BF (a) and large-angle BF (b) STEM images of Pt nanoparticles supported on γ-alumina crystallites. The strong phase and diffraction contrast present in the BF image is suppressed in the large-angle BF image.

The contrast characteristics of LABF lattice images include less dependence on the beam defocus and sample thickness, but strong dependence on the channeling condition of the crystal. These are similar to the characteristics of annular dark-field (ADF) images (see detailed discussions in section 4.3.5).

To understand the characteristics of LABF images, we rewrite the Eq. (4-8) as:

$$\int [D_{\mathrm{LABF}}(\mathbf{K}) + D_{\mathrm{ADF}}(\mathbf{K})]|\Psi(\mathbf{K},\mathbf{X})|^2 d\mathbf{K} = I_{\mathrm{LABF}}(\mathbf{X}) + I_{\mathrm{ADF}}(\mathbf{X}) \equiv 1 \qquad (4\text{-}11)$$

$$I_{\mathrm{LABF}}(\mathbf{X}) = 1 - I_{\mathrm{ADF}}(\mathbf{X}) \qquad (4\text{-}12)$$

Thus, the contrast of LABF images is complementary to the contrast of ADF images obtained with an inner collection angle as large as that of the LABF detector. LABF images can be interpreted in the same way as low-angle ADF images: improvement in image resolution and increased atomic-number sensitivity.

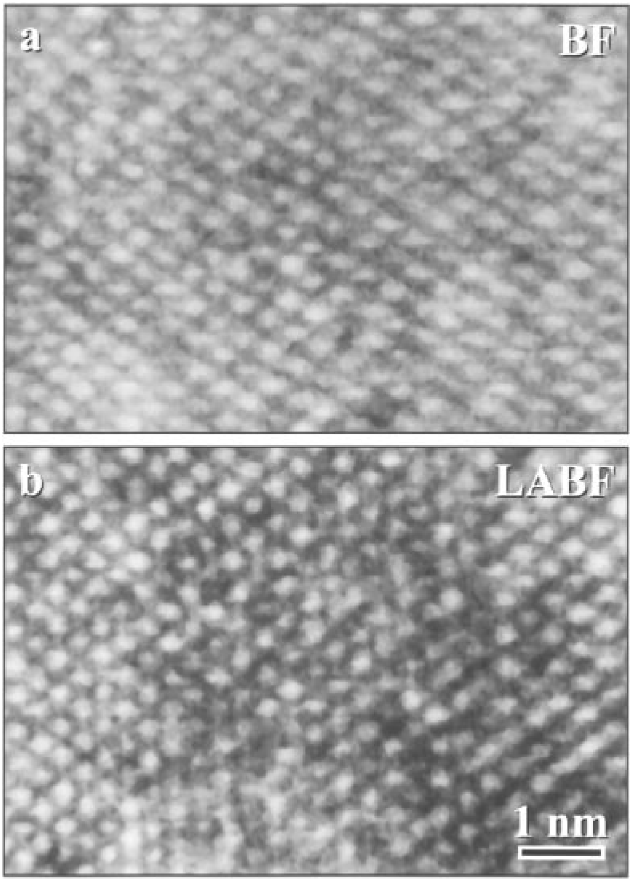

Figure 4-10. Atomic resolution BF (a) and large-angle BF (b) STEM images of the same area of a GaAs crystal oriented along the [110] zone axis. The large-angle BF STEM image clearly shows a better resolution and a higher contrast.

4.3.5 Annular dark-field and high-angle annular dark-field imaging

By collecting electrons scattered outside the central beam in the diffraction pattern, a high-resolution ADF image of the sample can be obtained. In fact, atomic resolution imaging was first achieved in STEM by using an ADF detector to collect electrons scattered from heavy atoms supported on ultra-thin, light-element substrate [12–14]. The high efficiency of the ADF signal made it possible to image individual atoms of heavy-elements, and to study the motion and diffusion of atom clusters [15]. Atomic rows in small crystallites and different layers of atoms were also observed in ADF STEM images, and for very small clusters, quantized levels of integrated intensity of atoms were observed [16–17].

However, the ADF imaging mode has its drawbacks. Because of the low collection angle of the ADF detector, strong dynamical diffraction effects may obscure the compositional sensitivity in ADF images of polycrystalline materials or of small metal particles that are supported on polycrystalline substrates.

The contrast of ADF images critically depends on the inner and outer collection angles of the ADF detector. The diffraction effects in ADF images of crystalline materials can be greatly suppressed by increasing the inner collection angle of the ADF detector beyond the Bragg reflections so that only high-angle scattered electrons contribute to the collected signal [18]. This new imaging mode is called HAADF or Z-contrast imaging. In HAADF images, the diffraction and phase contrast is significantly suppressed and the compositional sensitivity is recovered.

The development of HAADF imaging technique has proved very successful for characterizing small particles and supported metal catalysts with sub-nanometer or atomic resolution and high compositional sensitivity [19–24]. Small metal particles supported on polycrystalline materials cannot be reliably detected in BF or low-angle ADF images because of the strong diffraction and phase effects (Fig. 4-11a), but these nanoparticles can be easily recognized in HAADF images (Fig. 4-11b).

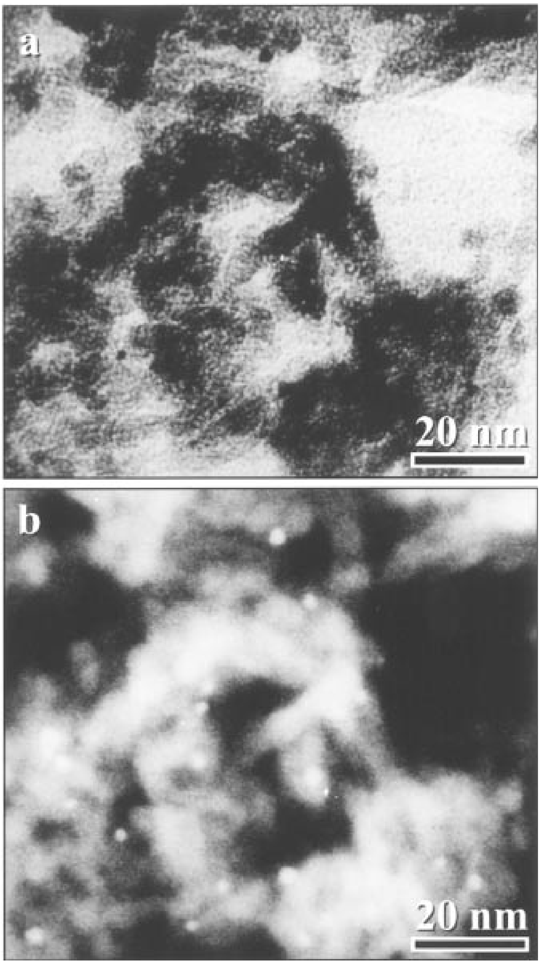

Figure 4-11. BF (a) and HAADF (b) STEM images of Pt nanoparticles supported on γ-alumina crystallites. The phase and diffraction contrast of the γ-alumina crystallites is significantly reduced and the Pt particles are clearly revealed in the HAADF image.

By using post-specimen lenses, we can conveniently switch from low-angle ADF to HAADF imaging mode to study the contrast variations in ADF images. With the increase of the inner collection angle, the phase and diffraction contrast slowly decreases, the atomic-number contrast becomes dominant; but the signal-to-noise ratio of the ADF images decreases. The inner collection angle (α_1) for low-angle ADF images is usually greater than 10 mrad and the outer collection angle (α_2) is generally set at about 50 mrad (Fig. 4-12). For HAADF imaging, however, the appropriate inner collection angle of the ADF detector depends on the nature of the sample and the orientation of crystalline materials. For imaging polycrystalline materials or small particles, the inner collection angle (β_1) is usually greater than 100 mrad and the outer collection angle (β_2) can be as high as a few hundred mrad. For imaging zone-axis crystals, however, β_2 is usually set at an angle smaller than the first-order Laue pattern to reduce contributions of high order Bragg scattering, and β_1 is about 50–60 mrad.

The resolution attainable in HAADF images is better than the resolution obtainable in BF STEM or TEM images using the same lenses [4, 15, 25–27]. Observation of high-resolution details of crystalline specimens on a scale < 0.2 nm can be achieved by using 100 keV electrons [28–32], and a resolution of less than 0.13 nm has been achieved by using 300 keV electrons [33, 34]. Because of the high atomic-number sensitivity and high spatial resolution, the HAADF technique is undoubtedly one of the most useful imaging techniques for studying nanoparticles, supported catalysts, and interfaces in semiconductors, ceramics, and superconducting materials.

The strength of the high-angle scattering, which gives the HAADF imaging signal, depends on several parameters including: 1) large-angle elastically scattered electrons, 2) phonon scattered electrons, and 3) inelastically scattered electrons. Various simulations using dynamical diffraction theory have been performed to understand the nature of HAADF imaging signal [35–43].

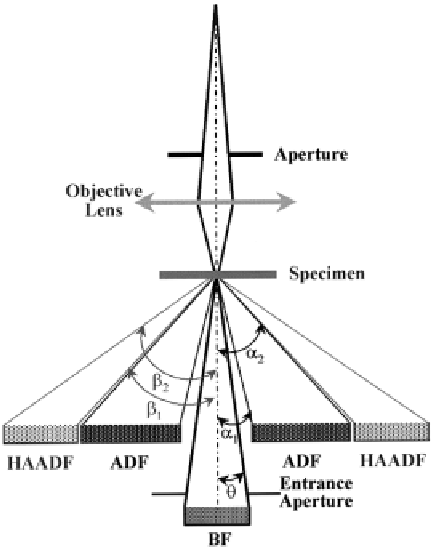

Figure 4-12. Schematic diagram illustrates the geometric arrangement of BF, ADF, and HAADF detectors. The parameter θ represents the collection (semi-) angle of the BF detector; α_1 and α_2 are the inner and outer collection (semi-) angle of the ADF detector, respectively; β_1 and β_2 are the inner and outer collection (semi-) angle of the HAADF detector, respectively.

The imaging theory of HAADF microscopy follows that of incoherent imaging: the high-angle scattered electrons can be treated incoherently. The lateral coherence of the scattered electrons is almost completely suppressed because of detector geometry (averaging effect) and thermal diffuse (phonon) scattering of high-energy electrons. The columnar coherence of the scattered electrons is significantly reduced because of phonon scattering although a small residue of the coherence still exists along the incident beam direction [42, 43]. The contrast characteristics of incoherent HAADF imaging include: 1) high atomic-number sensitivity, 2) less dependence on beam defocus and sample thickness, and 3) absence of proximity effects at interfaces.

For zone-axis crystals, high-energy electrons may preferentially travel along paths of low-energy potentials in the sample. This phenomenon is called the electron channeling in crystalline materials [44]. The propagation of a coherent-convergent electron probe inside a perfect crystal in the zone-axis channeling condition has been widely investigated [36, 44–49]. Remarkable electron focusing effects can occur under channeling conditions. The penetration of the incident electrons is different for probes focused onto atomic columns of different species. The channeling effect of a convergent probe is important in interpreting high-resolution HAADF images of crystals oriented in principal zone-axes [36]. Thermal diffusing scattering, plus the channeling effect, forms the basis of atomic resolution HAADF imaging of crystalline materials. The channeling effect, however, may not significantly affect the contrast of small particles since small particles are usually randomly oriented.

In the incoherent imaging limit, the image contrast becomes a pure "number contrast": the total number of high-angle scattered electrons determines the image intensity at that pixel. Thus, HAADF images can be viewed as the convolution of the intensity distribution of the incident probe with appropriate cross-sections for high-angle scattering processes. Since high-angle scattering processes are highly localized, the resolution of HAADF images is necessarily determined by the size of the incident electron probe.

With coherent, convergent beam illumination, the intensity distribution of the incident probe, $I_0(\mathbf{x})$, rather than the vaguely defined probe size, is usually used to describe the performance of a STEM instrument. The form of $I_0(\mathbf{x})$ strongly depends on the size of the objective aperture, the spherical aberration coefficient of the objective lens, the beam defocus, the energy of the incident electrons, and the instability of the microscope. The "optimum" probe sizes in a STEM instrument depend on the selected imaging and analytical modes [11, 50]. With the use of small objective apertures, usually used for nanodiffraction and nanoanalysis, the intensity distribution of the electron probe does not vary appreciably with the change of beam defocus. On the other hand, with the use of large objective apertures, such as those used in high-resolution STEM imaging, the intensity distribution within the electron probe becomes increasingly sensitive to the change of beam defocus. Figure 4-13 shows calculated intensity distributions of a small electron nanoprobe at different defoci. The central peak of the nanoprobe narrows with increasing under-focus, but the side lobes also become significant.

For high-resolution imaging of zone-axis crystals, it is desirable to use a large objective aperture and to work at an under-focus value slightly larger than the Scherzer focus to improve image resolution without introducing complications in image interpretation [32]. For imaging small particles, however, an analytical probe (top-hat shape) may give shaper images.

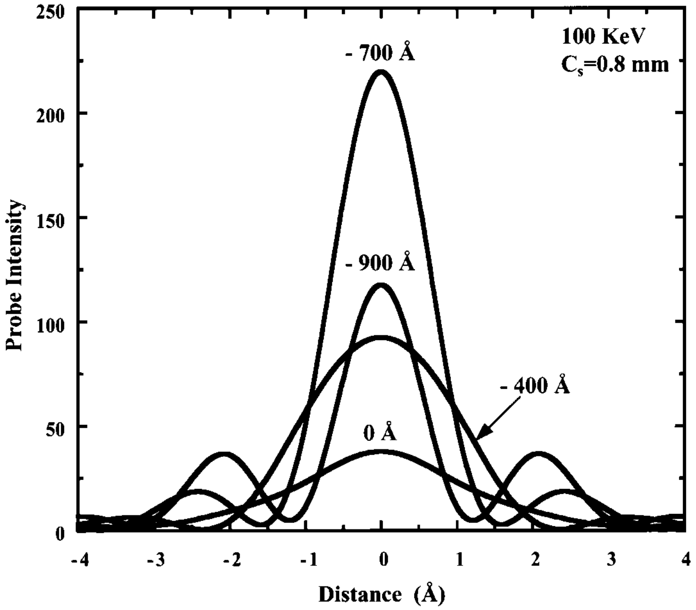

Figure 4-13. Calculated intensity distributions of an electron nanoprobe at different values of defocus: $C_S = 0.8$ mm; $E = 100$ keV; incident beam semi-angle of convergence $\alpha = 12$ mrad.

HAADF images of nanoparticles can be intuitively interpreted as the convolution of the intensity distribution of the probe with the scattering power of the particles (Fig. 4-14a). For an infinitely small electron probe, the image intensity profile should give information about the shape of nanoparticles with an atomic resolution. In practice, however, the finite probe complicates the interpretation of HAADF images. Therefore, it is difficult to unambiguously determine the shape of nanoparticles in HAADF images. When the under-focus value is too large, the intensity in the central peak of the probe can be much less than that in the side lobes; thus an annular ring-like probe may be formed. The corresponding HAADF images of small particles should show annular rings with an intensity modulation weighted by the scattering power of the particles (Fig. 4-14b).

The high atomic-number sensitivity, the incoherent imaging characteristics, and the intuitive relationship to the object make HAADF imaging the most powerful STEM technique for characterizing small particles, interfaces, and superstructures. For example, supported nanoparticles with sizes < 1 nm are difficult to be identified in high-resolution TEM (HRTEM) images. Image distortion also poses a severe problem for correctly interpreting HRTEM images of small particles without extensive image simulations [51]. However, sub-nanometer sized particles and even single atoms can be detected in HAADF images with high contrast [20–24].

The effective penetration depth of high-energy incident electrons increases with their scattering angle. This general argument is true for both elastic and inelastic scattering processes. Thus, it is an advantage to examine relatively thick samples by collecting high-angle scattered electrons. Depending on the inner and outer collection angle of the ADF detector, plural and multiple scattered electrons may significantly contribute to the collected signal. Multiple scattering events redistribute the angular

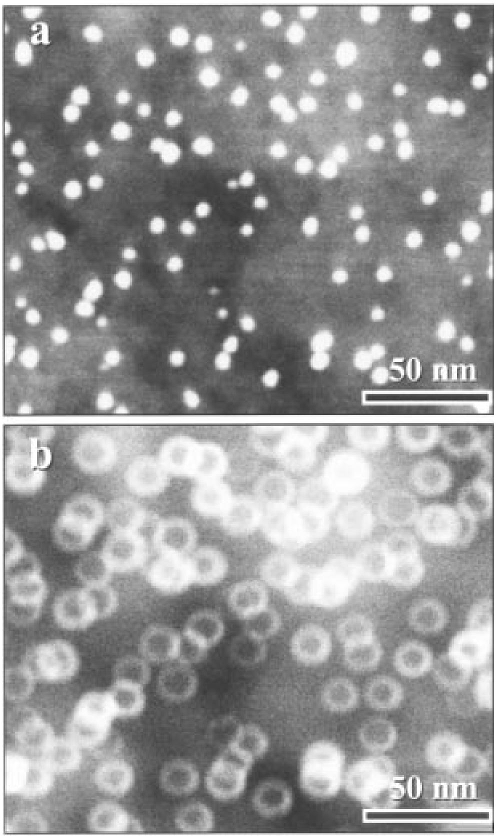

Figure 4-14. In-focus (a) and under-focus (b) HAADF images of the same sample area of Pt nanoparticles dispersed on a highly activated carbon support. The annular rings shown in image (b) represent the shape of the under-focused electron nanoprobe. All the rings have a similar size, but their intensities are weighted by the scattering power of the individual Pt particles.

distribution of the scattered electrons in the diffraction plane; they broaden the width of the angular distribution of the scattered electrons so that the high-angle ADF signal is enhanced for thick specimens.

For imaging thick samples consisting of metal particles dispersed on a light-element support, BF TEM or STEM images can not give much information about the sample because of plural and multiple scattering of incident electrons (Fig. 4-15a). ADF images, however, can still give useful information about the size and spatial distribution of nanoparticles [52]. At low collection angle, high atomic-number particles show white contrast in thin regions of the sample; but these particles show dark contrast in thick regions of the sample because of the plural and multiple scattering effects (Fig. 4-15b). With the increase of the inner and outer collection angle, the contrast of particles in thick regions diminishes first (Fig. 4-15c), and then changes to bright (Fig. 4-15d). This technique can be effectively utilized for correlating the features observed in the thinner regions of a specimen to those in thicker regions.

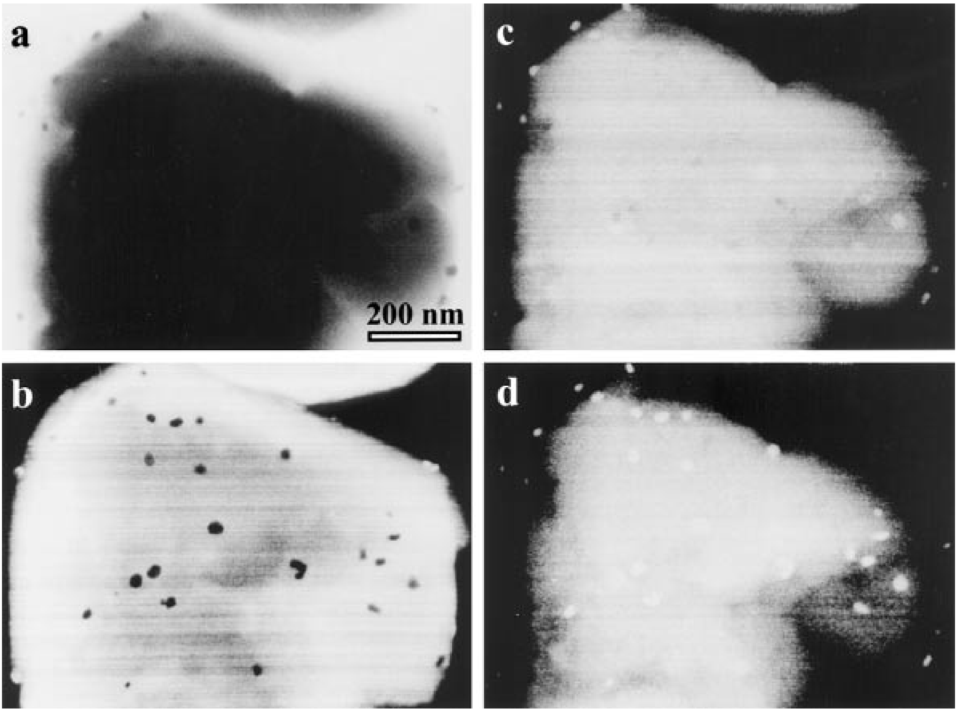

Figure 4-15. A set of STEM images of metal particles supported on zeolite crystals illustrates the variations of image contrast of nanoparticles with the change of the scattering angle. The BF image (a) shows a few metal particles near the edge of the large zeolite particle. The low-angle ADF image (b) shows some metal particles near the edge of the support with a slightly bright contrast and metal particles inside the support with a dark contrast. The ADF image (c) obtained with an intermediate inner collection angle does not show much contrast of the metal particles at all. The HAADF image (d) shows all metal particles with a bright image contrast.

4.3.6 Thin annular detector and other configured detectors

The central beam of the diffraction pattern can be expanded, by use of post-specimen lenses, to overlap the inner edge of the ADF detector. A thin ring at the outer edge of the directly transmitted beam, plus a small portion of the scattered beams, can be collected to form an image of the specimen. A specially designed thin annular detector (TAD) with only about 10% difference between the inner and outer collection angle can also be used to obtain TAD images. The TAD can be used to form bright-field (TADBF) or dark-field (TADDF) images [53–54]. By applying the principal of reciprocity, this imaging mode is equivalent to hollow-cone illumination in TEM. Detailed treatment of the imaging process suggested that the resolution of TADBF images can be improved [53–54].

The TAD imaging modes take advantage of selecting the range of frequencies that give higher image resolution and excluding the lower frequencies that contribute to background signal. The TAD may also be used to collect signals of small-angle scattering to produce images of amorphous materials or light-element particles. For example, carbon nanoparticles supported on amorphous silica can be detected with good con-

trast [55]. The combination of TAD with HAADF imaging technique can be very effective in examining both heavy-element and light-element nanoparticles with atomic resolution.

Other specially configured detectors can be constructed to increase image resolution, to enhance image contrast, or to extract unique information about certain features of the sample [56, 57]. For example, circular detectors splitting into halves or quadrants have been used to study magnetic field and magnetic domain structures of thin films and small particles [58, 59]. Complicated multiple detectors have also been proposed for special purposes.

4.3.7 Size measurement and distribution of nanoparticles

It is often a challenge to accurately determine the exact sizes of particles with diameters < 1 nm, highly dispersed on supporting materials. Because of the strong phase and diffraction contrast of the supports, it is even difficult to recognize particles of sub-nanometer sizes in HRTEM images. However, the knowledge of this class of nanoparticles is important for understanding nanoparticle systems. For example, the catalytic properties of supported metal catalysts are directly related to the size and spatial distribution of the metal particles.

Although nanoparticles can be observed in high-resolution HAADF images, particles with sizes comparable to the size of the incident probe cannot be reliably measured. Because of the convolution of the probe with the real dimensions of the particles, particles with sizes smaller than the size of the electron probe may give similar sizes in HAADF images.

Because of the incoherent nature of HAADF imaging, the signal strength of high-angle scattered electrons from an isolated small particle is proportional to the total number of atoms in that particle. In principle, the integrated intensity of a particle in a HAADF image is independent of the probe size, the defocus value, and the substrate thickness. It only depends on the type of atoms, the total number of atoms in the particle, and the total current of the incident probe. In practice, however, the presence of noise in HAADF images affects the accurate measurement of the total integrated image intensity of a particle.

Quantification of the intensity distribution of HAADF images of metal particles can be accomplished by image processing techniques [20]. By measuring the integrated intensity, I_1, associated with the N_1 pixels of a particle and I_2 associated with an expanded area of N_2 pixels, the net integrated intensity I_{total} due to only the particle is given by:

$$I_{\text{total}} = \frac{I_1 N_2 - I_2 N_1}{N_2 - N_1} \tag{4-13}$$

In the incoherent imaging limit, the total integrated image intensity of a particle in a HAADF image is proportional to the probe current and the total scattering power of the particle. The signal strength of high-angle scattered electrons is linearly dependent on the number of atoms of each type within the probed volume, weighted by their scattering cross-sections. Assuming the radius of a spherical particle is R, then we can write $I^{1/3} = \alpha R + \beta$. The parameter α is proportional to $(\sigma/\Omega)^{1/3}$; β is a parameter related to the microscope and the noise level introduced in the image acquisition and analysis processes; σ is the atomic scattering cross-section; and Ω is the atomic volume [20].

In the absence of image noise, the total scattering strength of a particle should be independent of the size of the integration area and is not sensitive to lens aberrations or beam defocus. This unique property makes the intensity integration method a much more powerful technique than the conventional sizing methods that rely on diameter or area measurements. Diameters measured in HRTEM images can change in a complicated way with defocus and substrate thickness, especially for particles with a sub-nanometer size [51]. In practice, however, particle visibility in HAADF images change with beam focus. Low signal-to-noise ratio is another limiting factor for measuring small particles. The intensity measurement technique is sensitive to noise, either intrinsic to the specimen or generated from the image-acquisition system [20].

With clean metal particles supported on thin carbon films, the measurement of the total integrated intensity of individual metal particles can be easily performed through a simple intensity-threshold process. Figure 4-16 shows an intensity$^{1/3}$-radius plot from the HAADF signal of silver nanoparticles. The plot lies on a straight line with a slope of α which is related to the intensity increment per atom and the particle morphology. The number of atoms per cluster can be estimated from the intensity$^{1/3}$-radius plots [20].

Because of the extremely complex structures of supports and nanoparticles in practical systems, it is a formidable task to obtain the true integrated intensity of a nanoparticle. Higher beam current densities and smaller probe sizes are preferred to increase the signal-to-noise ratio of particles with sub-nanometer sizes. Sample movement, decomposition, and damage due to intense electron beam irradiation, will all affect the accuracy of the intensity measurement. Sample contamination may also render complications in determining the true signal strength of individual nanoparticles. Sophisticated image analyses are usually needed to subtract uneven background signals before performing particle size and intensity measurement (Fig. 4-17).

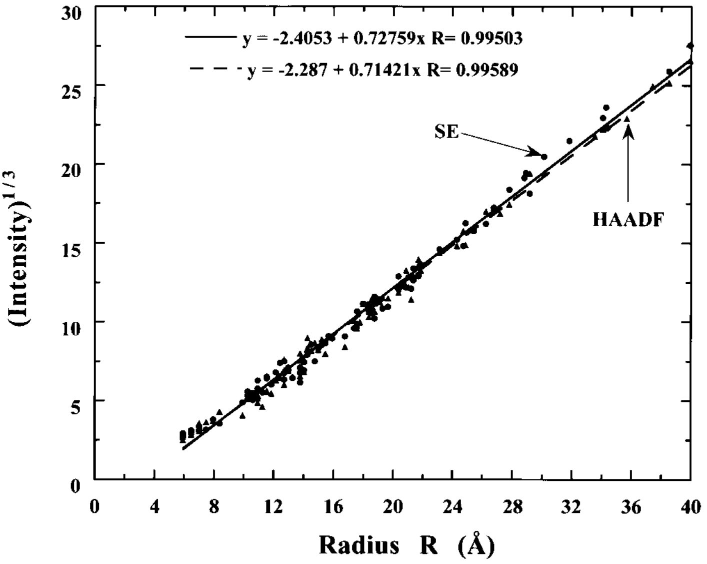

Figure 4-16. Intensity and radius data from particles in HAADF and SE images of silver nanoparticles plotted as (intensity)$^{1/3}$ against particle radius R. The HAADF and SE images were simultaneously collected.

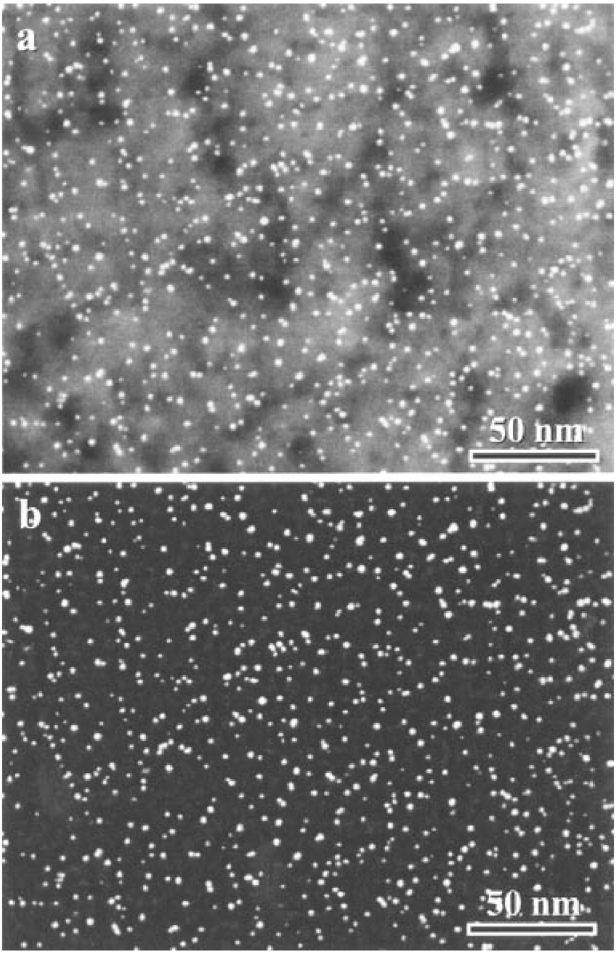

Figure 4-17. HAADF image (a) of Pt nanoparticles dispersed on highly activated carbon support shows small Pt particles with a bright contrast, and intensity variations of the carbon support. The background-subtracted image (b) shows a much "cleaner" image for size and intensity measurement of individual Pt nanoparticles.

In principle, the intensity-size plot could be used to give accurate size distributions of particles, to distinguish between raft-like and spherical particles, and to give information about alloys of different compositions. Although this technique has been used to assess compositional variations in bimetallic nanoparticles, the interpretation of intensity-size plots is much more complicated [60].

4.4 Coherent electron nanodiffraction

When an electron nanoprobe is stopped at any point of interest on a sample, a convergent beam electron-diffraction (CBED) pattern is formed on the detection plane of a STEM instrument. The size of the diffraction discs is determined by the conver-

gent angle of the incident electron probe. With a two-dimensional detector such as a phosphor screen or a CCD system, the diffraction patterns can be observed, recorded, and analyzed in the same away as CBED patterns obtained in TEM instruments [53, 61–62].

The use of a field-emission gun in STEM, however, introduces important new features in STEM CBED patterns [61]. First, the sizes of the electron probes are usually 1 nm or less in diameter, much smaller than those used in TEM. Thus, the diffraction patterns obtained in STEM are usually called micro- or nano-diffraction patterns. Secondly, the use of a field-emission gun warrants the coherent nature of a convergent nanoprobe: the illuminating aperture is filled with completely coherent radiation, and the final probe entering the specimen can be treated as perfectly coherent. In contrast, the illuminating aperture in conventional TEM is considered incoherently filled and the illumination is treated as completely incoherent.

Coherent electron nanodiffraction (CEND) is the only technique that gives full diffraction information about individual nanoparticles. Figure 4-18 shows a schematic diagram illustrating a coherent, convergent electron probe with a size smaller than the size of a multi-faceted nanoparticle. Diffraction patterns from the various parts of the nanoparticle can be obtained to give information about the structure as well as the morphology of the nanoparticle.

Although CEND patterns obtained in a STEM instrument are necessarily CBED patterns, different operating modes of STEM require different incident beam convergent angles. The spatial distribution of the electron probe depends on the convergent angle of the incident beam. For example, high-resolution lattice imaging requires the smallest electron probe and overlapping diffraction discs; thus, a large convergent angle of the incident probe is used to satisfy these conditions. On the other hand, it is necessary to use a small convergent angle to obtain sharp diffraction spots from small particles or localized crystal defects. If we denote the convergent semi-angle of the incident probe as α and the Bragg angle of a crystal as θ_B (Fig. 4-19), then three distinctive types of CEND patterns need to be discussed: 1) $\alpha \leq \theta_B$; 2) $\alpha > \theta_B$; and 3) $\alpha >> \theta_B$. In the following, we will discuss each type of the diffraction pattern in detail.

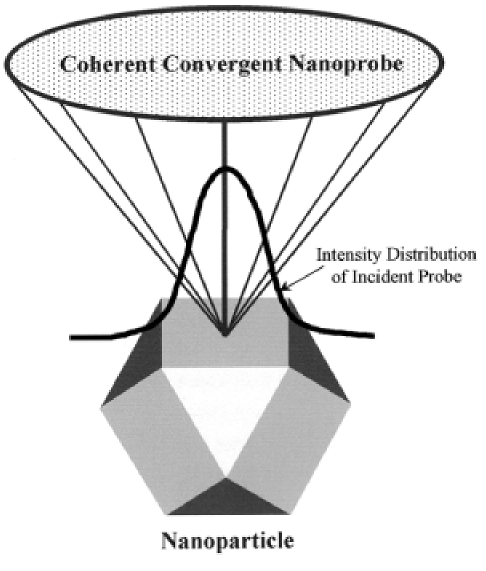

Figure 4-18. Schematic diagram illustrates a coherent, convergent electron probe with a size smaller than the size of a multifaceted nanoparticle. Nanodiffraction patterns from the various facets of the nanoparticle can be obtained to give information about the structure as well as the morphology of the nanoparticle.

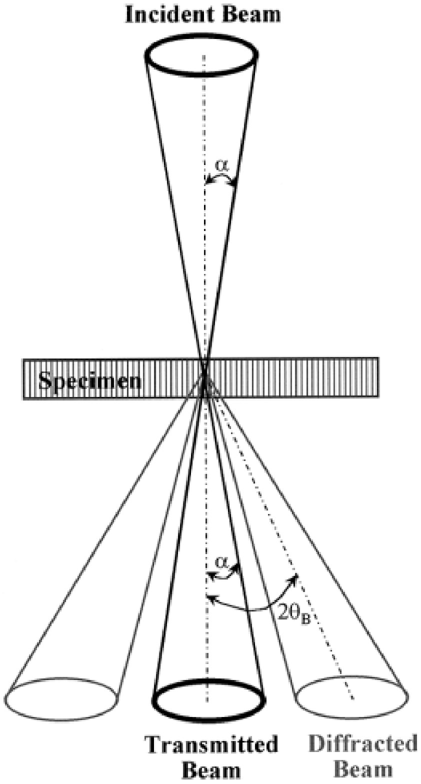

Figure 4-19. Schematic diagram illustrates coherent electron nanodiffraction from crystalline materials: α is the convergent semi-angle of the incident beam; θ_B is the Bragg angle of a diffracting plane.

4.4.1 Coherent electron nanodiffraction with $\alpha \le \theta_B$

4.4.1.1 Perfect crystals

For an ideally perfect, thin crystal (no thickness variation, no defects, no bending), there are no differences in the diffraction patterns obtained with a coherent or an incoherent electron beam if the diffraction discs do not overlap ($\alpha \le \theta_B$ in Fig. 4-19). This is a consequence of the Bragg law: for each incident direction of the electron beam only scattering through mutiples of the Bragg angle is allowed. Thus, electrons with different incident beam directions cannot interfere with each other although the incident electron probe is completely coherent. If the crystal is thicker, the intensity distribution within the diffraction discs may become non-uniform, with sets of lines, bands, or more complicated shapes [62]. This is mostly due to dynamical diffraction effects giving a variation of the incident and diffracted beam intensities as a function of the angle of incident beam. If we ignore the fine-details present in CBED patterns, CEND patterns can be treated the same way as those generated by an incoherent electron beam with a nanometer-size probe. CEND patterns from perfect crystals can be interpreted the same way as CBED patterns obtained in conventional TEM [62].

4.4.1.2 Imperfect crystals

For crystals containing defects (crystal edges and bending, stacking faults and dislocations, thickness variations, and other defects), elastic diffuse scattering from these defects can coherently interfere with each other or with Bragg diffracted electrons. Different patterns, characteristic of the nature of the defects, can be observed. For thicker or strongly scattering samples, any discontinuity in the sample can have some observable effect on the CEND patterns.

For example, when a nanoprobe approaches a straight edge of a MgO cube aligned along the [001] zone-aixs, first the central transmitted disc shows strong streaking towards the crystal; then diffraction spots appear at non-Bragg positions (Fig. 4-20). Fine structures in these CEND patterns change rapidly with the movement of the probe position. The streaking of the central transmitted spot is attributable to the influence of the crystal inner potential. The interference among waves arriving from different incident beam directions gives rise to perturbations of the Bragg diffraction spots. When part of the incident probe is positioned inside the MgO crystal, electrons with different incident directions interact with different parts of the crystal. The scattered electrons interfere with each other to give a characteristic diffraction pattern related to the position of the electron probe. Dynamical diffraction simulations show that the intensity distributions in CEND patterns are sensitive to the surface or the defect structures of the sample [63]. A surface channeling effect may also be responsible for the fine features observed in CEND patterns from straight edges of small crystals [63].

When the incident probe is positioned near the edge of a crystal, CEND discs may show annular rings or splitting of diffracted spots [64]. Internal discontinuities, such as fault planes, out-of-phase boundaries, and thin layer precipitates, may give character-

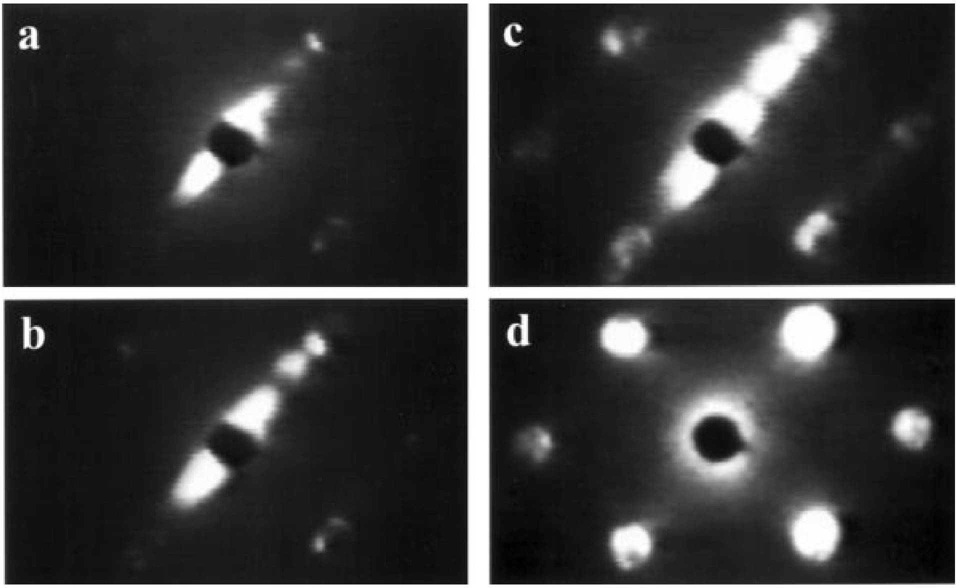

Figure 4-20. Nanodiffraction patterns obtained with an electron nanoprobe (~ 0.8 nm in diameter) moving toward a large MgO cube oriented along the [001] zone axis. The electron nanoprobe was right outside (a) and inside (d) the MgO cube. The black spot represents the center of the directly transmitted electron beam.

istic structures in their corresponding CEND patterns. For example, CEND patterns from antiphase domain boundaries in ordered alloys show spot splitting of superlattice reflections [65].

One of the important applications of CEND is the structural study of metal particles in supported catalysts [21, 66–69]. Other applications of CEND include study of empty and filled carbon nano-tubes [70], precipitates in metals and alloys [71], phase separation in magnetic materials [72], and local ordering in thin films.

4.4.1.3 Small particles

Small particles have peculiar chemical and physical properties compared to their corresponding bulk materials. Metallic nanoparticles are especially important in heterogeneous catalysis; they are primarily the active components of supported metal catalysts. A precise knowledge of the size, structure, and composition of metal particles is of primary importance in understanding the synthesis-structure-activity relationships and is essential for a qualitative and quantitative understanding of the performance of supported metal catalysts.

One of the successful applications of STEM techniques is the ability to analyze the structure and composition of individual nanoparticles. Figure 4-21, for instance, shows a set of CEND patterns, obtained with an electron beam of approximately 1 nm in diameter, of a bimetallic catalyst containing noble metals supported on zeolite crystals which are connected by alumina binders. These CEND patterns provide information about the crystallographic structure of the bimetallic particles and supports, and information about the structural relationship between the metal particles and their supports or binder materials.

It is, however, impossible to make accurate measurements of lattice parameters in CEND patterns because of the large sizes of the diffraction spots. An error of 5% or higher is common in determining lattice constants of small particles, and much larger errors can frequently occur because of coherent interference effects.

It is important to correlate the characteristic features of CEND patterns to particle properties, such as the structure of the particle, the nature of defects within the particle, and the shape and size of the particle. A frequently observed characteristic feature is the splitting of diffraction spots along certain crystallographic directions (Fig. 4-21). The spot splitting in non-overlapping CEND patterns is attributable to the coherent nature of electrons diffracting from an abrupt discontinuity of the scattering potential at particle edges [64]. It is also observed that the spot splitting is related to the geometric forms of the diffracting particles; some splitting occurs in a well-defined crystallographic direction. Depending on the probe position relative to the center of a particle, annular rings may be observed in CEND patterns of small particles [64].

Dynamical simulations reveal that for a particle which has facets smaller than the size of the incident probe, the incident electrons may interact with several facets of the small particle [73]. The thickness of the particle may vary rapidly even within a region of only about 1 nm in diameter. The electron probe effectively interacts with the "particle morphology" under illumination. The intensity variations of the splitting spots are related to the probe positions with respect to the particle facets and are related to the length of the facets along the incident beam direction.

The direction of spot streaking or splitting is directly related to specific edges or facets of a small particle [73]. Furthermore, the intensity profiles across the splitting spots vary with the types of particle wedges. In principle, it is possible to deduce the 3-dimensional structure of nanoparticles by quantitatively analyzing the intensity distri-

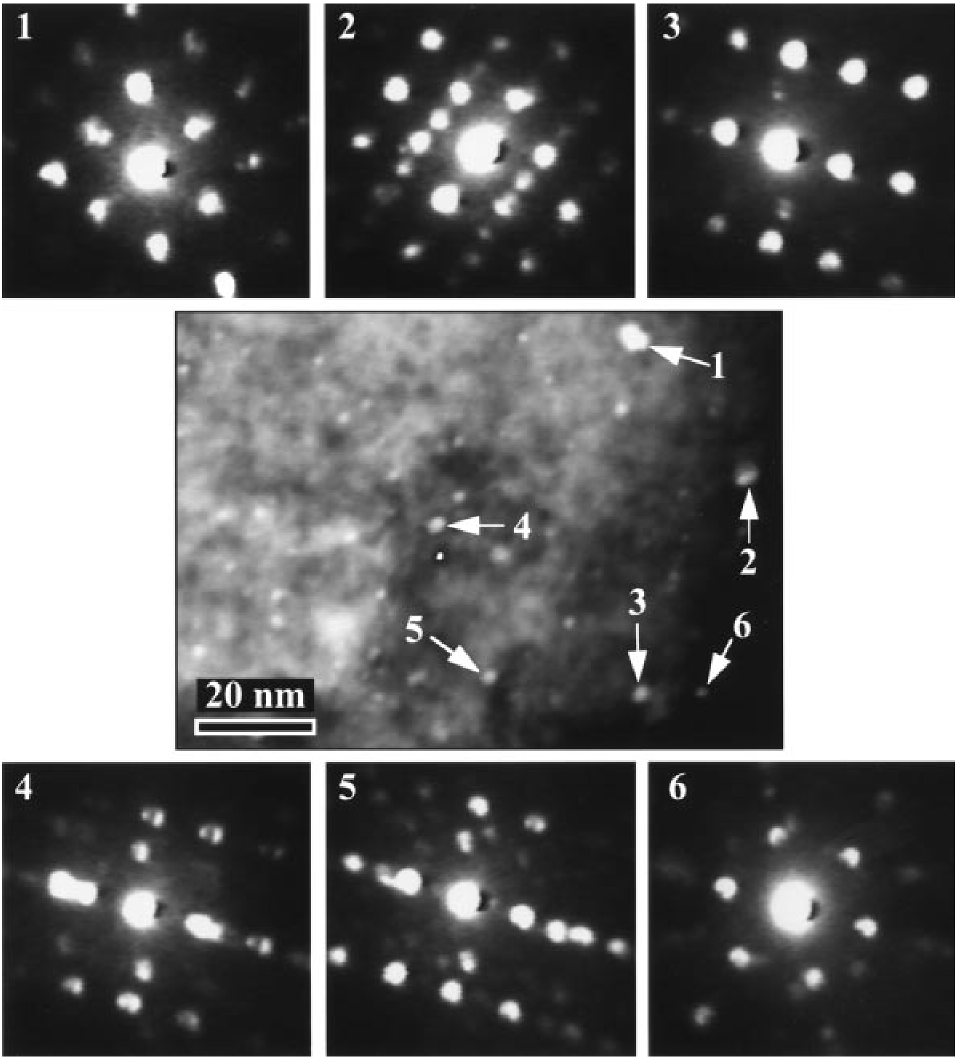

Figure 4-21. HAADF image of bimetallic particles supported on zeolite crystallites connected by alumina binders and electron nanodiffraction patterns obtained from the six nanoparticles labeled in the HAADF image. Some of the diffraction spots are clearly split along certain crystallographic orientations (spot splitting in the diffraction patterns # 3 and # 4).

butions of their CEND patterns. Before this technique can be effectively and reliably utilized to extract the sample information coded in CEND patterns of small particles, many experimental difficulties, such as particle stability, contamination, and accurate control of beam defocus, have to be overcome.

When metal atoms aggregate from the vapor phase or in a liquid, they usually form a crystal, having shapes of regular pentagonal bi-prisms or icosahedra (see Chapter 3 for details). Their internal structure is a complex arrangement of five or twenty twinned components. Large metal particles with shapes of cuboctahedron, decahe-

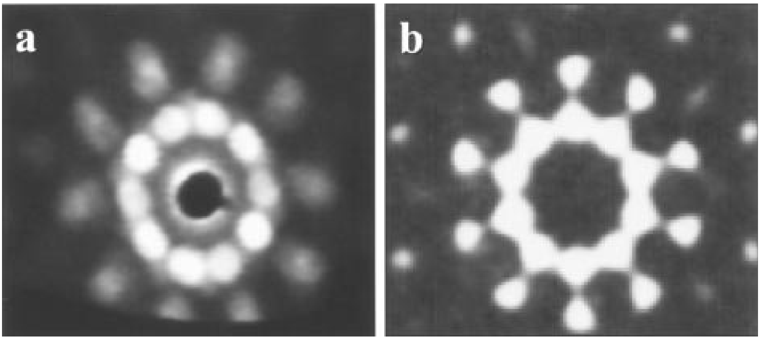

Figure 4-22. Experimental (a) and simulated (b) coherent electron nanodiffraction patterns of a silver nanoparticle with an icosahedral shape. The incident beam was along the five-fold symmetry axis of the icosahedral particle.

dron, icosahedron, and other multiple-twinned structures have been observed [74–76]. For particles with sizes smaller than 2 nm in diameter, however, it is difficult to unambiguously determine their shape by imaging techniques.

CEND technique can provide information about the shape of clean, metallic nanoparticles. For example, a large portion of clean silver nanoparticles with a size smaller than 3 nm in diameter was observed to give unique CEND patterns exhibiting almost five-fold symmetry. These clean silver nanoparticles were formed by in situ deposition in a UHV STEM instrument (MIDAS). Figure 4-22a shows such a CEND pattern and Fig. 4-22b shows a simulated CEND pattern of a small icosahedron with the incident beam direction along the five-fold symmetry axis of the icosahedron. The simulated CEND pattern closely matches the experimental one. These small particles are not stable under intense electron beam irradiation. They rapidly change their orientation and crystal structure [77]. Detailed analyses of CEND patterns recorded on videotapes, however, can provide information about the shape of, as well as the defect structure in, clean nanoparticles.

4.4.2 Coherent electron nanodiffraction with $\alpha > \theta_B$

When the incident electron convergent semi-angle α is larger than the Bragg angle, θ_B, of the diffracting planes, interference effects occur in regions of overlapping discs (see schematic diagrams of Fig. 4-7). In these overlapping regions, the amplitudes of waves from different incident beam directions are added. The phase differences among these waves depend on the values of the transfer function of the probe-forming lens and the relative phases of the specific reflections of the crystal [8]. The phase differences vary with the incident beam position relative to the origin of the unit cell of the crystal. The intensity distribution in overlapping regions becomes sensitive to the probe position and the microscope parameters, such as beam defocus, spherical aberration coefficient of the objective lens, and stability of the microscope. Lattice images can be obtained by placing a STEM detector in the overlapping regions (see Section 4.3.3).

It is possible to determine the detailed atomic arrangement at the core of a defect by coherent overlapping CBED technique [78, 79]. These CBED patterns can also be used to determine the local symmetry of a crystal [80]. In principle, analysis of the

intensity distributions in all overlapping regions of the diffraction pattern should provide information about the relative phases of all diffracted beams, the basis for unambiguous structure analysis of crystals.

A new technique for determining atomic positions using a series of coherent CBED patterns from overlapping regions has been developed; auto-correlation functions are computed for each probe position, giving atomic coordinates with an accuracy of 0.02 nm [5]. However, the most frequent use of these overlapping diffraction patterns is for the final stages of lens alignment and a stigmatism correction of the objective lens for high-resolution STEM imaging [81].

When the convergent angle of the incident beam is made even larger, the diffraction discs overlap at any point of the CEND pattern so that individual discs are no longer visible. The coherent incident beam may have a central peak smaller than the projection of the unit cell of a crystal. The CEND pattern depends on the symmetry and the structure of only that small portion of the projected potential. The intensity distribution of the whole diffraction pattern changes as the beam is moved across the unit cell of the crystal. The changes of intensity and symmetry in CEND patterns can also be observed when an incident beam is scanned across localized defect [79]. By comparing the intensity variations of CEND patterns across crystal defects to those simulated by using many-beam dynamical theory, it is possible to deduce the nature of localized defects in crystalline materials [78, 79].

Recent experiments performed in FE-TEM instruments have demonstrated distortion-free interference fringes in coherent CBED patterns with a lattice spacing < 0.13 nm [82]. The phases of crystal structure factors can be determined from the relative positions of the interference fringes [83]. This coherent interference technique has been applied to the investigation of glide planes, stacking faults, and other defects in crystalline materials [82, 84].

4.4.3 Coherent electron nanodiffraction with $\alpha >> \theta_B$

When the convergent semi-angle of the incident beam is much larger than the Bragg angle of the crystal, the diffraction discs are no longer identifiable, and a point projection image of the specimen is formed on the diffraction plane. In practice, this condition corresponds to using a very large objective aperture or no objective aperture at all. In the absence of spherical aberration, this projection image would be a direct representation of the object transmission function with a resolution determined by the effective probe size. The magnification of projection images is inversely proportional to the beam defocus [61]. The effect of the spherical aberration of the objective lens is to introduce distortions in projection images [81, 85]. These distortions become severe when the in-focus position is approached [85].

For a thin crystal, a special type of projection image, called electron Ronchigram, can be observed in the diffraction plane (Fig. 4-23) [81, 85]. These patterns are called electron Ronchigrams because the geometry used to obtain them is identical to that used in testing optical lenses and mirrors [86]. Electron Ronchigrams can be conveniently used to measure the spherical aberration coefficient and the defocus value of the objective lens [85]. At large defocus values, projection images are similar to low magnification TEM images.

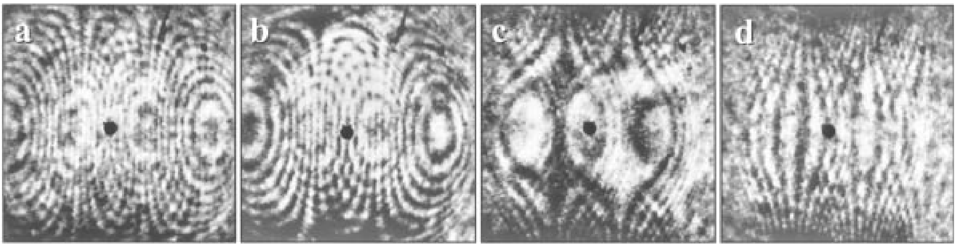

Figure 4-23. A through-focus series of electron Ronchigrams from under-focus (a) to over-focus (d), obtained from a thin GaAs crystal.

A projection image formed by a point source distance Z from an object produces an identical image to that produced by a plane-wave illumination on a plane at a distance Z beyond the object. When a thin crystal is oriented along a principle-zone axis, a slightly defocused projection image can give two-dimensional lattice fringes representative of the projected crystal structure.

With the correction of lens aberrations, increased stability of the microscope parameters, and smaller incident probe sizes, we should be able to study the local structure of crystals in projection images without using any lenses or scanning systems.

Point projection images formed in STEM are exactly the in-line electron holograms proposed by Gabor: in-line holograms could be recorded and used to reconstruct the object wave [87–88]. Gabor suggested that if the reconstruction could be done with an optical system with appropriate aberrations, the effect of the aberrations on the original electron optical images could be corrected and the resolution of the electron microscope could be enhanced. Initial attempt to reconstruct the object function using digitally recorded holograms in a computer has shown limited success [89].

For greatly defocused projection images, an off-line electron holography technique can be effectively utilized to extract quantitative information about the magnetization in small magnetic particles with a nanometer resolution [90–91].

4.5 Imaging with secondary electrons

High-energy electrons impinging on a solid sample experience elastic scattering by atomic nuclei and inelastic scattering by sample electrons. Inelastic scattering results in the transferring of energy from the high-energy electrons to the sample electrons. Thus, specimen-specific electrons can be excited to high-energy states. Some of the excited electrons travelling to the sample surface can be emitted out of the sample as secondary or Auger electrons. By collecting these low-energy electrons, high-resolution surface images can be obtained to give morphological information about the sample (Fig. 4-4). In the following, we will discuss the emission and collection of secondary electrons, the resolution and contrast of SE images, and the application of the SE imaging technique to the characterization of nanoparticles.

4.5.1 Emission of secondary electrons

Electron-induced SE emission is a complicated process and is not well understood. Nevertheless, the emission of secondary electrons from a solid sample can be described as a three-step process: generation, transportation, and emission.

The generation of internal secondary electrons is directly related to the electron energy-loss processes of high-energy incident electrons that undergo a series of inelastic scattering events with an average energy loss of about 20 eV per event. The main energy-loss peaks are usually associated with the generation of plasmons, the direct excitation of outer-shell electrons, and the excitation of core electrons [92]. Secondary electrons can be generated via plasmon-decay or electron-electron scattering processes. The relative contribution of each generation process to the total number of internal secondary electrons depends on the properties of the material under study as well as the energy of the primary incident electrons. The number of secondary electrons generated inside a solid is often regarded as proportional to the stopping power (total energy loss per unit path length) of the incident electrons [93–94]. The relative importance of plasmon-decay processes in the SE production has also been emphasized for conducting materials [95–96].

The internal secondary electrons thus generated interact with different components of the sample such as electrons, phonons, etc. During their diffusion through the solid, the internal secondary electrons can be scattered both elastically and inelastically. Elastic scattering modifies their angular distribution while inelastic scattering changes their energy distribution. The scattering processes of secondary electrons can be best described by a multiple scattering or diffusion theory of low-energy electrons in solids [96–99]. This diffusion process of internal secondary electrons is also called the cascade process of SE transportation.

Only a small fraction of the internal secondary electrons may reach the sample surface because of elastic and inelastic scattering processes. Those secondary electrons that can surmount the energy barrier (work function) at the sample surface can be emitted out of the sample to become detectable secondary electrons. The final emission process is sensitive to the surface properties of the sample such as work function, surface adsorbates, thin layer deposition, sample contamination, surface charging, etc.

The current density of emitted secondary electrons depends on the initial inelastic scattering events, the decay processes of the initial excitations, the transport of low-energy electrons through the sample, and the work function and modifications of the sample surface.

4.5.2 Detection of secondary electrons

In a STEM instrument, a specimen is usually placed inside the pole pieces of a highly excited objective lens. The emitted secondary electrons first experience a strong magnetic field before being collected by an SE detector. Due to the effect of the magnetic field, an emitted SE spirals in a cyclotron orbit with a radius R that depends on the energy and the emission angle of the SE, and the strength of the magnetic field. When secondary electrons travel up or down the optic axis of the microscope, their emission angles are compressed. After spiraling out of the bores of the objective lens, secondary electrons are collected by an SE detector through a transverse electric field. Because of the effect of the magnetic field on the trajectory of the

emitted secondary electrons, the collection efficiency of secondary electrons in a STEM instrument is much higher than that in a conventional scanning electron microscope.

The collection efficiency of low-energy electrons can be further enhanced by the use of electron "parallelizers" located inside the bores of the objective lens [100–101]. The "parallelizers" provide a magnetic field that is strong enough to keep low-energy electrons moving in a small spiral trajectory and traveling out of the bores of the objective lens. The detection efficiency of low-energy electrons in such systems can be significantly increased [100].

The energy distribution of the collected secondary electrons can be analyzed by a low-energy electron spectrometer. Secondary electron spectroscopy (SES) can be used to investigate the energy distribution of secondary electrons from different materials; to measure work function of solid samples; and to study the charging effects of non-conducting materials [102–103]. Localized SES spectra also give information about the nature of high-resolution SE imaging. High-resolution SES has been used to investigate SE emission processes from metals, semiconductors, and insulators [52, 104–106].

Figure 4-24 shows a SES spectrum obtained from a small MgO cube. Since the onset energy of the secondary electrons does not shift from the zero value, we can conclude that there is no observable charge-up of this particular crystal although MgO is an insulator. Furthermore, the SES spectrum shows that more than 90% of the emitted secondary electrons have energies < 5 eV. Secondary electrons emitted from clean, non-charging MgO crystals have a maximum intensity at 1.5 eV with full-width-at-half-maximum (FWHM) of about 2 eV. Energy-selected SE imaging can be performed by selecting certain portion(s) of an SES spectrum as an imaging signal to enhance the contrast of specific features or to improve image resolution and surface sensitivity.

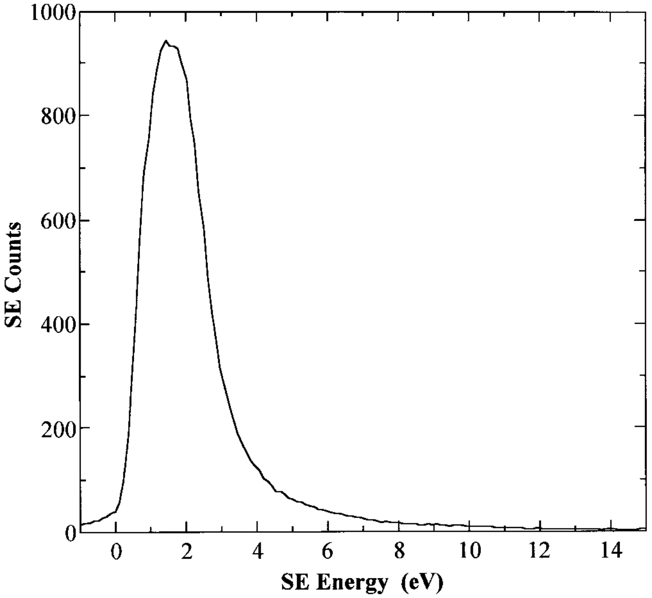

Figure 4-24. High-energy resolution secondary electron spectrum obtained from a small MgO cubic crystal shows that more than 90% of the collected secondary electrons have energies less than 5 eV.

4.5.3 Resolution and contrast of secondary electron images

There are two types of secondary electrons emitted at the surface of a sample. Secondary electrons that are directly generated by the incident beam are termed SE1 and those that are generated by backscattered electrons are termed SE2. Signals of SE1 and SE2 cannot be distinguished from their energy or angular distributions. Depending on the incident beam energy and the type of samples under investigation, the total signal strength of SE2 can be stronger than that of SE1.

The resolution of SE images depends on the rate at which the signal changes as the probe is scanned across a sample. The contrast of SE images depends on the relative intensity variations among different probe positions. Therefore, both the resolution and the contrast of SE images depend on the local current density of the emitted secondary electrons. With very small probe sizes, the spatial distributions of SE1 and SE2 determine the image contrast and resolution.

In a STEM or a field-emission SEM instrument, the current density of SE1 is much higher than that of SE2, although the total signal strength of SE2 could be stronger than that of SE1 for thick or bulk samples. At high magnifications, the SE2 signal varies much more slowly with the movement of the incident probe than that of SE1, thus SE1 and SE2 signals can be spatially separated. For thin specimens, the contribution of SE2 is usually negligible. The contrast and the resolution of SE images of thin specimens are entirely determined by the spatial distribution of SE1 signals.

Sub-nanometer surface details can be observed in high-resolution SE images [107–111]. This implies that the generation processes of secondary electrons are localized to within 1 nm or less. It was first pointed out and later experimentally proved that the generation of secondary electrons is directly related to large-angle inelastic scattering of the high-energy incident electrons [112–113]. There exist large momentum transfer mechanisms during inelastic interaction processes such as Umklapp or phonon-assisted electron excitation processes. Inelastic scattering events involving these processes are highly localized. The resolution obtainable in SE images is currently limited by the incident probe size to about 0.5 nm.

The contrast in SE images is primarily due to topographic effect, although other contrast mechanisms (material contrast, work function contrast, etc.) may play a role in determining the contrast of SE images of specific samples [93, 112, 114]. Figure 4-25 shows an SE image of a MgO particle revealing surface steps, facets, and the var-

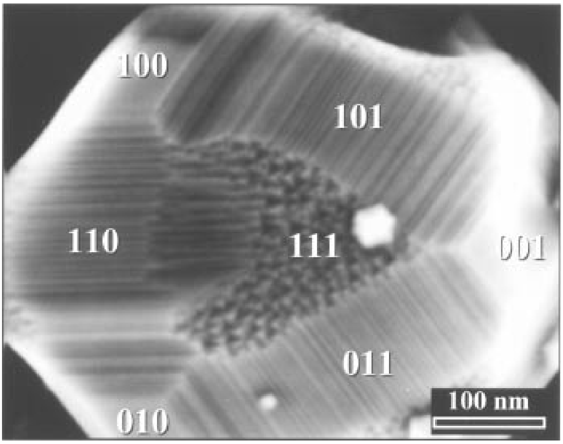

Figure 4-25. High-resolution secondary electron image of a large MgO cube clearly shows flat {001} faces, terraced {011} faces, and the faceted (111) face. The {011} and {111} surfaces are composed of {001} terraces or facets.

ious faces of the incomplete MgO cube. Individual atomic steps can be observed in high-resolution SE images with characteristic black and white contrast for up- and down-steps, respectively [106]. For normal incidence of the electron beam, all steps are shown bright but sharper and fainter. The observed contrast of SE images of surface steps can be explained in terms of SE emission from the steps. The amount of material that generates and emits secondary electrons is greater for down-steps than for a flat surface and is less for up-steps [106].

4.5.4 Image contrast of small particles

When the radius of a small particle becomes comparable to, or even smaller than, the escape depths of secondary electrons, most of the secondary electrons, generated inside the particle, with energies higher than the surface barrier may escape. In contrast, because of the effect of total internal reflection of low-energy secondary electrons, only about 10% of the total internal secondary electrons which have energies higher than the surface barrier can escape from a flat surface. Because of this geometric effect in SE emission, small particles are often observed with a bright contrast in high-resolution SE images (Fig. 4-26) [109, 112].

The SE signal strength of a small particle increases with the size of the particle. Furthermore, for metal particles with a radius much smaller than the average escape depth of the collected secondary electrons, the SE image intensities of these particles follow exactly those of HAADF images. Figure 4-27 shows SE and HAADF intensity line-scans, acquired simultaneously, across small, clean silver nanoparticles. These intensity line-scans clearly show that the SE signal is as localized as the HAADF signal within the resolution limit which is about 0.6 nm in these images. The SE intensity profiles almost overlap those of HAADF signal. In fact, the total integrated SE intensity (I_{SE}) from a small particle is proportional to the volume of that particle. If we plot $I_{SE}^{1/3}$ against the particle radius R, a straight line is obtained (see Fig. 4-16), similar to that of the HAADF signal. Thus, the total integrated SE intensities of small particles are proportional to the volume of the particles.

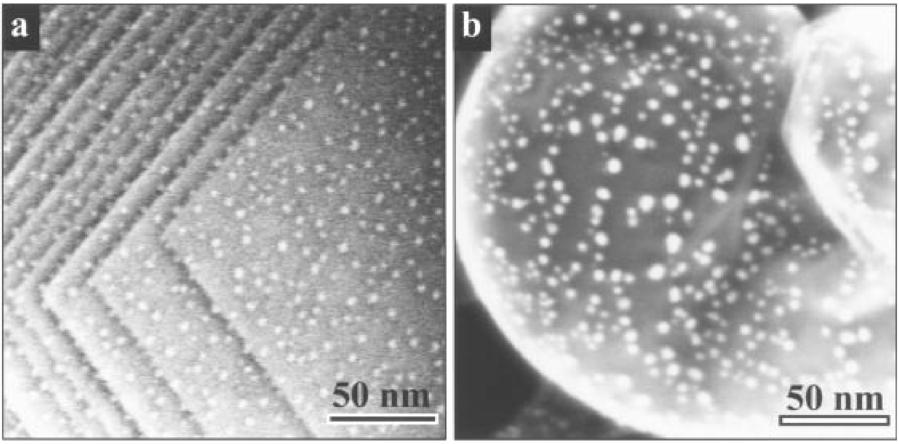

Figure 4-26. High-resolution secondary electron images of silver nanoparticles deposited onto clean surfaces of (a) MgO and (b) α-alumina crystals. Small silver particles are clearly shown with a bright particle contrast.

The particle contrast in SE images can be parameterized by the ratio of the particle radius (R) to the average escape-depth (L) of the collected secondary electrons (Fig. 4-28). If $R/L < 1$, the brightness of a particle increases with the size of the particle and the image intensity has a maximum at the center of the particle. If $R/L > 1$, the particle intensity slowly increases with the size of the particle and the highest image intensity is approximately at a distance $d = (R - L)$ from the center of the particle. For very large particles, the particle contrast evolves into the edge-brightness contrast commonly observed in SE images.

Although the resolution of SE images is comparable to the size of the incident probe, it is impossible to extract information about the shape of nanoparticles with sizes less than the escape depth of the collected secondary electrons. Therefore, we cannot extract information about detailed surface morphology of very small particles. However, we can obtain useful information about the relative locations of nanoparticles with respect to the surface topography of supports (Fig. 4-4).

Because of the use of strong probe-forming lenses and field-emission electron sources, it is possible to obtain SE images with a resolution of about 0.5 nm and 2 nm at 30 kV and 1 kV, respectively. The collection efficiency of secondary electrons in a field-emission SEM is also significantly improved due to the utilization of novel SE detection configurations. It is especially attractive to operate at low electron energies: the increase in signal strength, the reduced volume of electron-specimen interactions, and the neutralization of charging effects for non-conducting materials [115–116]. Other advantages of low-voltage SEM include enhanced surface sensitivity at medium image resolution and reduced radiation damage for delicate samples [115–116]. Metal nanoparticles, as well as detailed surface morphology of supports, can be clearly revealed in low-voltage high-resolution SE images with high contrast and high surface sensitivity (Fig. 4-29).

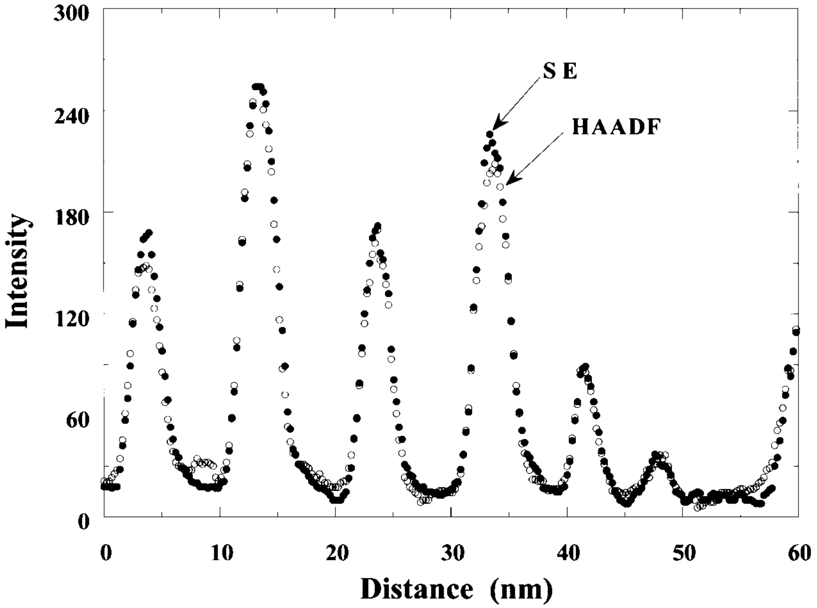

Figure 4-27. HAADF and SE intensity line-scans across silver nanoparticles. The SE intensity line-scan closely follows that of the HAADF signal.

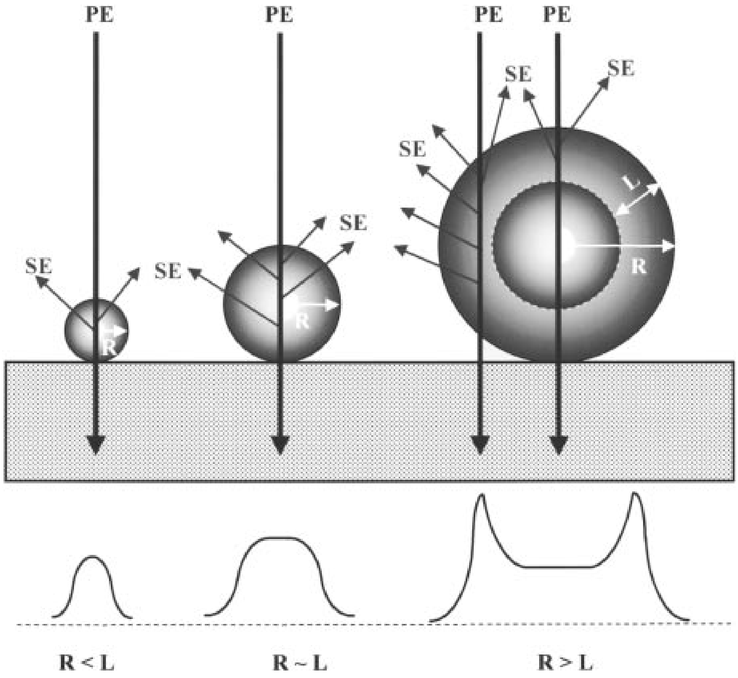

Figure 4-28. Schematic diagrams illustrate the emission of secondary electrons from spherical particles of different sizes and the corresponding SE intensity line-scans across the particles. The parameters *R* and *L* represent the particle radius and the average escape depth of the secondary electrons, respectively.

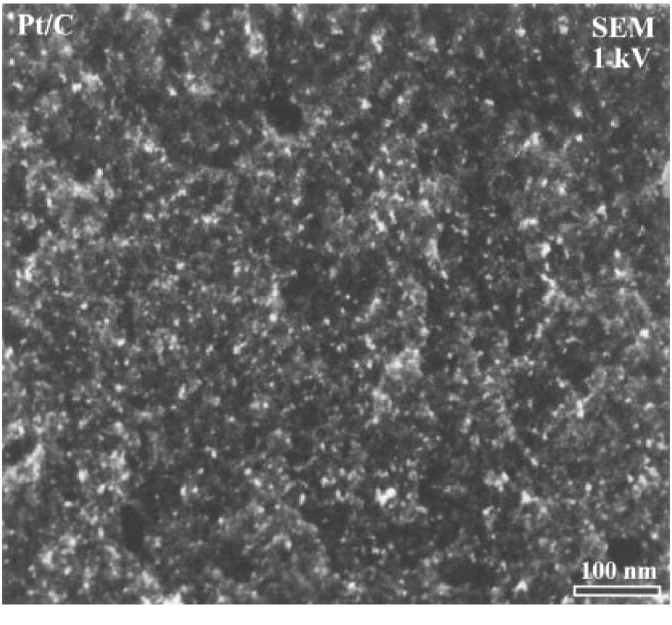

Figure 4-29. Low voltage, high-resolution secondary electron image of Pt nanoparticles dispersed in a highly activated carbon. The Pt particles, as well as the nano-pores of the carbon support, are clearly revealed.

4.6 Imaging with Auger electrons

An atomic inner-shell vacancy produced by the incident electrons can be relaxed through a two-electron process: one electron fills the inner-shell vacancy and the other is emitted from the atom (Fig. 4-30). The emitted electron is called an Auger electron. The energies of the primary excitation and of the emitted Auger electrons are both characteristic of the element(s) involved [117]. The production of Auger electrons is essentially similar to that of low-energy secondary electrons; the initial excitation produced by the inelastic scattering of the incident electrons decays to generate a low-energy electron that can escape into the vacuum. In contrast to the diffusion of secondary electrons, Auger electrons must escape from the specimen surface without losing any energy in order to be registered as Auger peak signals. The reason that Auger electron spectroscopy is a surface-sensitive technique lies in the intense inelastic scattering that occurs for electrons in this energy range. Thus, only Auger electrons generated from the outmost atom layers of a solid can survive to be ejected and measured in the Auger electron spectrum. Most of the emitted Auger electrons are produced within a very short distance from the sample surface, typically 0.3 to 3 nm [118].

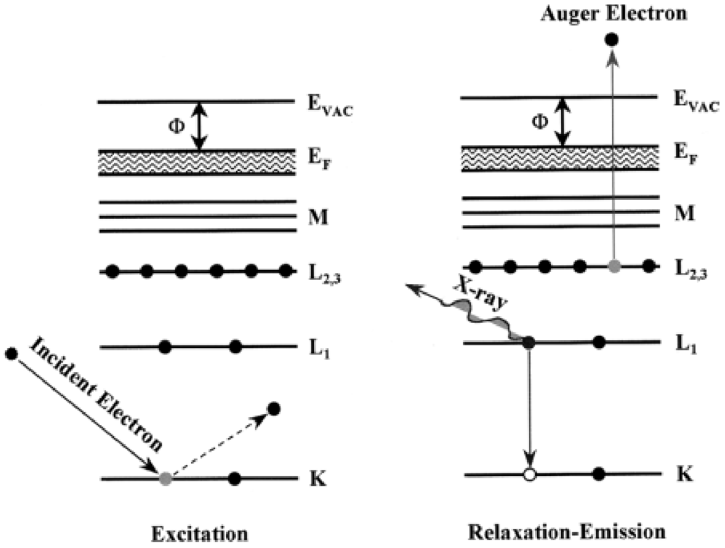

Figure 4-30. Schematic diagram illustrates the emission of characteristic X-rays and Auger electrons from a solid sample. The excitation of a core-level electron can be relaxed either by emission of a photon (characteristic X-ray) or by emission of another electron (Auger electron).

4.6.1 High spatial resolution Auger electron spectroscopy

In a STEM instrument, Auger electrons, emitted from either the entrance or the exit surface of a specimen, can be collected and analyzed using a CMA (cylindrical mirror analyzer) or a CHA (concentric hemispherical analyzer) electron spectrometer. Because of the high-energy and high-brightness of the incident electrons, the employment of magnetic "parallizers", and the use of thin specimens in STEM instruments, high-quality Auger electron spectra can be acquired with extremely high peak-to-background ratios [119–121]. Figure 4-31a shows a high-energy resolution AES spectrum of clean silver nanoparticles supported on a thin carbon film; the silver MNN doublet is clearly resolved. The sizes of the silver nanoparticles range from 1 to 5 nm in diameter.

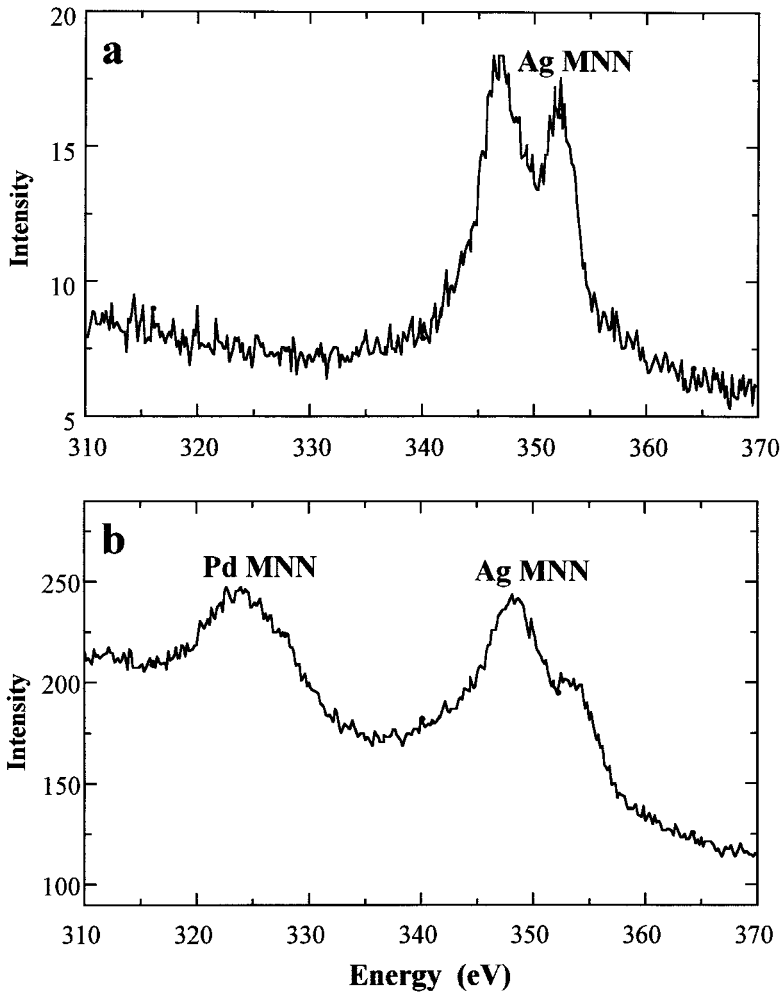

Figure 4-31. Auger electron spectra obtained in a UHV STEM instrument (MIDAS): (a) high-energy resolution MNN Auger electron spectrum of silver nanoparticles; (b) Auger electron spectrum obtained from Ag/Pd bemetallic particles.

Surface compositional analysis of individual nanoparticles is essential for understanding the activity and selectivity of industrial bimetallic or multi-component catalysts used in a variety of chemical reactions. The overall composition of these individual nanoparticles can usually be obtained by the use of high spatial resolution XEDS (see section 4.7). It is, however, extremely difficult to extract information about preferential surface segregation or aggregation of individual components in nanoparticles of different sizes. Because of the high-surface sensitivity of Auger electrons, it is possible to determine qualitatively and, in some cases, quantitatively, the surface composition of nanoparticles consisting of multiple components. Figure 4-31b shows an Auger electron spectrum obtained from a sample containing palladium, silver, or palladium-silver nanoparticles highly dispersed on a high-surface area support. Both the silver and the palladium MNN Auger peaks are clearly revealed. Quantitative analyses of this type of spectrum can provide information about the surface enrichment of specific elements and information about how this enrichment varies with the size of the particles.

4.6.2 High spatial resolution scanning Auger microscopy

Considerable efforts have been devoted to the development of scanning Auger microscopy (SAM) and the improvement of its imaging resolution since the pioneering work of MacDonald and Waldrop [122]. The driving force for developing high spatial resolution SAM is related to the characterization of nanoparticles and other nano-structured materials. The best resolution of SAM images obtained in conventional SEM geometry is approximately 30 nm under favorable conditions [123–124]. A spatial resolution of about 10 nm can be achieved using the high current density and the small probes of STEM instruments [125]. A similar or better image resolution may also be achievable in the new generation of field-emission SEM instruments. Further improvement in resolution by using smaller electron probes significantly reduces the strength of the collected Auger signal.

With the improvement in the detection efficiency of low-energy electrons in the MIDAS system by employing magnetic "parallelizers" [100], a spatial resolution of $<$ 3 nm in Auger peak images can be obtained on bulk samples [120]. For electron transparent specimens, typically used in STEM instruments, an image resolution $<$ 1 nm can be achieved [121]. Silver nanoparticles $<$ 1 nm in diameter and containing as few as 15 silver atoms can be detected [119, 121].

Metal nanoparticles highly dispersed on supporting materials represent a significant fraction of heterogeneous catalyst systems. Surface chemical information about such systems can be obtained by collecting Auger electrons to form high spatial resolution, elementally specific, and surface sensitive images. Figure 4-32 shows a set of images of a model catalyst consisting of clean silver nanoparticles deposited onto a thin carbon film. Both the silver nanoparticles and the surface details of the support are revealed in the SE image. However, the nano-scale pore structure of the carbon film is clearly revealed in the C KLL Auger peak image with high contrast. The high intensity of the silver particles in the C KLL Auger peak image could occur due to electron scattering processes or because of the high SE background from the silver nanoparticles [121].

The silver nanoparticles are shown with very high contrast in the silver MNN Auger peak image. The silver Auger map, obtained by subtracting the background image from the silver MNN Auger peak image, shows silver clusters as small as 1–2 nm in diameter. The average background pixel value in the silver Auger map is $<$ 3 while the

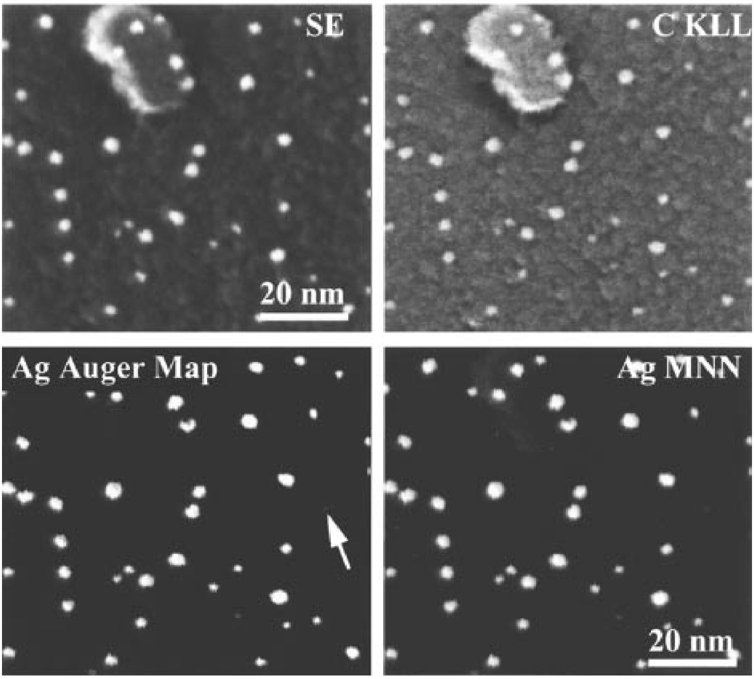

Figure 4-32. A set of images of silver nanoparticles supported on a carbon film: SE image; carbon KLL Auger peak image; silver MNN Auger peak image; and silver Auger map obtained by subtracting a background image from the silver MNN Auger peak image.

smallest silver particles have a pixel value of about 30 at the center of the particle (indicated by the arrow in the silver Auger map). Larger particles have pixel values of about 340 at the center of the particles. Further particle analyses can be performed on this type of "clean" image, yielding information about the size distribution and the composition of the particles. The intensity variations of Auger signals with the sizes of silver nanoparticles can also be investigated.

The digitally acquired Auger peak and background signal images contain quantitative data on the Auger peak height and SE background intensity. Data sets obtained by processing the digital images contain quantitative information about the contrast of the Auger peak and background signal images [121].

The topographic contrast in SAM images of bulk samples can be, in general, minimized by using the algorithm (P–B)/(P+B). Here P represents the signal at the Auger peak and B represents a background signal taken at an energy level just above the Auger peak [126]. Despite the successful use of this algorithm in low resolution SAM images, it cannot be directly applied to nanometer-resolution SAM images. In fact, the (P–B)/(P+B) or (P–B)/B display only enhances the edge contrast since the escape depth of the background signal is much greater than the attenuation length of the Auger electrons [121, 127]. For nanometer-resolution SAM images, the P–B display may best represent the elemental map of the sample surface.

4.6.3 Resolution limit

The resolution in SAM images depends on several sample- and instrument-related effects. The sample-related effects include: 1) surface topography, 2) escape depth of the collected Auger electrons, 3) contribution from backscattered electrons, and 4) localization of the Auger electron production processes. The last factor sets the ultimate resolution limit that will be achievable in SAM images. Since the primary inelastic scattering processes involve excitation of inner-shell electrons, the generation of Auger electrons is highly localized. With thin specimens and high-energy incident electrons, the contribution from backscattered electrons should be negligible. It may, however, degrade the image resolution and affect the image contrast of bulk samples.

The instrument-related effects include: 1) the intensity distribution of high-energy electron probes, 2) the collection efficiency of the emitted Auger electrons, and 3) the instability of the STEM microscopes. The capabilities and limitations of high spatial resolution AES and SAM are discussed in a recent review article [128]. At present, the instrument-related factors set the limits of obtainable resolution to about 1 nm in Auger peak images of thin specimens [121].

4.6.4 Detection sensitivity

Because the Auger electron intensity profile of a particle is a complicated convolution of the electron probe with the real morphology of the particle, the true size of the particle may be smaller than that measured in a SAM image. A de-convolution process might be used to extract the real sizes of the observed nanoparticles. However, knowledge of the intensity distribution of the probe, the radial and angular distributions of the emitted Auger electrons, and the detailed transmission function of the electron analyzer would have to be known.

The emission of Auger electrons from small particles is different from that of flat surfaces. Electrons generated inside a small particle may all escape if the radius of the particle is much smaller than the inelastic mean free path (λ) of the collected Auger electrons. In this limit, the total number of the collected Auger electrons is proportional to the volume of the particle; and the distinction between "bulk" and surface signals is no longer valid. A quantitative estimate of the minimum particle size detectable in SAM images can be developed from a simple relationship between the signal strength and the size of the particle. By using an intensity-ratio method, it is possible to estimate the total number of atoms detectable in high spatial resolution Auger maps [119].

The total integrated signal strength of a small particle, in the absence of image noise, should be independent of the size of the incident electron probes. The integrated intensity (I) of a particle in SAM images is proportional to the total number of atoms (N) which contribute to the collected Auger signal, $I = \alpha N$. The parameter α is dependent on the Auger electron cross-section, detection efficiency, incident beam current, and other instrument-related parameters. However, for each SAM image α can reasonably be assumed a constant.

Thus, the number of atoms contained in a small particle N_1 with an integrated intensity I_1 can be estimated from a large particle with N_2 atoms and an integrated intensity I_2: $N_1 = N_2(I_1/I_2)$. This relationship indicates that a large particle could be used as an internal calibration standard to determine the total number of atoms contained in smaller particles. On this basis, it is estimated that particles containing as few

as 15 silver atoms can be detected in high-resolution SAM images (see Fig. 4-32). At present, the minimum detectable mass in high spatial resolution SAM images is less than 3×10^{-21} g [119].

The minimum detectable dimension is different from the resolution of SAM images [128–129]. While the latter is currently limited by the sizes of the incident electron probe, the former is related to, but not limited by, the dimension of the incident electron probe. The minimum detectable size can be much smaller than the incident probe diameter. The minimum particle size detectable in a SAM image is directly related to the signal-to-noise and signal-to-background ratios, as well as the radiation damage of the sample. For example, the minimum detectable dimension would be the size of a single atom if the signal strength were not a limiting factor, and that the atom were stable under intense electron beam irradiation.

4.7 Nanoanalysis with energy-loss electrons and X-rays

The remarkable capability of forming an electron probe with sub-nanometer sizes in STEM instruments makes it practical to perform chemical analysis with a nanometer or sub-nanometer resolution. When high-energy incident electrons interact with a specimen, a variety of signals are generated from within the interaction volume (see Fig. 4-1). Some of these signals such as characteristic X-ray photons, energy-loss electrons, Auger electrons, and light photons, carry information about the composition or the chemistry of the sample. These analytical signals can be collected and analyzed by appropriate spectrometers to give useful information about the sample.

Unlike microscopy that records the location and distribution of atoms, particles, and phases, spectroscopy is concerned with the measurement of energies or wavelengths of the collected analytical signals. We can transform various spectra into useful data that give information about elemental composition or distribution of different phases in the sample at a nanometer and, in some cases, an atomic resolution. Among these spectroscopic techniques, XEDS and EELS are the two most frequently used analytical techniques in STEM instruments.

EELS is the analysis of the energy distribution of high-energy incident electrons that have been inelastically scattered by the specimen. These inelastically scattered electrons carry important information about the electronic structure of the specimen atoms. Thus, EELS spectra contain essential details of the nature of these atoms, their bonding and nearest-neighbor coordination, charge transfer, and dielectric response (see Chapter 3 for detailed discussions).

XEDS is the analysis of the energy distribution of emitted characteristic X-ray photons, which are related to the excitation of inner-shell electrons of the specimen atoms (Fig. 4-30). The dependence of the emitted characteristic X-rays on the nature of the excited atoms present in a sample provides the basis of nanoanalysis by XEDS. The fundamental principles of XEDS and EELS have been discussed in many textbooks [9, 92, 130–132]. We discuss here only those features that are unique to STEM configurations.

4.7.1 Electron energy-loss spectroscopy

By performing parallel EELS (PEELS) in conjunction with the HAADF imaging technique in STEM, detailed information about the composition, chemistry, and structure of the specimen can be obtained with atomic resolution and sensitivity. This strategy has recently been applied to the study of a variety of materials problems with great success [133–140]. For example, in the study of iron nanoparticles used as a fuel additive to reduce or enhance soot formation during combustion, PEELS gave information about the spatial variation of the oxidation states of iron species within individual nanoparticles 141]. This type of information is extremely important for understanding the role of nanoparticles during catalytic reactions.

Electron energy-loss images, formed by selecting characteristic energy-loss peaks in EELS spectra as input signals, provide information about the spatial distribution of elements or electronic and oxidation states in the specimen [135, 142–143]. For example, energy-loss electrons were used to obtain maps of sp^2 and sp^3 states of carbon at sub-nanometer spatial resolution across the silicon-diamond interface [135]. By analyzing the electron energy-loss images, it was concluded that diamond nucleates on an amorphous carbon layer, with the transition from sp^2 to sp^3 carbon occurring over a distance less than 1 nm. This type of valuable information can only be obtained by using a high-brightness, sub-nanometer electron probe available in STEM instruments.

A recent development in quantitative EELS mapping is the spectrum-imaging technique: acquire and store a spectrum at each pixel in a two-dimensional image [142–144]. A spectrum-image in its most common form is similar to a normal STEM image; but a spectrum-image contains an entire spectrum at each pixel. A spectrum-image can be viewed as a three–dimensional image with two spatial coordinates and one energy coordinate. One of the greatest advantages of the spectrum-image technique is that it can be processed a posterior, thus, offering access to the exact relationship between the spatial coordinates and the spectral feature. Elements in unexpected locations may be found by off-line processing the digitally stored spectra. The major limitations of this technique include acquisition and manipulation of a tremendous amount of spectral data and the time-consuming process of analyzing millions of spectra for each sample. Quantitative EELS imaging is, however, a powerful method for spatial interpretation of elemental, chemical, and other important information related to the physical properties of nanophase materials.

Another unique application of ELLS in STEM is the study of valence excitation processes of high-energy electrons passing through a thin film or a small particle, or passing close to a surface or interface of a solid material [145–149]. Surface or bulk plasmon excitations, inter-band or intra-band single-electron transitions, and defect-induced electronic states can be investigated with a sub-nanometer spatial resolution (see Chapter 3 for detailed discussion on the excitation processes).

EELS technique is ideal for analysis of low atomic-number materials of thin specimens. When a specimen is thicker, plural and multiple inelastic scattering may become dominant and thus obscure the characteristic features of the EELS spectra.

4.7.2 X-ray energy-dispersive spectroscopy

XEDS is now routinely used, in TEM, SEM, or STEM instruments, to identify unknown phases or to obtain information about the spatial distribution of certain phases of interest. In a STEM instrument, XEDS can be conveniently used to analyze

the features revealed in HAADF images by stopping the incident probe at any point of interest. For thin specimens, qualitative interpretation of XEDS spectra can be performed on-line.

A consequence of high spatial resolution in STEM is that the X-ray signal originates from a much smaller volume of the specimen; a weaker signal means long acquisition time in order to obtain statistically meaningful results. Therefore, specimen-drift correction, either manually or automatically, is usually used to collect enough X-ray signals when very small particles are analyzed. Nevertheless, XEDS can detect the presence of just a few atoms if the analyzed volume is small enough [150].

XEDS technique has been widely used to solve materials problems including identifying precipitates in alloys, active phases in supported catalysts, elemental segregation at grain boundaries, and quantitative composition of multi-component phases.

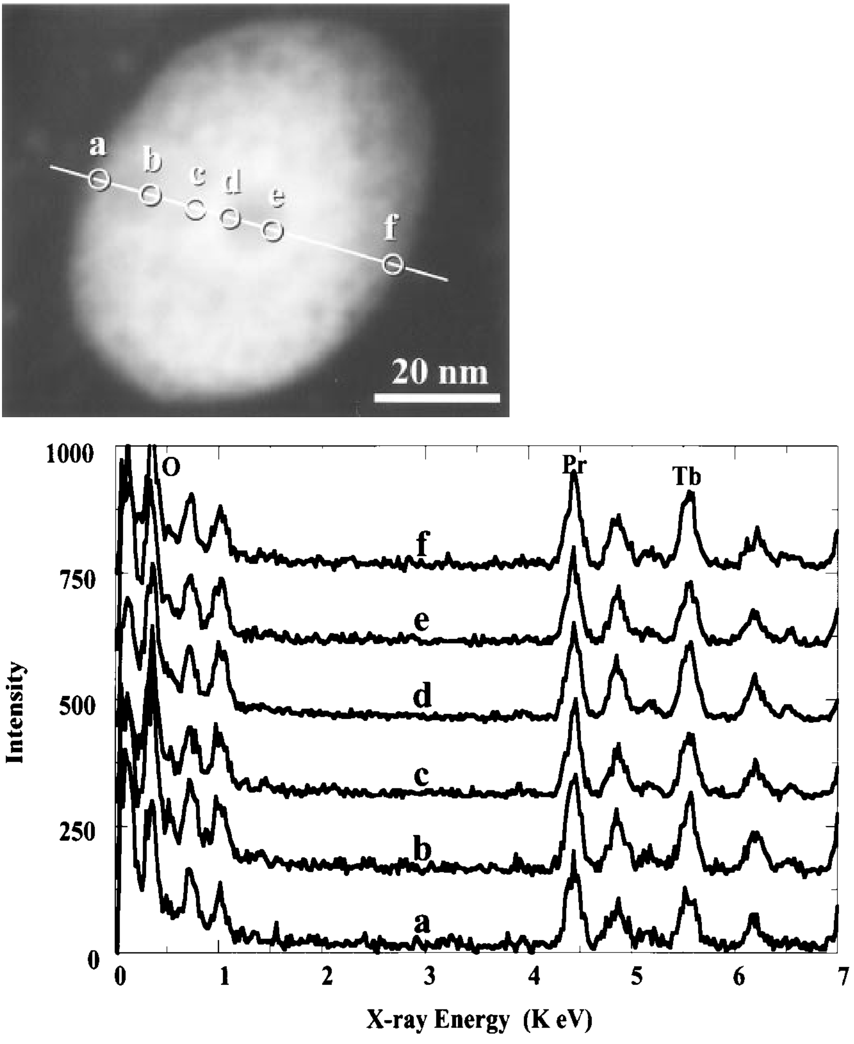

Figure 4-33. Nanoanalysis of a colloidal $Pr_{0.5}Tb_{0.5}O_x$ nanoparticle. The XEDS spectra were obtained from the corresponding locations labeled in the HAADF image.

The combination of qualitative XEDS with HAADF imaging technique is now routinely used in STEM instruments for fast analysis of unknown phases and the spatial distribution of these phases.

In the study of in situ decomposition of hydroxycarbonate ($Pr_{0.5}Tb_{0.5}OHCO_3$) colloidal nanoparticles, it is necessary to understand the chemical homogeneity of the decomposition products within individual nanoparticles. Figure 4-33a shows a HAADF image of one of these nanoparticles after approximately 20 minutes intense electron beam irradiation. To determine the variations in elemental composition across the small particle, a series of XEDS spectra were obtained at different probe positions (Fig. 4-33b). By quantitatively analyzing the XEDS spectra obtained from different particles and comparing these nanoanalytical results with those of HRTEM, a model of the decomposition process and the structure of the final decomposition product were proposed [151].

Similar to EELS mapping, X-ray maps can provide valuable information about two-dimensional elemental distributions in the sample. Particles as small as 2 nm in diameter can be detected in digitally acquired X-ray maps [152]. The ultimate limitation for X-ray mapping of nanoparticles is the extremely low X-ray signal strength although high-brightness field-emission guns are used. The conditions for optimum X-ray mapping include: 1) high beam current with small probe size, 2) high X-ray collection efficiency, and 3) long acquisition times per pixel with specimen-drift correction.

4.7.3 Comparison of nanoanalysis by EELS and XEDS

Both EELS and XEDS are important analytical techniques available in STEM instruments. These two techniques are complementary to each other. EELS is preferable for analysis of light-elements of thin specimens with a sub-nanometer or atomic resolution; XEDS is mostly used for identifying, and determining the composition of, unknown phases composed of heavy-elements. Furthermore, EELS can provide useful information other than just the composition of the sample. Although EELS has a much higher sensitivity than XEDS has for detecting light-elements [153], little useful information can be extracted in the acquired EELS spectra unless the specimen is very thin. Because of the complexity of the experimental procedures and because of the large number of variables related to the acquisition and the subsequent analysis, EELS, however, is not as widely used as XEDS in solving industrial problems.

Qualitative analysis of both XEDS and EELS spectra can be performed on-line. Quantification of these spectra, however, is not straightforward, especially for analysis of nanoparticles. Low signal-to-noise ratio often poses a severe problem for quantitative analysis of XEDS spectra while low peak-to-background ratio in EELS spectra presents difficulties for quantification.

The achievable resolution in XEDS is limited by the size of the incident probe, the spreading of the propagating probe, the signal-to-noise ratio in the spectra, the specimen drift, and the electron beam damage of the sample [154]. The achievable resolution in EELS is limited by the size of the incident probe, the delocalization of the primary excitation processes, the signal-to-background ratio, instrument stability, and electron beam damage of the sample [155]. Under highly favorable conditions, single atoms can be detected in EELS spectra [156]. With special precautions and under optimized conditions, about 10 atoms can be detected in XEDS spectra [150].

4.8 Summary

STEM can be used in various forms to provide useful information about nanoparticles or nanoparticle systems. Surface morphology of the sample can be examined on a nanometer scale by collecting secondary electrons. Nanoparticles can be identified

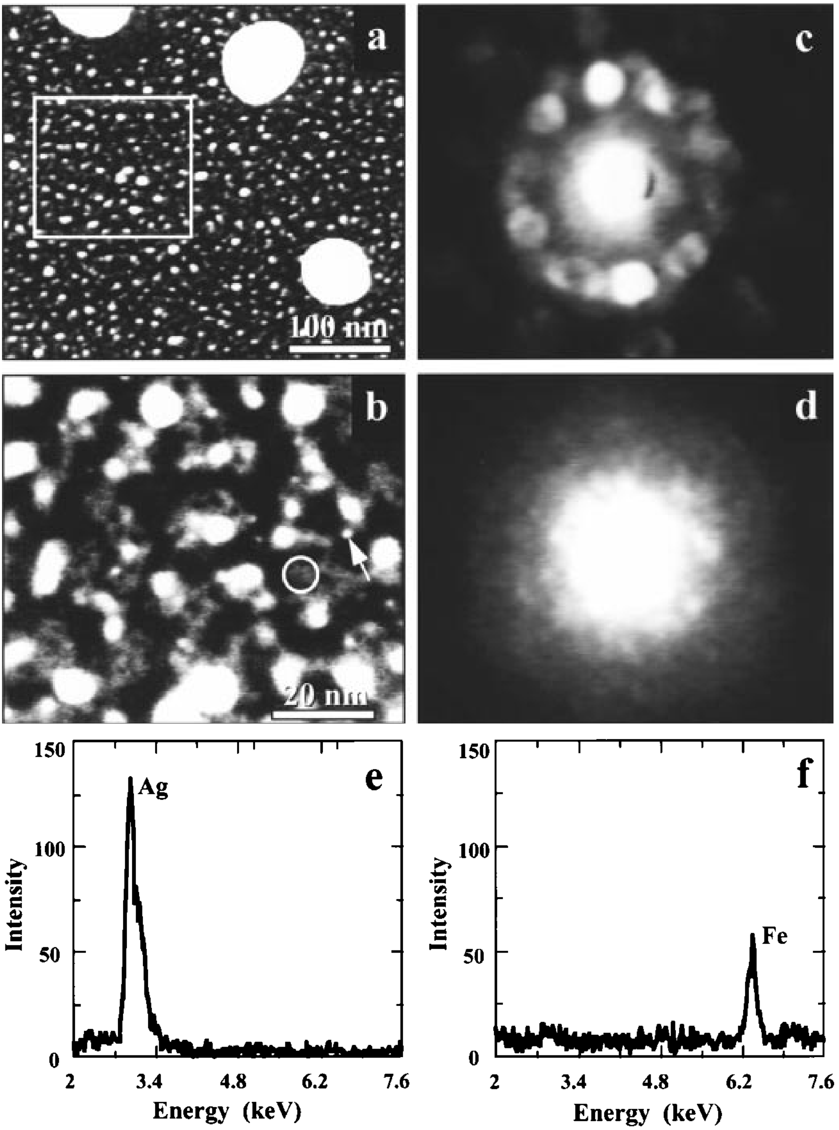

Figure 4-34. Nanoanalysis of Fe_XAg_{1-X} giant magnetoresistance films. HAADF images clearly show two phases with distinctive contrast. Nanodiffraction patterns show that some of the small particles have an icosahedral shape (c) and the matrix film is highly disordered (d). XEDS spectra (e) and (f) were obtained from the small particle (indicated by the arrow in (b)) and the matrix film (the region inside the circle in (b)), respectively. The XEDS spectra show that there is a complete phase separation in the Fe_XAg_{1-X} film, and the bright particles are silver and the highly disordered matrix consists of only Fe.

in images formed by collecting high-angle scattered electrons; and thus, the spatial and the size distributions of nanoparticles can be obtained. Nanodiffraction patterns, formed by positioning an electron nanoprobe at the area of interest, can provide crystallographic information about nanoparticles and their supports. XEDS and EELS can be used to give complementary information about the composition, electronic structure, and state of oxidation of nanoparticles as well as their supports. Elementally specific and surface sensitive techniques such as AES and SAM can be used to extract information about surface chemistry of nanoparticles or other nano-structured materials.

The combination of all these high spatial resolution imaging, diffraction, and analytical techniques in a single microscope makes the STEM the most powerful tool for characterizing nanoparticles (see Figs. 4-4 and 4-22). For example, in the study of giant magnetoresistance (GMR) in granular Fe_XAg_{100-X} magnetic films, it was found that the GMR is sensitive to the Fe volume fraction, and the size distribution and the inter-particle distances of the ferromagnetic particles. STEM and associated techniques were used to characterize the nano-structure of the magnetic granular films. Figure 4-34 summarizes the major results of the STEM analysis [72]. Based on these results preliminary models of the observed GMR of granular Ag-Fe magnetic films were proposed [157].

With the recent development of electron nanoprobes with a size < 0.2 nm in commercially available 200 kV field-emission TEM instruments, the unique STEM capabilities described in this chapter will soon be available to most researchers. STEM and its associated techniques will become more widespread and useful in solving materials problems in the 21st century.

Acknowledgements

The author is deeply grateful to many collaborators and friends for valuable and insightful discussions on characterization of nanoparticles. The author wishes to express his gratitude to Drs. J. M. Cowley, P. A. Crozier, G. E. Spinnler, J. R. Ebner, J. A. Venables, G. G. Hembree, M. Pan, and Z. L. Wang for giving advice and encouragement.

References

[1] J. M. Cowley, *Appl. Phys. Lett.* **1969**, *15*, 58.
[2] E. Zeitler, M. G. R. Thomson, *Optik* **1970**, *31*, 258, 359.
[3] J. M. Cowley, *Diffraction Physics*, 2nd ed., New York, North-Holland, **1981**.
[4] J. M. Cowley, *Ultramicroscopy* **1993**, *49*, 4.
[5] J. Konnert, P. D'Antonio, J. M. Cowley, A. Higgs, H. J. Ou, *Ultramicroscopy* **1989**, *30*, 371.
[6] J. M. Rodenburg, R. H. T. Bates, *Philos. Trans. R. Soc. Lond.* **1992**, *A339*, 521.
[7] J. M. Rodenburg, B. C. McCallum, P. D. Nellist, *Ultramicroscopy* **1993**, *48*, 304.
[8] J. C. H. Spence, J. M. Cowley, *Optik* **1978**, *50*,129.
[9] L. Reimer, *Energy-Filtering Transmission Electron Microscopy*, New York, Springer, **1995**.
[10] M. Mitome, K. Takayanagi, Y. Tanishiro, *Ultramicroscopy* **1990**, *33*, 255.
[11] C. Mory, C. Colliex, J. M. Cowley, *Ultramicroscopy* **1987**, *21*, 171.
[12] A. V. Crewe, J. Wall, J. Langmore, *Science* **1970** *168*,1338.
[13] A. V. Crewe, J. Wall, *J. Mol. Biol.* **1970**, *48*, 373.
[14] A. V. Crewe, *Rep. Progr. Phys.* **1980**, *43*, 621.
[15] M. Isaacson, D. Kopf, M. Utlaut, N. W. Parker, A. V. Crewe, *Proc. Natl. Acad. Sci.*, **1977**, *74*, 1802.

[16] M. Isaacson, D. Kopf, M. Ohtsuki, M. Utlaut, *Ultramicroscopy* **1979**, *4*, 101.
[17] M. Ohtsuki, *Ultramicroscopy* **1980**, *5*, 325.
[18] A. Howie, *J. Microscopy* **1979**, *117*, 11.
[19] M. M. J. Treacy, A. Howie, C. J. Wilson, *Philos. Mag.* **1978**, *A38*, 569.
[20] M. M. J. Treacy, S. B. Rice, *J. Microsc.* **1989**, *156*, 211.
[21] J. Liu, J. M. Cowley, *Ultramicroscopy* **1990**, *34*, 119.
[22] S. B. Rice, J. Y. Koo, M. M. Disco, M. M. J. Treacy, *Ultramicroscopy* **1990**, *34*, 108.
[23] S. A. Bradley, M. J. Cohn, S. J. Pennycook, *Microsc. Res. Tech.* **1994**, *28*, 427.
[24] P. D. Nellist, S, J, Pennycook, *Science* **1996**, *274*, 413.
[25] K. J. Hanssen, G. Ade, *Optik* **1976**, *44*, 237.
[26] H. Rose, *Ultramicroscopy* **1977**, *2*, 251.
[27] J. Silcox, P. Xu, R. F. Loane, *Ultramicroscopy* **1992**, *47*, 173.
[28] S. J. Pennycook, L. A. Boatner, *Nature* **1988**, *336*, 565.
[29] D. H. Shin, E. J. Kirkland, J. Silcox, *Appl. Phys. Lett.* **1989**, *55*, 2456.
[30] P. Xu, E. J. Kirkland, J. Silcox, R. Keyse, *Ultramicroscopy* **1990**, *32*, 93.
[31] D. E. Jesson, S. J. Pennycook, S. J. Baribeau, *Phys. Rev. Lett.* **1991**, *66*, 750.
[32] J. Liu, J. M. Cowley, *Ultramicroscopy* **1993**, *52*, 335.
[33] A. J. McGibbon, S. J. Pennycook, J. E. Angelo, *Science* **1995**, *269*, 519.
[34] S. J. Pennycook, D. E. Jesson, A. J. McGibbon, P. D. Nellist, *J. Electron Microsc.* **1996**, *45*, 36.
[35] S. J. Pennycook, D. E. Jesson, *Phys. Rev. Lett*. **1990**, *64*, 938.
[36] S. J. Pennycook, D. E. Jesson, *Ultramicroscopy* **1991**, *37*, 14.
[37] R. F. Loane, P. Xu, J. Silcox, *Acta Crystallogr.* **1991**, *A47*, 267.
[38] S. Hillyard, R. F. Loane, J. Silcox, *Ultramicroscopy* **1993**, *49*, 14.
[39] S. Hillyard, J. Silcox, *Ultramicroscopy* **1993**, *52*, 325.
[40] Z. L. Wang, J. M. Cowley, *Ultramicroscopy* **1989**, *31*, 437.
[41] Z. L. Wang, J. M. Cowley, *Ultramicroscopy* **1990**, *32*, 275.
[42] M. M. J. Treacy, J. M. Gibson, *Ultramicroscopy* **1993**, *52*, 31.
[43] D. E. Jesson, S. J. Pennycook, *Proc. R. Soc. Lond*. **1993**, *A441*, 261.
[44] J. Fertig, H. Rose, *Optik* **1981**, *59*, 407.
[45] R. F. Loane, E. J. Kirkland, J. Silcox, *Acta Crystallogr.* **1988**, *A44*, 912.
[46] J. M. Zuo, J. C. H. Spence, *Philos. Mag.* **1993**, *A68*, 1055.
[47] J. Broeckx, M. Op de Beeck, D. Van Dyck, *Ultramicroscopy* **1995**, *60*, 71.
[48] J. T. Fourie, *Optik* **1994**, *95*, 128.
[49] J. M. Cowley, J. C. H. Spence, V. V. Smirnov, *Ultramicroscopy* **1997**, *68*, 135.
[50] J. K. Weiss, R. W. Carpenter, A. A. Higgs, *Ultramicroscopy* **1991**, *36*, 319.
[51] J. O. Malm, M. A. O'Keefe, *Ultramicroscopy* **1997**, *68*, 13.
[52] J. Liu, J. M. Cowley, *Ultramicroscopy* **1991**, *37,* 50.
[53] J. M. Cowley, *Ultramicroscopy* **1993**, *49*, 4.
[54] J. M. Cowley, M. S. Hansen, S. Y. Wang, *Ultramicroscopy* **1995**, *58*, 18.
[55] J. M. Cowley, V. I. Merkulov, J. S. Lannin, *Ultramicroscopy* **1996**, *65*, 61.
[56] N. H. Dekkers, H. de Lang, *Optik* **1974**, *41*, 452.
[57] L. H. Veneklasen, *Optik* **1975**, *44*, 447.
[58] J. M. Chapman, P. E. Batson, E. M. Waddell, R. P. Ferrier, *Ultramicroscopy* **1978**, *3*, 203.
[59] I. R. McFayden, J. M. Chapman, *Electron Microsc. Soc. Amer. Bull.* **1992**, *22*, 64.
[60] R. Darji, A. Howie, *Micron* **1997**, *28*, 95.
[61] J. M. Cowley, *J. Electron Microsc. Tech.* **1986**, *3*, 25.
[62] J. C. H. Spence, J. M. Zuo, *Electron Microdiffraction*, New York, Plenum Press, **1992**.
[63] M. Pan, J. M. Cowley, *Ultramicroscopy* **1988**, *26*, 205.
[64] J. M. Cowley, J. C. H. Spence, *Ultramicroscopy* **1981**, *6*, 359.
[65] J. Zhu, J. M. Cowley, *Acta Cryst.* **1982**, *A38*, 718.
[66] J. M. Cowley, R. A. Roy, *Scanning Electron Microsc.* **1981**, 143.
[67] A. Howie, L. D. Marks, S. J. Pennycook, *Ultramicroscopy* **1982**, *8*, 163.
[68] M. Pan, J. M. Cowley, I. Y. Chan, *J. Appl. Cryst.* **1987**, *20*, 300.
[69] J. M. Cowley, R. J. Plano, *J. Catal*. **1987**, *108*, 199.
[70] J. M. Cowley, P. Nikolaev, A. Thess, R. E. Smalley, *Chem. Phys. Lett.* **1997**, *265*, 379.
[71] J. Zhu, J. M. Cowley, *Ultramicroscopy* **1985**, *18*, 419.
[72] J. Liu, Z. G. Li, H. Wan, A. Tsoukatos, G. C. Hadjipanayis, *Mat. Res. Soc. Symp. Proc*. **1994**, *332,* 303.
[73] M. Pan, J. M. Cowley, J. C. Berry, *Ultramicroscopy* **1989**, *30*, 385.
[74] J. G. Allpress, J. V. Sanders, *Surf. Sci*. **1967**, *7*, 1.
[75] M. J. Yacaman, K. Heinemann, C. Y. Yang, H. Poppa, *J. Cryst. Growth* **1979**, *47*, 187.
[76] M. J. Yacaman, M. A. Borja, *Catal. Rev.-Sci. Eng*. **1992**, *34*, 55.

[77] S. Iijima, T. Ichahasi, *Phys. Rev. Lett.* **1986**, *50*, 616.
[78] J. M. Cowley, J. C. H. Spence, *Ultramicroscopy* **1979**, *3*, 433.
[79] J. M. Cowley, M. A, Osman, P. Humble, *Ultramicroscopy* **1984**, *15*, 311.
[80] H. J. Ou, A. A. Higgs, J. M. Cowley, *Mater. Res. Soc. Symp. Proc.* **1989**, *139*, 223.
[81] J. M. Cowley, *Ultramicroscopy* **1979**, *4*, 413.
[82] K. Tsuda, M. Tanaka, *J. Electron Microsc.* **1996**, *45*, 59.
[83] W. J. Vine, R. Vincent, P. Spellward, J. W. Steeds, *Ultramicroscopy* **1992**, *41*, 423.
[84] S. Yamada, M. Tanaka, *J. Electron Microsc.* **1995**, *44*, 213.
[85] J. A. Lin, J. M. Cowley, *Ultramicroscopy* **1986**, *19*, 31.
[86] V. Ronchi, *Appl. Optics* **1964**, *3*, 437.
[87] D. Gabor, *Nature* **1948**, *161*, 777.
[88] D. Gabor, *Proc. R. Soc. Lond.* **1949**, *A197*, 454.
[89] J. A. Lin, J. M. Cowley, *Ultramicroscopy* **1986**, *19*, 179.
[90] M. Mankos, M. R. Scheinfein, J. M. Cowley, *J. Appl. Phys.* **1994**, *75*, 7418.
[91] M. Mankos, P. de Haan, V. Kambersky, G. Matteucci, M. R. McCartney, Z. Yang, M. R. Scheinfein, J. M. Cowley in *Electron Holography* (Eds.: A. Tonomura, L. F. Allard, G. Pozzi, D. C. Joy, Y. A. Ono), New York, Elsevier Science B. V. **1995**, p329.
[92] R. F. Egerton, *Electron Energy-Loss Spectroscopy in the Electron Microscope*, 2nd ed., New York, Plenum Press, **1996**.
[93] L. Reimer, *Scanning Electron Microscopy*, Berlin, Springer, **1985**.
[94] D. C. Joy, *J. Microscopy* **1987**, *147*, 51.
[95] M. S. Chung, T. E. Everhart, *Phys. Rev.* **1977**, *B15*, 4699.
[96] M. Rosler, W. Brauer, *Phys. Status Solidi* **1981**, *B104*, 161.
[97] R. Bindi, H. Lantari, P. Rostaing, *J. Phys.* **1980**, *D13*, 461.
[98] M. Rosler, W. Brauer, *Phys. Status Solidi* **1988**, *B148*, 213.
[99] J. Schou, *Scanning Microscopy* **1988**, *2*, 607.
[100] P. Kruit, J. A. Venables, *Ultramicroscopy* **1988**, *25*, 183.
[101] G. G. Hembree, P. A. Crozier, J. S. Drucker, M. Krishnamurthy, J. A. Venables, J. M. Cowley, *Ultramicroscopy* **1989**, *31*, 111.
[102] H. Seiler, *Scanning Microscopy* **1988**, *2*, 1885.
[103] J. A. Venables, G. D. T. Spiller, D. J. Fathers, C. J. Harland, M. Hambucken, *Ultramicroscopy* **1983**, *11*, 149.
[104] A. L. Bleloch, A. Howie, R. H. Milne, *Ultramicroscopy* **1989**, *31*, 99.
[105] J. Liu, J. M. Cowley, *Ultramicroscopy* **1993**, *52*, 335.
[106] A. Howie, *J. Microsc.* **1995**, *180*, 192.
[107] D. Imeson, R. H. Milne, S. D. Berger, D. McMullan, *Ultramicroscopy* **1985**, *17*, 243.
[108] A. Howie, R. H. Milne, *Ultramicroscopy* **1985**, *18*, 427.
[109] J. Liu, J. M. Cowley, *Ultramicroscopy* **1987**, *23*, 463.
[110] T. Nagatani, S. Saito, *Scanning Microscopy Suppl.* **1987**, *1*, 901.
[111] J. Liu, J. M. Cowley, *Scanning Microscopy* **1988**, *2*, 65.
[112] J. Liu, J. M. Cowley, *Scanning Microscopy* **1988**, *2*, 1957.
[113] J. Drucker, M. R. Scheinfein, J. Liu, J. K. Weiss, *J. Appl. Phys.* **1993**, *74*, 7329.
[114] H. Seiler, *J. Appl. Phys.* **1983**, *54*, R1.
[115] D. C. Joy, J. P. Pawley, *Ultramicroscopy* **1992**, *47*, 80.
[116] D. C. Joy, C. S. Joy, *Micron* **1996**, *27*, 247.
[117] D. Briggs, J. C. Riviere in *Practical Surface Analysis: Auger and X-ray Photoelectron Spectroscopy* (Eds.: D. Briggs, M. P. Seah), 2nd ed., New York, John Wiley & Sons, **1990**, Chapter 3.
[118] M. P. Seah, W. A. Dench, *Surf. Interface Anal.* **1979**, *1*, 2.
[119] J. Liu, G. Hembree, G. Spinnler, J. Venables, *Surf. Sci.* **1992**, *256*, L111; *Catal. Lett.* **1992**, *15*, 133.
[120] G. G. Hembree, J. A. Venables, *Ultramicroscopy* **1992**, *47*, 109.
[121] J. Liu, G. G. Hembree, G. E. Spinnler, J. A. Venables, *Ultramicroscopy* **1993**, 52, 369.
[122] N. C. MacDonald, J. R. Waldrop, *Appl. Phys. Lett.* **1971**, *19*, 315.
[123] A. P. Janssen, J. A. Venables, *Surf. Sci.* **1978**, *77*, 351.
[124] M. M. El Gomati, A. P. Janssen, M. Prutton, J. A. Venables, *Surf. Sci.* **1979**, *85*, 309.
[125] J. Cazaux, J. Chazelas, M. N. Charasse, J. P. Hirtz, *Ultramicroscopy* **1988**, *25*, 31.
[126] C. J. Harland, J. A. Venables, *Ultramicroscopy* **1985**, *17*, 9.
[127] J. Ferron, E. C. Goldberg, *Surf. Sci.* **1992**, *275*, 114.
[128] J. Cazaux, *J. Surf. Anal.* **1997**, *2*, 286.
[129] J. Cazaux, *Surf. Interface Anal.* **1989**, *14*, 354.
[130] D. B. Williams, G. I. Goldstein, D. E. Newbury (Eds.), *X-ray Spectrometry in Electron Beam Instruments,* New York, Plenum Press, **1995**.

[131] M. M. Disko, C. C. Ahn, B. Fultz (Eds.), *Transmission Electron Energy-Loss Spectrometry in Materials Science,* Pennsylvania, TMS, Warrendale, **1992**.
[132] J. J. Hren, J. I. Goldstein, D. C. Joy (Eds.), *Introduction to Analytical Electron Microscopy*, New York, Plenum Press, **1979**.
[133] N. D. Browining, M. F. Chisholm, S. J. Pennycook, *Nature* **1993**, *366*, 143.
[134] S. J. Pennycook, N. D. Browning, D. E. Jesson, M. F. Chisholm, A. J. McGibbson, *Appl. Phys.* **1993**, *A57*, 385.
[135] D. A. Muller, Y. Tzou, R. Raj, J. Silcox, *Nature* **1993**, *366*, 725.
[136] N. D. Browining, S. J. Pennycook, *J. Microsc.* **1995**, *180*, 230.
[137] P. E. Batson, *J. Electron Microsc.* **1996**, *45*, 51
[138] C. Colliex, *J. Electron Microsc.* **1996**, *45*, 44.
[139] D. A. Muller, D. A. Shashkov, R. Benedek, L. H. Yang, J. Silcox, D. N. Seidman, *Phys. Rev. Lett.* **1998**, *80*, 4741.
[140] G. Duscher, N. D. Browning, S. J. Pennycook, *Phys. Status Solidi* **1998**, *A166*, 327.
[141] D. J. Wallis, N. D. Browning, C. M. Megaridis, P. D. Nellist, *J. Microsc.* **1996**, *184*, 185.
[142] J. A. Hunt, D. B. Williams, *Ultramicroscopy* **1991**, *38*, 47.
[143] S. Q. Sun, S. L. Shi, J. A. Hunt, R. D. Leapman, *J. Microsc.* **1995**, *177*, 18.
[144] C. Jeanguillaume, C. Colliex, *Ultramicroscopy* **1989**, *28*, 252.
[145] A. Howie, *Ultramicroscopy* **1983**, *11*, 141.
[146] R. Garcia-Molina, A. Gras-Marti, A. Howie, R. H. Ritchie, *J. Phys. C: Solid State Phys.* **1985**, *18*, 5335.
[147] R. H. Richie, A. Howie, *Philos. Mag.* **1988**, *A58*, 753.
[148] Z. L. Wang, J. M. Cowley, *Ultramicroscopy* **1987**, *21*, 77, 335.
[149] M. G. Walls, A. Howie, *Ultramicroscopy* **1989**, *28*, 40.
[150] C. E. Lyman, J. I. Goldstein, D. B. Williams, D. W. Ackland, S. Von Harrach, A. W. Nicholls, P. J. Statham, *J. Microsc.* **1994**, *176*, 85.
[151] J. Tong, J. Liu, Z. C. Kang, L. Eying, *J. Alloys and Compound*s **1994**, *207*, 416.
[152] C. E. Lyman, *Ultramicroscopy* **1986**, *20*, 119.
[153] R. D. Leapman, J. A. Hunt, *Microsc. Microanal. Microstruct.* **1991**, *2*, 231.
[154] C. E. Lyman in *Physical Aspects of Microscopic Characterization of Materials* (Eds.: J. Kirschner, K. Murata, J. A. Venables) Scanning Microscopy International, AMF O'Hare, Illinois, **1987**, p123.
[155] C. Mory, H. Kohl, M. Tence, C. Colliex, *Ultramicroscopy* **1991**, *37*, 191.
[156] O. L. krivanek, C. Mory, M. Tence, C. Colliex, *Microsc. Microanal. Microstruct.* **1991**, *2*, 257.
[157] Z. G. Li, H. Wan, J. Liu, A. Tsoukatos, G. C. Hadjipanayis, L. Liang, *Appl. Phys. Lett.* **1993**, *63*, 3011.